Multi-Foci Beamforming Using Curved Linear Array Transducer for Qualitative Identification of Lipids in Human Liver

by

Waqas Bin Khalid

B.S, GIK Institute of Engineering Sciences and Technology, Pakistan, 2010

M.S, University of Minnesota Duluth, USA, 2016

Submitted to the Graduate Faculty of the

Swanson School of Engineering in partial fulfillment

of the requirements for the degree of

Doctor of Philosophy

University of Pittsburgh

2020

UNIVERSITY OF PITTSBURGH

SWANSON SCHOOL OF ENGINEERING

This dissertation was presented

by

Waqas Bin Khalid

It was defended on

September 15, 2020

and approved by

Charles Laymon, PhD, Associate Professor, Departments of Bioengineering, Mechanical Engineering and Materials Science

George D. Stetten, MD, PhD, Professor, Department of Bioengineering

Xucai Chen, PhD, Associate Professor, Department of Medicine

Dissertation Director: Kang Kim, PhD, Associate Professor, Departments of Bioengineering, Medicine, Mechanical Engineering and Materials Science

Multi-Foci Beamforming Using Curved Linear Array Transducer for Qualitative Identification of Lipids in Human Liver

Waqas Bin Khalid, Ph.D.

University of Pittsburgh, 2020

Nonalcoholic fatty liver disease (NAFLD) is the leading cause of liver chronic diseases in the U.S. and its prevalence is growing in the world. In the United States, it affects an estimate of 80 to 100 million people. In less than a decade, NAFLD will likely become the number one cause of liver transplants in the country. NAFLD cases have risen rapidly over the last three decades and is the most common liver disease in children. NAFLD encompasses a disease spectrum of a variety of liver conditions ranging from simple steatosis (SS) to nonalcoholic steatohepatitis (NASH). SS is a benign form of the disease, characterized by the accumulation of lipid in the liver. On the other hand, NASH is defined by hepatic steatosis with cell injury, hepatic ballooning and various degrees of fibrosis. NASH may further develop into cirrhosis, liver failure and hepatocellular carcinoma (HCC). A non-invasive, early detection and accurate staging of NAFLD may allow for a timely intervention and treatment to prevent the progression of the disease to cirrhosis and HCC.

We hypothesized a new dual-modality ultrasound imaging combining acoustic radiation force impulse (ARFI) imaging and thermal strain imaging (TSI) implemented on a clinical ultrasound probe. ARFI imaging utilizes high intensity focused ultrasound to generate a push in a region of interest (ROI). The response of the tissue inside the region of excitation due to the acoustic radiation push is determined by estimating the displacement between the pre-push reference frames and the post-push tracking frames. TSI has been used in the field of medical imaging for detecting lipids in atherosclerotic plaques and quantification of liver fat in ob/ob mice. TSI is based

on the fact that the speed of sound changes differently in respect to the increase in temperature for different tissue composition. Lipids register a decreasing sound speed with increasing temperature, whereas water-bearing tissue exhibit an increasing sound speed with increasing temperature. Development of the proposed multi-modality system will be a step towards a novel clinical system which would permit the creation of a single co-registered image featuring information regarding lipid content and liver stiffness.

Table of Contents

List of Tables

List of Figures

Preface

First and foremost, I would like to thank my advisor, Dr. Kang Kim, for his leadership and advice. I would not have finished my PhD without his support and patience. It is a frequently heard cliché; however, it is not an overstatement in this situation to say that without the consistent guidance and encouragement from Dr. Kim, this thesis would never have existed.

I would like to extend my sincere gratitude to my defense committee members i.e. Dr. Charles Laymon, Dr. George Stetten and Dr. Xucai Chen, for taking the time out for my defense presentation and agreeing to be on my committee. I would like to thank Dr. Laymon for his words of encouragement prior to my thesis defense. These words are always going to be dearer to me. It was an honor and pleasure to be a teaching assistant for Dr. George Stetten's class. It was a great learning opportunity to educate myself about various imaging modalities being used in the field of medical imaging. I would also like to thank Dr. Chen who went above and beyond for his help and spending countless hours on running the hydrophone experiment.

I would also like to thank my fellow graduate students at my lab for giving me valuable advice when work wasn't progressing according to plan. A special thanks to Nick Mance, BioE graduate administrator at the department of Bioengineerig and Dr. Sanjeev Shroff. I would also like to acknowledge the friends from the Pittsburgh Squash Federation who have been a second family to me in Pittsburgh.

To my family, particularly my mother and my siblings, thank you for your love, your endless encouragement, your prayers and your unwavering trust in me. I will not be the person without you that I am today.

Above all, I would like to thank my wife, Rabiya, for her love and constant support, for all those late nights and early mornings, and for keeping me sane over the past few years. Thank you for being my editor and proofreader. But most important of all, thank you for being my best friend. I owe you everything. I would like to let my son, Khalid, know that he has been a source of happiness and hope in my life. In my life, he was my stress-relieving tablet.

1.0 Introduction

1.1 Non-Alcoholic Fatty Liver Disease

Non-alcoholic fatty liver disease (NAFLD) is an umbrella term used to define a variety of liver conditions caused by the accumulation of fat. Fat in healthy liver is normal but if it constitutes more than 5-10% of the liver's weight, then it is called NAFLD [1]. NAFLD encompasses a spectrum of liver conditions ranging from simple steatosis (SS) to non-alcoholic steatohepatitis (NASH), a more aggressive steatosis [2]. SS is a benign form of the disease associated with the accumulation of adipose tissue in the liver [3]. NASH is associated with fibrosis, cirrhosis and in some cases leads to hepatocellular carcinoma (HCC), ultimately requiring a liver transplant [4].

NAFLD is the most common chronic liver disease in developing countries. The causes of NAFLD remains unknown, however, the origin of NAFLD is not associated with viral causes or the consumption of alcohol. There are no symptoms affiliated with NAFLD. Individuals who have metabolic syndrome, such as type 2 diabetes, hypertension, hypertriglyceridemia, hyperlipidemia and obesity, are more at risk of NAFLD [5]. Moreover, individuals diagnosed with NAFLD are more prone to heart diseases [6]. There is no approved drug in the market for treating NAFLD. The ailments caused by NAFLD can only be reversed by adopting a healthy lifestyle. This includes exercising regularly and maintaining a healthy balanced diet. NAFLD develops in 4 main stages [7]. Figure 1.1 shows the stages of NAFLD initiating from a healthy liver and progressing towards aggravated stages of NAFLD.

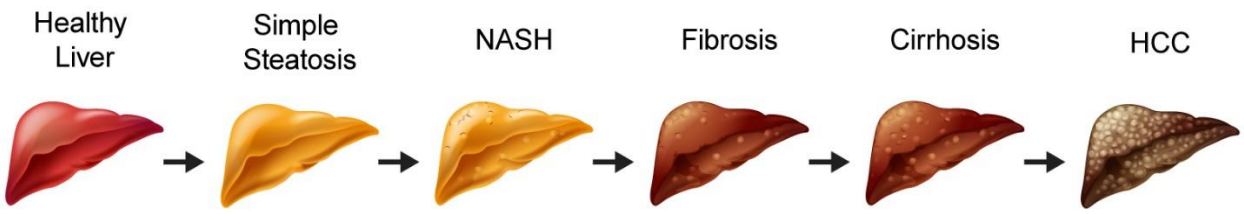

Figure 1.1: Stages of NAFLD starting from a healthy liver and advancing towards aggravated stages of NAFLD

Simple Steatosis (SS)

A healthy liver contains little to no fat. Simple steatosis is harmless deposition of adipose tissue inside the liver cells [8]. The detection of this particular stage is referred to an accidental discovery, because it is found during medical tests carried out for other reasons such as a routine ultrasound scan or elevated levels of liver enzymes detected during a routine blood screening test [9]. At this stage, there is no inflammation or damage to the liver cells. It is possible to stop the progression of the disease to irreversible stages if it is identified and managed at this stage.

Non-alcoholic steatohepatitis (NASH)

Non-alcoholic steatohepatitis is an aggregated form of the disease where the liver has inflamed. Inflammation is the natural response of the body to damage or injury, however, in this situation it is an indicator that the liver cells are damaged [10]. The damage at this stage can still be reverted by regular exercise and a change in diet. If the liver remains undiagnosed, this persistent liver cell damage can escalate towards scarring of the liver tissue causing fibrosis and cirrhosis [11].

Fibrosis

Consistent inflammation leads to scarring of the liver tissue and adjoining blood vessels. The scarred liver tissue replaces some of the healthy liver tissue, but the liver is still functional at this stage [12].

Cirrhosis

Cirrhosis is defined as the most severe form of the disease due to the persistent inflammation over a long period of time. The liver is severely scarred reduced in size accompanied with severe inflammation [13]. The damage at this stage is irreversible and permanent and can progress towards liver failure, ultimately requiring a liver transplant.

1.2 Liver Biopsy

Currently, liver biopsy is the gold standard for diagnosing NAFLD. Liver biopsy is successful in differentiating NASH from simple steatosis [14]. However, liver biopsy is invasive in nature and can cause medical complications such as bleeding and perforated liver. Moreover, liver biopsy suffers from sampling bias as only a very small fraction of the liver tissue is used. The distribution of the adipose tissue across the liver is not evenly distributed. Therefore, acquiring a small volume of liver tissue may report false negative results. Furthermore, due to the invasive nature of the procedure, a longitudinal monitoring of the disease in response to treatment is not possible with liver biopsy as this would require repeated measurements [15].

Limitations of liver biopsy have been acknowledged by the medical community leading to a surge in non-invasive methods for diagnosing the stages of NAFLD. Currently, numerous imaging modalities involving ultrasonography (US), computed tomography (CT), magnetic

resonance imaging (MRI) are being used to diagnose NAFLD and quantitation of triglycerides inside the liver [16].

1.3 Imaging Modalities

Computed Tomography (CT)

Computed tomography estimates hepatic steatosis quantitatively by measuring the attenuation value of liver expressed as Hounsfield units (HU). Attenuation value for a healthy normal liver is approximately 55 HU, however, attenuation value of fat is much lower, -100 HU. With the accumulation of fat inside the liver, the attenuation value for liver decreases as NAFLD develops and progresses. Several studies have revealed a cut off value of 40 HU as an indication of fat content greater than 30% [17]. However, the cutoff value is subjected to inconsistency as it depends upon the injection rate, patient circulation and phase of enhancement [18]. A major concern with CT is that it exposes patients to a high dose of ionizing radiation which precludes its use as a screening tool, especially among children.

Magnetic Resonance Imaging (MRI)

Magnetic resonance imaging is the most accurate imaging modality for estimating hepatic steatosis. MRI determines a metric called proton density fat fraction (PDFF) which is a measure of fat within the liver tissue. MRI does not expose patients to ionizing radiation, but it remains a very expensive imaging modality and is not easily available in remote clinics [19].

Ultrasound (US)

Ultrasound remains a popular choice for diagnosing NAFLD as it does not expose patients to ionizing radiation and is comparatively cheap compared to other imaging modalities and is easily available in remote clinics. However, US is also subjected to its limitations such as subjective assessment depending upon the expertise of the clinician [17]. Additionally, US experiences poor results when performed on morbidly obese individuals and suffers from inter- and intra-observer variability. Also, US cannot distinguish among the different stages of NAFLD [20].

1.4 Thermal Strain Imaging (TSI)

Thermal strain imaging (TSI) is an ultrasound-based imaging modality founded on the principle that the speed of sound in a medium is dependent on the temperature based on tissue composition. For water bearing tissue, the speed of sound increases with an increase in temperature. However, for lipid bearing tissue the speed of sound decreases with an increase in temperature [21, 22]. Figure 1.2 shows the relationship of the speed of sound with an increase in temperature for water and castor oil.

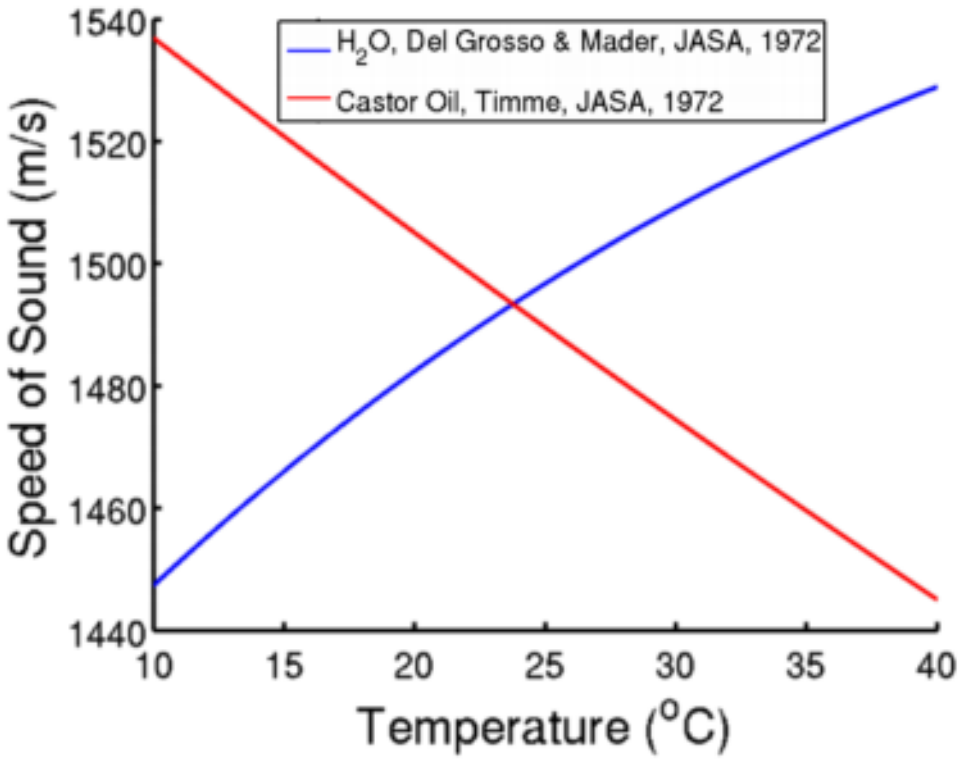

Figure 1.2: Relationship of the speed of sound with temperature for water and castor oil.

Modern ultrasound systems calculate distances by determining the time of the returned echoes, assuming that the speed of sound in biological tissue is 1540 m/s. With an increase in temperature for water bearing tissue, the speed of sound increases resulting in a shorter return time. This results in water bearing tissue appearing closer towards the transducer surface. However, with an increase in temperature the speed of sound decreases resulting in a longer return time for lipid bearing tissue. This leads to lipid bearing tissue appearing further away from the transducer surface. Typically, a temperature rises of $\leq 2°C$ is enough to generate a change in sound speed. In literature, thermal strain imaging has been used interchangeably with temporal strain imaging making an emphasis that the signal recorded is merely because of the temporal echo shift rather

than a true mechanical strain. The physics of thermal strain imaging can be shown by the following equation:

$$\frac{du}{dz} = -\lambda \Delta T \qquad (1)$$

where du/dz is the thermal strain, λ [$°C^{-1}$] is the linear coefficient for sound speed vs. temperature. At a normal body temperature (37°C), λ is positive for water-bearing tissue with values ranging from 0.7×10^{-3} to 1.3×10^{-3} and is negative for lipid-based tissues with values ranging from -1.3×10^{-3} to -2.0×10^{-3} [23].

A typical ultrasound pulse sequence for TSI comprises of three steps. Firstly, a reference frame is acquired. Followed by heating to induce a small change in temperature. Lastly, a post-heating frame is acquired. The schematic for the TSI pulse sequence is shown in Figure 1.3.

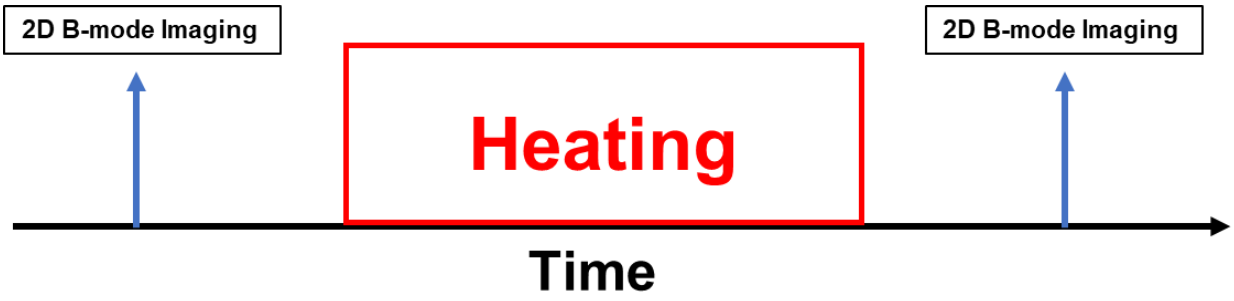

Figure 1.3: Schematic for the TSI pulse sequence. Ultrasound B-mode images are acquired before and after heating

The relative displacement between the pre-heating frame and post-heating frame is calculated and a derivative in the direction of wave travel yields the thermal or temporal strain.

1.5 Acoustic Radiation Force Impulse (ARFI) Imaging

Acoustic radiation force impulse (ARFI) imaging has been used to access the mechanical properties of tissue. ARFI imaging is clinically available and is essential in determining the structural information such as the size of lesions present in breast, prostrate, and kidney which are difficulty to visualize with conventional ultrasound B-mode [24]. Acoustic radiation force result from the transfer of momentum from an ultrasonic wave to the medium through which it is traveling. ARFI utilizes high intensity focused ultrasound to generate a push in a region of interest. The response of the tissue inside the region of excitation due to the acoustic radiation push is determined by estimating the displacement between the pre-push reference frames and the post-push tracking frames [13]. Our lab has demonstrated the use of ARFI imaging to study the biomechanics of tissues including rotator cuff tendon in response to increasing force. The fibers inside the rotator cuff tendon become stiffer on direct application of increasing load. This relationship is examined from the displacement recorded by ARFI imaging as the displacement value inside the tendon decreases with increasing force implying a stiffer tendon. We have also exhibited, ARFI imaging can be used to distinguish among various tissue types. Capsule, muscle and tendon each have different mechanical properties, and this was confirmed among the variation in the ARFI displacement measurements. We plan to implement this technology on liver to monitor the stiffness changes with development of fibrosis in liver.

1.6 Motivation

Many patients with NAFLD remain undiagnosed throughout their life and as aforementioned NAFLD can progress into simple steatosis leading to steatohepatitis, advanced fibrosis, cirrhosis and eventually cancer. Therefore, ultimately requiring a liver transplant. There exists a strong need of noninvasive, inexpensive screening tool that can assess fat accumulation in liver to stop the progression of the disease towards HCC. Moreover, to reflect the histopathological changes in liver because of hepatic ballooning and scarring of liver tissue, this screening tool should also evaluate liver stiffness to reflect the bio-mechanical changes during the evolution of the disease. We hypothesize that a new dual-modality ultrasound imaging, combining thermal strain imaging (TSI) and acoustic radiation force impulse (ARFI) imaging implemented on a commercially available, clinical ultrasound probe can be used to quantitatively estimate fat and stiffness of liver. Upon successful validation, the impact of the project will be influential in the NAFLD management, being complemented with laboratory assays to provide 1) critical diagnostic and prognostic information, 2) cost effective monitoring of the disease and treatment response. Therefore, the two specific aims of this project are:

Specific Aim 1: to develop a dual-modality imaging system combining TSI and ARFI using a single clinical ultrasound probe. This imaging system will be used to access lipid content as triglycerides build up during NAFLD progression and measure liver stiffness to reflect the pathological changes inside liver. Multi-foci beamforming technique is at the heart of designing the ultrasound heating and pushing beams for this system.

Specific Aim 2: to determine the relationship of the combined TSI-ARFI imaging on excised human liver specimen with histopathology. This is an essential step in making this dual-

modality imaging system into a clinical reality. This imaging system will be evaluated by carrying out ex-vivo experiments, excised human liver tissue embedded in gelatin phantom will be fabricated to validate this imaging technology and correlate the results against histopathology. A successful implementation of this aim will make it one step closer towards a clinical realization.

1.7 Thesis Outline

The purpose of this thesis is to demonstrate the translation of a combined TSI and ARFI imaging sequence on a commercially available curved linear array transducer for abdominal imaging.

Chapter 2 details a study carried out on obese or ob/ob mice using thermal strain imaging with a custom designed TSI system. TSI was used to quantify lipid composition of fatty livers at different stages in ob/ob mice (n = 28). A strong correlation coefficient was observed ($R^2 = 0.85$) between lipid composition measured with US-TSI and hepatic triglyceride content (HTGC). HTGC is used to quantify adipose tissue in liver. The ob/ob mice were divided into 3 groups of none, mild and moderate, by the degree of steatosis that is used in clinics. Non-parametric Kruskal-Wallis test was conducted to determine if TSI can potentially differentiate among the different stages of NAFLD. Chapter 3 is an introduction to multi-foci beamforming. Chapter 4 successfully implements TSI on a single, commercially available curved linear array transducer for heating and imaging of organs at a deeper depth. This yielded a heating area from 32 to 96 mm in the axial direction and -7 to +7 mm in the lateral direction. The pressure fields generated from simulation were in agreement with pressure fields measured with hydrophone. TSI with safe acoustic power identified with high contrast a rubber inclusion and liposuction fat tissue embedded in a gelatin

block. Chapter 5 establishes the relationship of the combined TSI-ARFI imaging on excised human liver specimen with histopathology. Chapter 6 discusses the future directions and constraints of this work for future translational efforts.

2.0 Noninvasive Assessment of Liver Fat in Ob/Ob Mice Using Ultrasound-Induced Thermal Strain Imaging and Its Correlation with Hepatic Triglyceride Content

2.1 Introduction

Nonalcoholic fatty liver disease (NAFLD) is a term used for defining a variety of liver conditions ranging from simple accumulation of adipose tissue in liver to more aggravated stages such as steatosis, fibrosis, cirrhosis and in some cases hepatocellular carcinoma (HCC). Currently, there are no obvious causes for NAFLD. The pathological changes inside the liver for NAFLD resembles that of alcohol-induced liver injury, however, NAFLD occurs in patients who do not abuse alcohol consumption. Obesity is the leading cause of NAFLD and it effects an estimated of 74% of the obese population and 24% of the general public across the globe [25]. As obesity has continued to rise among children so has NAFLD. It is projected that NAFLD may progress to cirrhosis in the estimated 8% of the children diagnosed with the disease [26]. With advances in treatment for hepatitis, NAFLD will most likely become the number one cause for liver transplant in the western hemisphere in less than a decade [27]. Previous studies have shown that 10% to 29% of NAFLD patients may develop liver cirrhosis within 10 years and 4% to 27% of these patients will progress to cancer [28]. However, the progression of NAFLD can be prevented with proper diagnosis, a change in diet and regular exercise [29]. Inevitability, there exists a need for a clinical technology to accurately identify and monitor early stages of NAFLD.

Currently, liver biopsy is the gold standard for diagnosing NAFLD. However, needle biopsy is subjected to sampling error because only 1/50,000 of the entire liver volume is sampled [30]. This quantitate information may be of limited use because of the heterogenous distribution

of lipid across the liver. Moreover, liver biopsy is invasive and can lead to medical complications such as the risk of infection, formation of hematoma, leakage of bile, and internal bleeding. Finally, histological findings from liver biopsy are subjective and dependent upon the experience and expertise of the pathologist. Several cases have been reported where children have shown resilience to liver biopsy because of the invasive nature of the procedure [31].

The limitations of liver biopsy have led to an increase in developing noninvasive methods for screening NAFLD. Noninvasive methods include imaging modalities such as computed tomography (CT), magnetic resonance imaging (MRI) and ultrasound (US) [32]. CT is the least popular choice among these imaging modalities to diagnose NAFLD as patients are exposed to high dosage of ionizing radiation and it cannot be used as a diagnostic tool in children. CT has a broad spectrum of sensitivity, 54% to 93%, and high specificity, 95% to 100%, for diagnosing NAFLD [33]. However, CT has limited diagnostic ability for quantitative evaluation of mild steatosis; it is more sensitive to the detection of moderate to advanced steatosis. CT cannot differentiate between NASH from simple hepatic steatosis [32].

MRI is overall more sensitive compared to CT in detecting NAFLD. The average sensitivity and specificity ranges for detecting NAFLD are 82.0% to 97.4% and 76.1% to 95.3% for MRI [34]. Studies have shown that MRI provides an accurate and more reproducible hepatic triglyceride content measurement [35]. With recent advancements in proton MR spectroscopy, the entire spectrum of steatosis along with the degree of fibrosis can be evaluated. Unlike CT, MRI can differentiate between normal and abnormal tissues i.e. distinguish simple steatosis from fibrosis and HCC [36]. MRI does not expose patients to ionizing radiation, but it has a few limitations such as the cost associated with MRI scan and not being widely available in remote

clinics compared to CT and US. Also, MRI scan is not allowed for the patients with implants that are sensitive to magnetic field [37].

Transabdominal ultrasound remains the preferred choice among imaging modalities when it comes to diagnosing NAFLD due to its relatively low cost, widespread availability and safety features. Fatty livers in US B-mode images display a variety of features. For example, hyper echogenicity of the liver parenchyma due to the fat accumulation compared to the adjacent right kidney and spleen [38]. Other common features of fatty liver under US B-mode images include attenuation of the ultrasound beam, hepatomegaly, decreased visibility of vascular margins and diaphragm [39]. A wide spectrum of sensitivities, 60% to 94%, and specificities, 66% to 95%, for ultrasound in diagnosing NAFLD have been reported [40]. However, obesity among patients reduces the sensitivity of ultrasound. These studies are nonreproducible and suffer from subjective assessment based mostly on an operator and have considerable inter and intra-observer variability [41]. US B-mode images may not be conclusive in diagnosing NAFLD if there is a missing or deceased organ such as a kidney or spleen that are compared with fatty liver. Moreover, US B-mode cannot quantify the degree of adipose tissue present in liver and cannot distinguish between simple steatosis from steatohepatitis [42].

Ultrasound induced temporal/thermal strain imaging (US-TSI) is an imaging modality for applications pertaining to noninvasive tissue thermometry [43] and detection of lipid rich cores in atherosclerotic plaques [44-46]. US-TSI is based on the principle that the speed of sound in a medium is dependent upon the temperature for different tissue compositions. Lipids register a decreasing sound speed with increasing temperature, whereas water-bearing tissue exhibits an increasing sound speed with an increasing temperature [21, 22]. With the rise in temperature inside the medium, the US radiofrequency (RF) signal arrives earlier or later at the transducer surface

depending on an increase or a decrease in the sound speed. The derivative of these temporal echo shifts in the direction of wave propagation yields the thermal strain. With a rise in temperature, lipids reveal positive thermal strain and water-based tissues reveal negative thermal strain.

The governing equation for TSI is as follows:

$$\frac{du}{dz} = (\beta - \lambda)\Delta T \qquad (2\text{-}1)$$

where du/dz is the thermal strain, λ [$°C^{-1}$] is the linear coefficient for sound speed vs. temperature and β [$°C^{-1}$] is the linear coefficient of thermal expansion. For temperatures less than 50°C, β is an order of magnitude much smaller than λ and can therefore be ignored [47]. Thus, the principal equation for TSI becomes:

$$\frac{du}{dz} = -\lambda\Delta T \qquad (2\text{-}2)$$

At a normal body temperature (37°C), λ is positive for water-bearing tissue with values ranging from 0.7×10^{-3} to 1.3×10^{-3} and is negative for lipid-based tissues with values ranging from -1.3×10^{-3} to -2.0×10^{-3} [23].

In a previous study carried out by our lab, US-TSI was successful in differentiating between normal livers of control mice and fatty livers in obese mice. US-TSI measured a significant difference between thermal strains of fatty livers in obese mice and in the control mouse livers. To verify and measure the lipid content in mice livers, oil red O histology was performed as a gold standard. US-TSI was able to identify fats in excised livers of obese mice with a sensitivity and specificity of 70% and 90%. The area under the receiver operating characteristic (ROC) curve was 0.775 [48]. Due to the limited sample size (n=10) in this study, US-TSI was not able to distinguish among the different degree of steatosis in NAFLD.

In our study, US-TSI was used to quantify lipid composition of fatty livers at different degrees of steatosis of ob/ob mice. To validate the results from our imaging modality, lipid

composition was correlated against hepatic triglyceride content (HTGC). HTGC is widely used in clinics to quantify lipid buildup in fatty liver [49]. With an increased sample size of 28, the mice were divided into 3 groups of none, mild and moderate, based upon HTGC values. In comparison to the previous study, non-parametric Kruskal-Wallis test was carried out demonstrating that US-TSI can potentially differentiate among the degrees of steatosis in NAFLD.

2.2 Materials and Methods

2.2.1 Animals

The postmortem experiment in this study was performed on mice liver. Figure 2.1 details the experimental setup and procedure. The mice were obtained from the Jackson Laboratory animal facility, Bar Harbor, Maine, under the regulation of approved IACUC protocol. US-TSI was performed on a total of 28 ob/ob mice livers. The ob/ob mice were on a high cholesterol diet for a duration of 16 weeks. It is reported that by the 7th week mark the ob/ob mice will develop hepatic steatosis in 50% of their cells and by the 13th week they will further develop steatosis in 85% of their hepatocytes [50]. The mice were euthanized by a veterinary technician before US-TSI was performed. Ultrasound gel was centrifuged to remove the presence of air bubbles in the ultrasound gel before being placed on the abdomen of the mice. The experiment was carried out at room temperature.

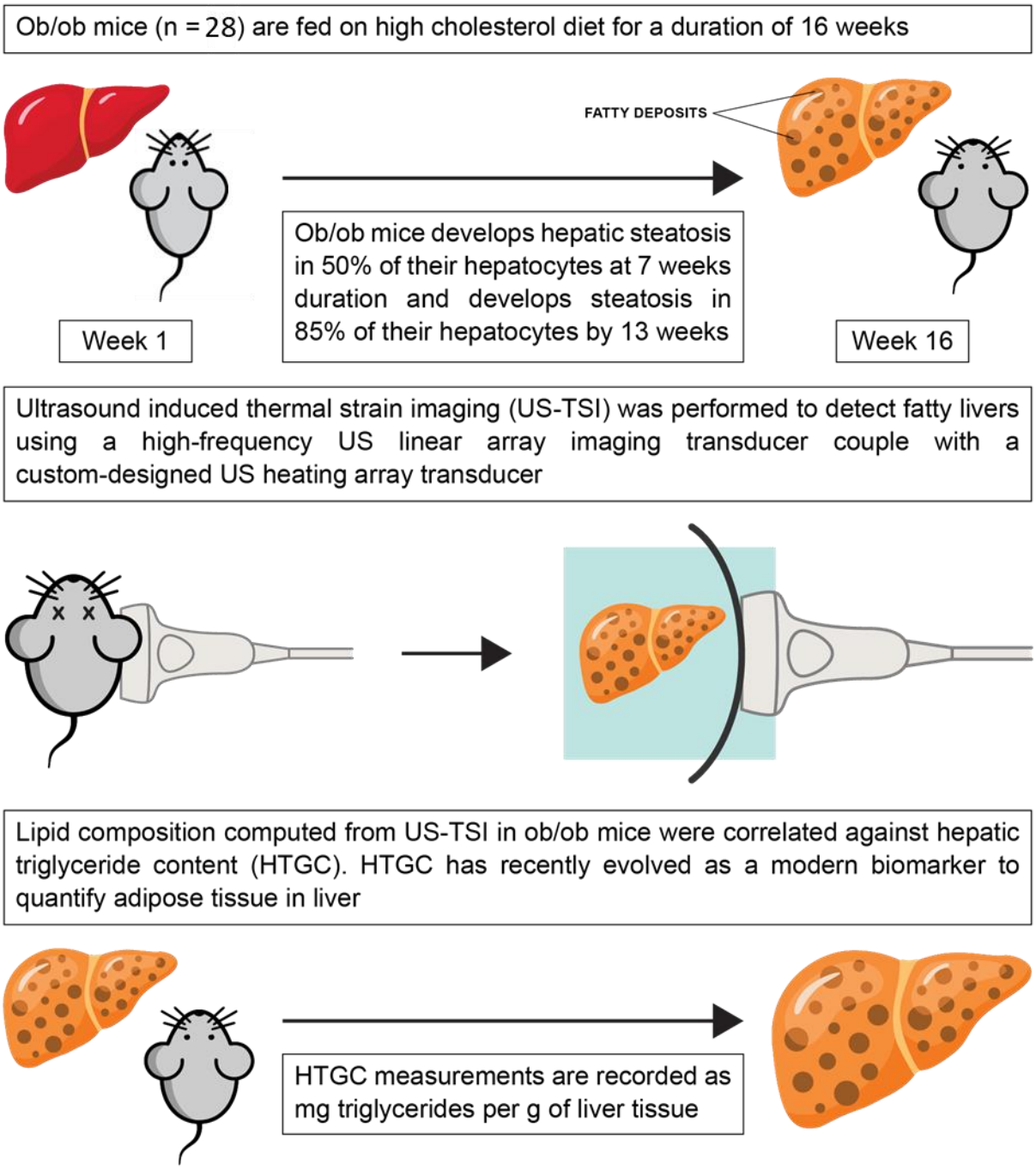

Figure 2.1: Experimental setup and protocols

2.2.2 Biochemical hepatic triglyceride content (HTGC) analysis

HTGC measurements were obtained using the protocol described in [51]. The HTGC measurements were calculated using a Trig/GB kit (#11877771216, Roche Diagnostics, Indianapolis, Indiana) and were recorded as milligram of triglycerides per gram of liver tissue. Lipid specimens were extracted from 50 to 100 mg of frozen liver tissue.

2.2.3 Experimental set-up

US-TSI requires two systems, a US imaging transducer and a US heating transducer to raise the temperature of the tissue during scanning. The first system consisted of a high frequency small animal-based imaging system (Vevo2100, FUJIFILM VisualSonics Inc., Canada) equipped with a high frequency linear array transducer for imaging (13 to 24 MHz). The second system consisted of a custom engineered US heating array transducer. This heating transducer was made of six elements assembled in a group of three elements on both sides of the imaging transducer aligned in a custom designed manifold. The heating beam width was at least 8 mm in the lateral direction and 5 mm wide-ranging in the axial direction providing a larger area for heating. For a detailed blueprint of the custom engineered heating array transducer the reader is referred to [52].

US-TSI sequence consisted of acquiring pre-frames followed by a heating duration of 9.2 seconds and then acquiring post-frames as shown in Figure 2.2. The long delay period between heating and acquiring post-frames was taken into consideration to avoid any motion being introduced by the acoustic radiation force. US B-mode images were acquired before and after heating at a frame rate of 10 Hz. The center frequency used for imaging was 21 MHz and 3.55 MHz for the heating transducer. The custom designed heating transducer ran at a duty cycle of

50%. For this study, a homogeneous gelatin phantom was manufactured, and a temperature rise of 1.5 °C was recorded. Temperature rise during US-TSI was measured inside the gelatin phantom using a Type T needle sheathed thermocouple (MT-23/5, Thermoworks, UT, USA) connected to a data acquisition module (QuadTemp, Thermoworks, Lindon, UT, USA). Temperature measurements were recorded 3 times at an axial depth of 25 mm and 0 mm in the lateral direction.

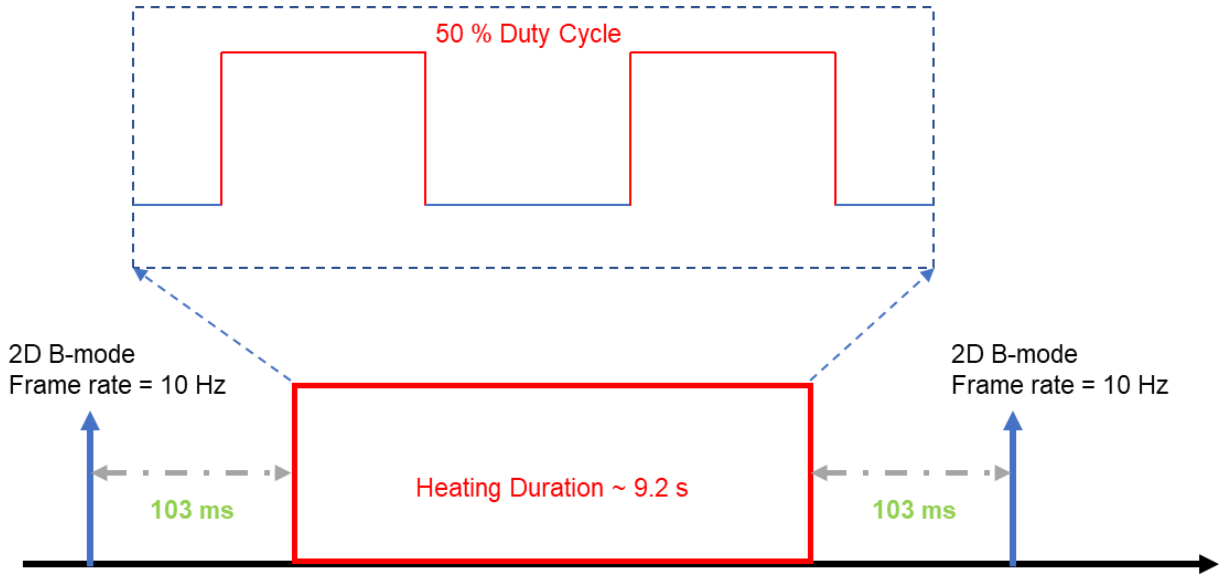

Figure 2.2: Ultrasound pulse sequence for heating and imaging. Two different US systems are required to perform US-TSI on mice liver. The first system consists of a high-frequency US linear array imaging transducer and the second system consist of a custom-designed US heating array transducer

2.2.4 Signal processing

US echo displacement between pre and post frames was tracked using speckle tracking algorithms. Phase-shift algorithm, Loupas 2-D autocorrelator, was used to estimate the displacement. Loupas 2-D algorithm operates on complex IQ data. The axial kernel size for displacement was 3.0 wavelengths. For a detailed understanding of Loupas estimator, the reader

is referred to [53]. A median filter was applied on the displacement outcome. The kernel size for the median filter was 0.55 mm (axial) × 0.27 mm (lateral) [46, 48].

Thermal strain was computed by taking the derivative in the axial direction using a second order savitzky–golay filter. The kernel size for savitzky–golay filter was 1.5 mm. Thermal strain maps were color coded within the heating region such that red indicated positive strain and blue indicated negative strain. These color-coded thermal strain maps were then overlaid on US B-mode images for viewing purposes.

To measure the extent of steatosis in each liver by US-TSI, lipid composition [%] was defined as a metric determined by US-TSI. First, the liver contour was identified from the US B-mode image. Then the number of pixels indicating the positive thermal strain inside the liver was determined. Lipid composition ($[\text{number of positive strain pixels} > \text{Threshold}] / [\text{number of pixels in the liver}]$) was calculated by dividing the positive thermal strain pixels by the number of pixels in the liver. For pixels which were counted towards the positive thermal strain, a threshold was predetermined. This threshold was computed by taking an average of the root mean square (RMS) values outside the heating region for the entire data group. The average RMS value calculated was 0.05%.

2.2.5 Statistical analysis

The triglyceride build-up during the progression of hepatic steatosis was widely spread across the liver lobes. Taking this into consideration, some of the animals were tested twice for HTGC values based upon the observation by a clinical pathologist. The HTGC values for medial and left lobes were recorded. The data was further classified into two groups of medial and left lobes for additional statistical analysis.

Analysis of covariance (ANCOVA) was performed to test if the liver lobes had any influence on the correlation between HTGC values and lipid composition determined by US-TSI. In this scenario, the covariate for ANCOVA analysis were the liver lobes. A pre-condition test for ANCOVA was successful before the statistical analysis. A p-value of >0.05 concluded that the livers lobes had statistically no effect on the correlation between HTGC values and lipid composition. Eventually, this led to combining the data from medial and left lobes into a single data entity. For mice that had two HTGC values, a single value was picked from the dataset by a normally distributed random generator algorithm, eliminating any possible incidences of bias being introduced by the operator.

A linear regression, Pearson's correlation coefficient, was used for correlating lipid composition determined from US-TSI and HTGC. Then a non-parametric Kruskal-Wallis test was carried out to further validate if US-TSI could be used to differentiate among the degree of steatosis in NAFLD.

2.3 Results

The results were divided into 3 groups of HTGC values reflecting the degree of steatosis in NAFLD. The amount of liver steatosis was classified as follow: none (< 5%), mild (5%-33%) and moderate (34%-66%) [54]. Figure 2.3(a) shows the distribution of HTGC values of multiple lobes of the liver in mice. The liver lobes were divided into three groups, none (n = 5), mild (n = 34) and moderate (n = 5) to demonstrate the degree of liver steatosis based on HTGC values. Figure 2.3(b) shows the distribution of HTGC values as a result of running the normally distributed random generator algorithm. For mice with two HTGC values, a single value was chosen from the dataset to eliminate any possible incidences of bias being introduced by the operator. The liver lobes were later divided into three groups, none (n = 3), mild (n = 23) and moderate (n = 2).

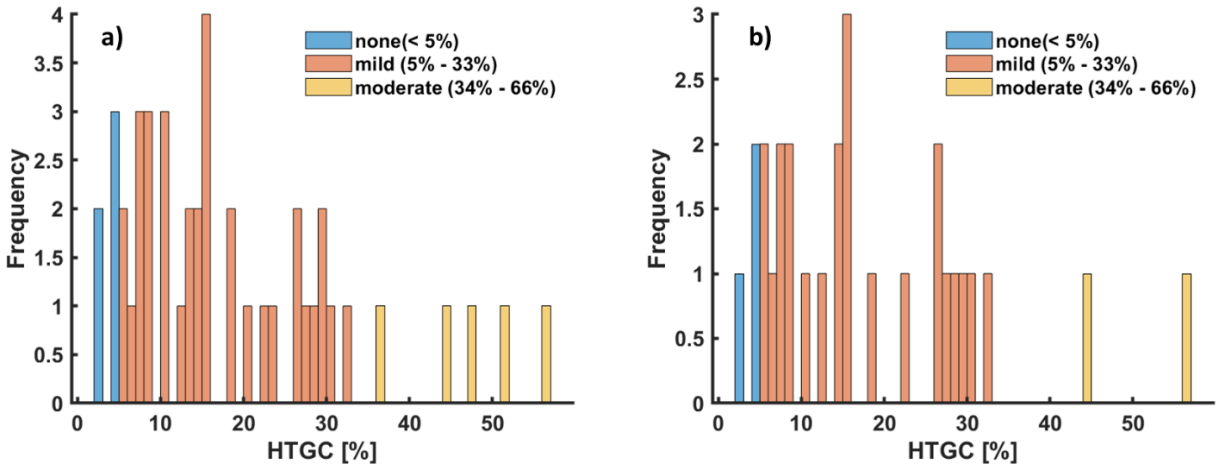

Figure 2.3: (a) Histogram of the mice population representing multiple lobes of the liver. The liver lobes were divided into three groups, none (n = 5), mild (n = 34) and moderate to severe (n = 5) to demonstrate the degree of liver steatosis based on HTGC values. (b) Histogram of the mice population representing a single lobe of the liver. For mice with two HTGC values, a single value was chosen from the dataset to eliminate any possible incidences of bias being introduced by the operator. The liver lobes were later divided into three groups, none (n = 3), mild (n = 23) and moderate to severe (n = 2).

Figure 2.4 shows the results of Pearson's correlation coefficient between HTGC values and lipid composition computed by US-TSI on the combined data set irrespective of the liver lobes. A

close correlation (R^2 = 0.85) existed between HTGC and US-TSI measurements. A p-value of 2.89 x 10^{-12} was calculated.

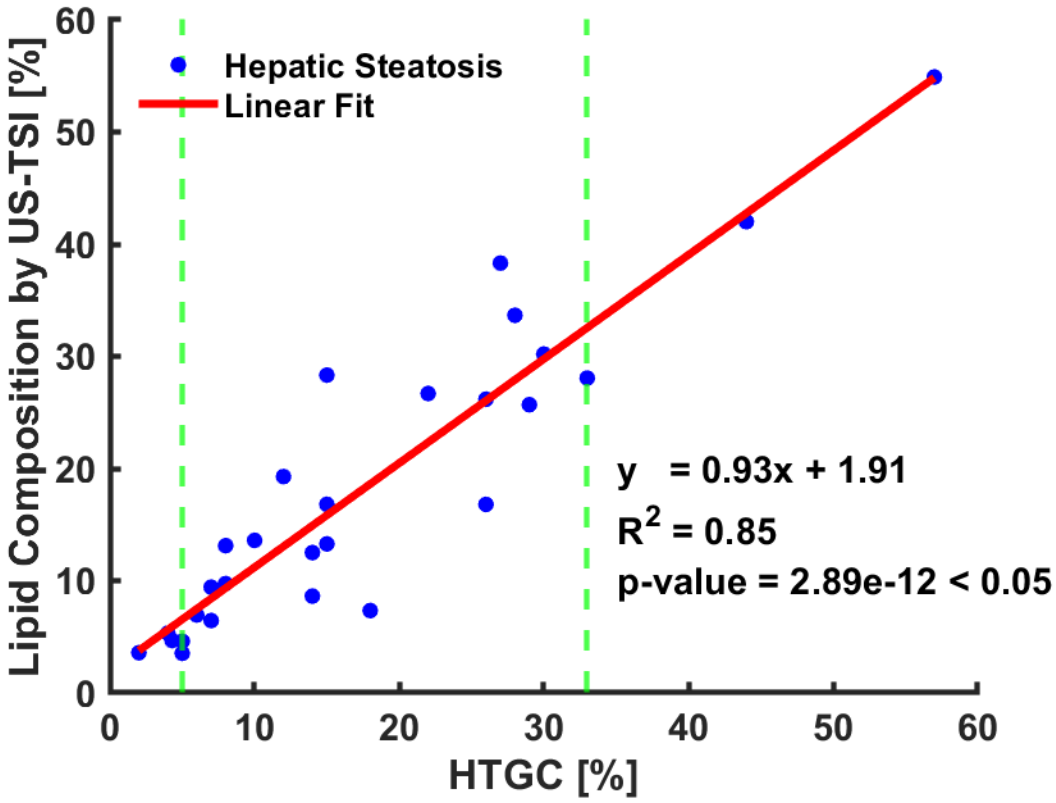

Figure 2.4: Pearson's correlation coefficient between HTGC and US-TSI measurements for combined dataset. A close correlation (R2 = 0.85) was observed between HTGC and US-TSI measurements of percentage strain. A p-value <0.05 was considered significant

The results of the Kruskal-Wallis test are shown in Figure 2.5. This test rejects the null hypothesis implying that at least one of the groups had a different mean of lipid composition compared to the other groups. Further post hoc analysis such as multiple comparisons tests needed to be carried out to determine which group differed from the other. The post hoc test used was the Dunn's test. Table 2.1 shows the results of the Dunn's test. The first two columns show the groups compared to each other. By conventional norm, a two tailed p-value of <0.05 was considered to

be statistically significant. Statistical analysis was carried out using the statistics toolbox of MATLAB R2019a.

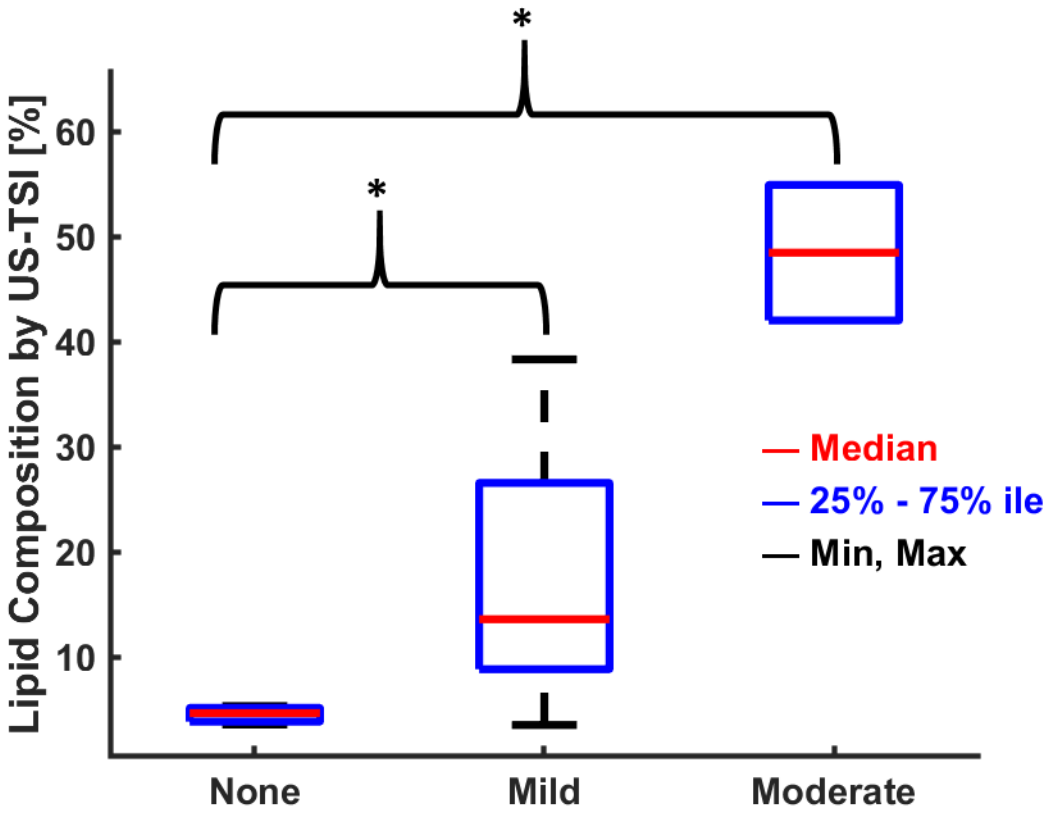

Figure 2.5: Non-parametric, Kruskal-Wallis Test was performed to determine if US-TSI can differentiate among the stages of Hepatic Steatosis. The non-parametric test, Kruskal-Wallis was performed to determine if there are statistically significant differences between the stages of hepatic steatosis detected by US-TSI. A p-value <0.05 was considered significant

Table 2.1: P-value for the post hoc test, Dunn's test

Stages of NAFLD		p-value
None	Mild	0.0067
None	Moderate	0.0014
Mild	Moderate	0.1609

Figure 2.6 (a - c) shows US B-mode images of mice liver. The approximate region of heating is indicated by the curved dotted line in Figure 2.6 (a - c). The liver contour is marked by the dashed red line and the strain map is overlaid on the B-mode image in Figure 2.6 (d - f). Figure 2.6 (a and d) shows the results of a mouse that had not developed any steatosis over the duration

of the study. The HTGC value for this mouse was 2%. The corresponding US-TSI map shows the area of negative thermal strain indicating no triglyceride accumulation in the liver. The lipid composition determined by US-TSI for this mouse was 3.5%.

Figure 2.6 (b and e) shows the results of a mouse that had developed mild steatosis with an HTGC value of 33%. US-TSI map displays an area of slight negative and positive thermal strains. The lipid composition determined by US-TSI for this mouse was 28.1%.

Figure 2.6 (c and f) exhibits the results of a mouse that had advanced steatosis with a HTGC value of 44%. US-TSI map displays an area of positive thermal strain indicating the accumulation of triglycerides within hepatocytes. The lipid composition determined by US-TSI for this mouse was 42.0%.

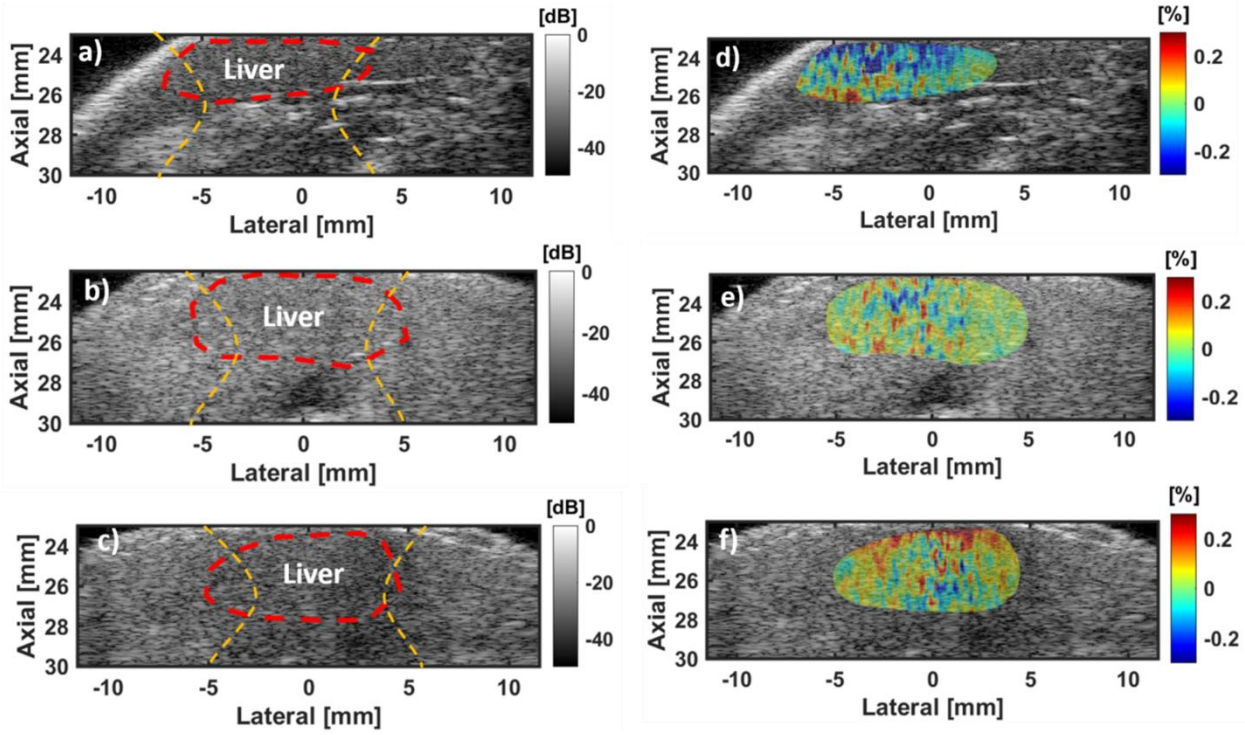

Figure 2.6: (a – c) Ultrasound images acquired using a high-frequency US scanner for medial lobe of the liver with no (HTGC = 2%), mild (HTGC = 33%), and moderate (HTGC = 44%), hepatic steatosis. The contour shows the boundary of the liver. The dotted line shows the approximate size of the heating beam. (d – f) US-TSI for the liver section. The lipid composition determined by US-TSI for none data point was 3.5%, for mild was 28.1% and for moderate was 42.0%

2.4 Discussion

In this study, we introduced US-TSI to measure the fat content in ob/ob mice to distinguish among the degree of steatosis in NAFLD. Our study used HTGC as a benchmark for adipose measurement and to find its correlation with lipid composition determined from US-TSI values. The degree of steatosis is the first step in calculating the NAFLD activity score (NAS). NAS, developed by the NASH clinical research network, is a summation of steatosis, lobular inflammation and ballooning scores. NAS accompanied with the fibrosis staging score provides an accurate staging of NAFLD [55]. Hence, steatosis score is of utmost importance in calculating NAS.

A single value was chosen from the dataset by a normally distributed random generator algorithm for mice with two HTGC values, avoiding all potential incidences of bias introduced by the operator. This step was repeated multiple times to account for a scenario where one HTGC measurement for a mouse would be an accurate representation of the measurement from US-TSI and the second HTGC measurement would be an outlier. A strong correlation ($R^2 > 0.8$) was still observed even after performing several iterations of the Pearson's correlation analysis.

Statistical analysis such as the Kruskal-Wallis test was performed to differentiate among the degree of steatosis in NAFLD. Kruskal-Wallis test was carried out instead of the parametric one-way ANOVA since the data points failed to meet the normality test and homogeneity of variance test. Moreover, the reason for conducting Dunn's test was to account for the unequal sample size among the different groups. The results from Dunn's statistical test concluded that US-TSI can differentiate between none and mild and none and moderate degree of steatosis. The post hoc test failed to conclude if US-TSI can distinguish among the mild and moderate degree of steatosis in NAFLD of the disease. However, further statistical analysis, such as simulating data

points, to increase the sample size for the none, mild and moderate groups concluded US-TSI can also distinguish among the mild and moderate degree of steatosis in NAFLD. Currently, with the limited number of sample sizes, US-TSI was unsuccessful in distinguishing between mild and moderate degree of steatosis in NAFLD. Future studies will need to experiment on a larger quantity of ob/ob mice. A low number of mice population in the none and moderate group can be attributed towards mouse gender. Mouse gender can affect their susceptibility to the development of NAFLD. It has been reported that male mice exhibit an increased susceptibility to development of NAFLD as opposed to female mice [56, 57]. In addition, the mice may be fed on a combination of high-fat diet enriched in fructose, carbohydrate and ethanol feeding to increase the mice population in the mild to severe group [58].

US-TSI requires two separate transducers i.e. one for imaging and one for heating. This is a bulky setup for US-TSI operation and may not be practical for the sonographer during the scanning operation. In addition, this setup requires a dedicated hardware and electrical system for the heating array transducer making it more costly. For clinical translation of US-TSI, the most realistic and viable option would be to use a multi-foci beamforming technique where a single commercially available transducer is used both for heating and imaging. For clinical setting, a low frequency for imaging will be used for a larger penetration depth considering attenuation of ultrasound beam. The frequency for heating can be equal to or less than the imaging frequency. This possible solution has been successfully devised by our group with computer simulation and ex vivo phantom study, using a clinical probe [59, 60]. Moreover, the rise in temperature recorded was 0.3°C during the heating duration, which is much less relative to the current temperature rise.

There were several challenges for an in vivo experiment. Firstly, the physiological motion from breathing and cardiac rhythms in mice is more elevated compared to humans, distorting the

displacement tracking estimation caused by speckle decorrelation. This physiological motion remains extreme even with anesthesia induced in the mice. To compensate for this motion, a postmortem study was carried out in this report. Eventually for human subject studies, patients can be requested to hold their breath for a few seconds (<5 s) to prevent such motions. To compensate for cardiac pulsations, US-TSI frames acquired before and after heating can be synchronized with an ECG trigger. Alternatively, advance signal processing techniques using time series analysis can be used to reduce motion artifact in US-TSI [61]. Moreover, other speckle tracking algorithms can be explored such as Bayesian speckle tracking for estimating ultrasound displacement [62, 63]. In the recent years, there has been a surge of machine-learning algorithms in ultrasonics. Machine-learning algorithms that features speckle tracking can be used for displacement estimation [64, 65].

Secondly, blood perfusion in the liver was neglected in this study. This may possibly affect the temperature of the tissue during in vivo operation of US-TSI. This effect along with thermal diffusion was not taken into consideration during the postmortem study. Further investigation into tissue thermal models or in vivo studies are required to understand and counteract the effect of blood perfusion.

Certain safety measures need to be taken into consideration for future in vivo studies. According to the American Institute of Ultrasound in Medicine (AIUM) “there have been no significant, adverse biological effects observed due to temperature increases less than or equal to 2°C above normal, for exposure durations up to 50 hours”. US-TSI induces a small temperature change (<2°C). The temperature rise recorded during US-TSI was ~1.5°C. The peak negative pressure (PNP) of US heating probe and imaging transducer was determined in a water tank using a hydrophone (HNC, Onda Corp., Sunnyvale, CA) connected to a computer controlled transitional

stage. The small animal imaging system had a negative peak pressure of −1.27 MPa, while it was −1.40 MPa for the heating transducer. Mechanical Index is later computed by using the equation $\mathrm{MI} = \mathrm{NPP}/\sqrt{\mathrm{centerfrequency}}$ [66]. MI for the imaging transducer is 0.28 and 0.74 for the custom designed heating transducer. According to the Food and Drug Administration (FDA), MI cannot exceed above the approved limit of 1.9 [67].

2.5 Conclusion

This study reports US-TSI was able to detect lipids in fatty livers of ob/ob mice. A strong correlation (R^2=0.85) between lipid composition estimated by US-TSI and a clinically established metric, HTGC, was found. In addition, US-TSI was able to distinguish between none and mild, and none and moderate, degrees of steatosis with significance but did not show significant difference between mild and moderate degrees of steatosis. Future studies need to be performed on excised human liver tissue and human liver tissue in a clinical setting for further validation for US-TSI to be used as a clinical diagnostic tool.

2.6 Acknowledgments

This work was supported by the National Institute of Health (NIH) grant 1R21EB016907-01A1 and the small animal imaging system (Vevo 2100) was supported by the NIH grant 1S10RR027383-01.

3.0 Introduction to Multi-Foci Beamforming

3.1 Introduction

Ultrasound is one of the most commonly used imaging modalities in the field of medical imaging. The term ultrasound refers to sound with frequencies that are not audible by the human ear i.e. any sound with range of frequencies above 20 kHz is considered an ultrasound. Medical ultrasound systems typically operate in the range of 2 MHz to 20 MHz [68]. A conventional ultrasound machine consists of a transducer accompanied by its dedicated electronics and operates on the pulse-echo principle. The transducer serves both as a transmitter and receiver of ultrasound energy. A transducer typically converts electrical signals to acoustic signals or vice versa. The transducer generates high frequency ultrasound pulses which propagate through the patient's body. Echoes are generated at the boundaries of the tissues or organs that are reflected back to the transducer. This reflected acoustic signal is converted back to electrical signal. The dedicated electronics using digital signal processing techniques convert these electrical signals to grayscale images depicting the structure of the human anatomy [69]. Ultrasound transducer consists of a sequence of piezo-ceramic crystals, which upon excitation by an electrical impulse generates an acoustic wave. The width of each element is approximately ¼ wavelength which is typically 0.2-0.75 mm in width [70].

Modern ultrasound systems utilize delay-and-sum beamforming for focusing [71]. An ultrasound system typically consists between 64 elements and 256 elements. During transmission the user specifies a focal point (x_f, z_f) of interest, where x_f is the lateral coordinate and $z_f$is the axial coordinate. On transmission, the focus is achieved by ensuring that ultrasound pulses

transmitted from the transducer elements arrive all together at the focal point so that sound waves are added coherently resulting in constructive interference.

For conventional ultrasound B-mode imaging, a narrow beam width is preferred for better image resolution [60]. On the contrary, for TSI, a wide heating ultrasound beam is desired to create a larger area for heating [52]. A precursor to TSI technology comprised of a high efficiency heating array probe coupled with a high frequency imaging transducer [52]. This meant a much heavier and bulkier setup for TSI operation making the scanning operation uncomfortable for the sonographer. Moreover, the setup for TSI operation required skilled expertise such as configuring the heating probe with the imaging transducer for which the sonographer may not be equipped with the right skill set. This TSI system used a series of geometrically focused heating array elements to deposit energy into a small and fixed target region. This target region exhibits a similar anatomical texture compared to the surrounding tissue; it is quite possible that the target region may not get any energy from the heating array. On the contrary, the surrounding tissue may receive the energy. Moreover, the separate heating elements would require dedicated system electronics and hardware that would increase the cost for companies and end users. The imaging center frequency for this TSI system is set at 21 MHz [52]. The ultrasound beam is highly attenuated at this frequency and is not suitable for deeper penetration to image abdominal organs of human subjects. The most realistic option would be to use a commercially available ultrasound scanner that can perform both heating and imaging with a single transducer for clinical translation of TSI. Our group has devised a novel beamforming methodology called multi-foci beamforming where a single transducer is used both for imaging and heating [59, 60]. Multi-foci beamforming utilizes a commercially available off the shelf transducer for TSI operation. Multi-foci beamforming comprises of dividing the transducer aperture, first into three sub-apertures, followed by into four

sub-apertures. A separate delay profile is applied to each sub-aperture. The 3 foci and 4 foci beams are interleaved thus producing a homogeneous region for heating [59, 60].

3.2 Materials and Methods

3.2.1 Sub-aperture Configuration

The first step in the design of heating beams is to determine the aperture configuration for the curved linear array geometry. Curved linear array transducers are primarily designed for abdominal imaging based upon the geometry and center frequency of the transducer.

Figure 3.1 shows transducer array geometry for a curved linear array transducer, Philips ATL C4-2 in the x-z plane. This transducer comprises of 128 elements. For linear array transducer, the -6-dB lateral beam width (BW) and depth of field (DOF) can be approximated from the following equations, assuming linear propagation [72]

$$BW = \lambda\left(\frac{Z_f}{D}\right) = \lambda\,.\,(F/\#) \qquad (3\text{-}1)$$

$$DOF = 8\lambda\left(\frac{Z_f}{D}\right)^2 = 8\lambda.\,(F/\#)^2 \qquad (3\text{-}2)$$

where $\boldsymbol{\lambda}$ is the wavelength, $\boldsymbol{Z_f}$ is the axial focal depth, $\boldsymbol{D}$ is the aperture width, and F-number ($\boldsymbol{F}$/#). From the equations above, it can be determined that by dividing the transducer elements into sub apertures, at a specific frequency and at a fixed depth, increases the f-number. This leads to an increase in the lateral beam width and depth of field. For TSI, a wide heating ultrasound beam with a larger depth of field and a broad lateral beam width is needed to form a large area for heating.

As stated earlier, multi-foci beamforming involves dividing the transducer aperture into a three sub-aperture and a four sub-aperture. Figure 3.2 (a, b) shows the sub-aperture configuration for 3 foci and 4 foci. The 3 foci sub-aperture consists of dividing the transducer aperture as 42-44-

42 and the 4 foci sub-aperture consists of dividing the transducer aperture as 20-44-44-20. Each of the sub-aperture has a different lateral focus. Figure 3.2(c, d) shows the lateral and axial focus for each of the sub-aperture. For the 3 foci sub-aperture, the lateral focus was at [-4.40 0.00 4.40] and for the 4 foci sub-aperture the lateral focus was at [-6.60 -2.20 2.20 6.60]. The axial focus for the 3 foci sub-aperture and for the 4 foci sub-aperture was fixed at 70 mm, equivalent to the elevation focus of the Philips ATL C4-2 transducer. The 3 foci and 4 foci beams are temporally interleaved creating a uniform area for heating resulting in an extended area for heating.

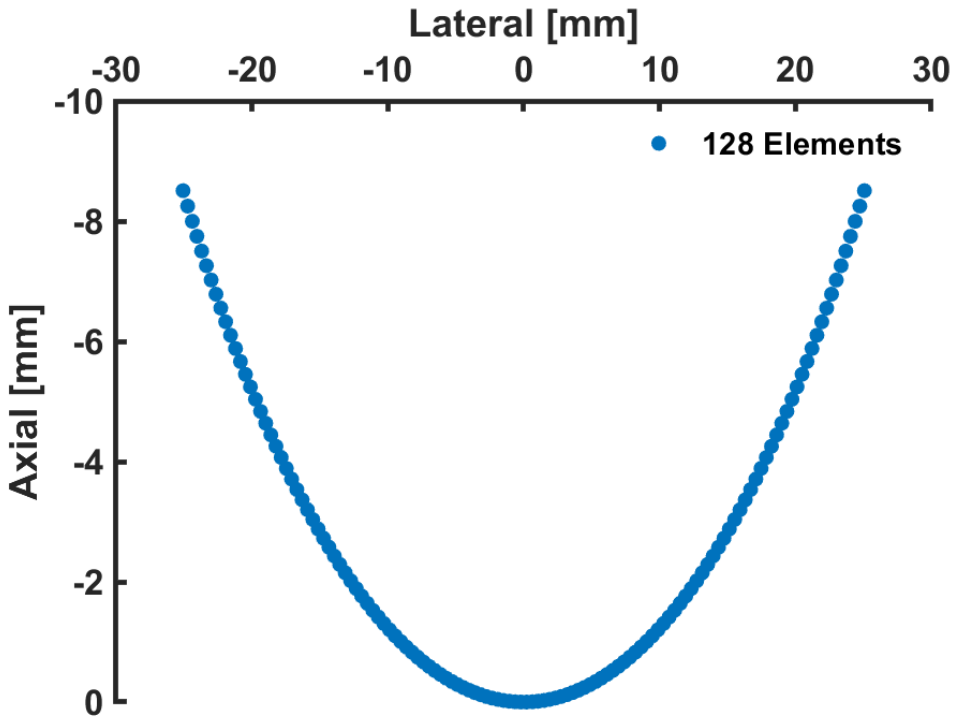

Figure 3.1: Transducer array geometry for a curved linear array transducer, Philips ATL C4-2 in the x-z plane. This transducer consists of 128 elements.

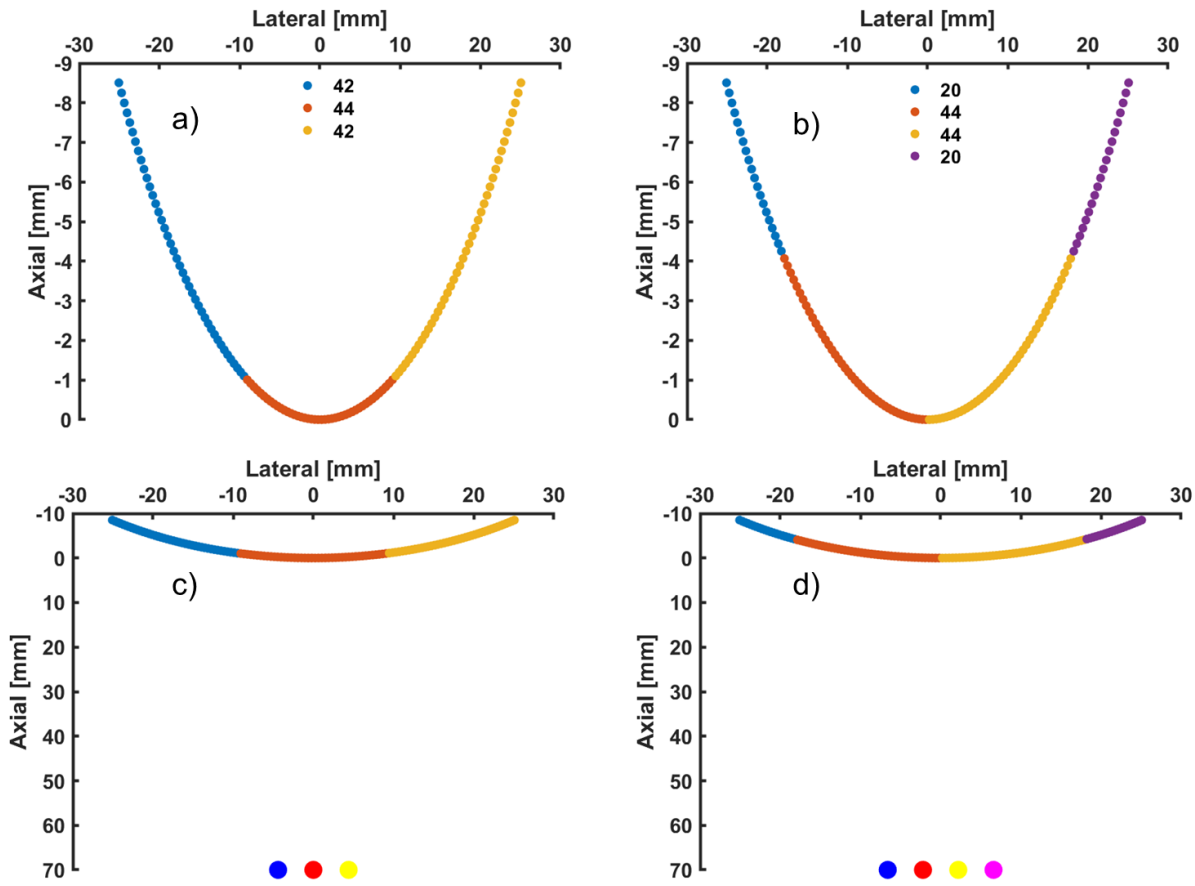

Figure 3.2: (a) The 3 foci sub-aperture consists of dividing the transducer aperture as 42-44-42 and (b) the 4 foci sub-aperture consists of dividing the transducer aperture as 20-44-44-20. (c) The lateral focus for 3 foci sub-aperture was at [-4.40 0.00 4.40] and for the 4 foci sub-aperture the lateral focus was at [-6.60 -2.20 2.20 6.60] (d). The axial focus for the 3 foci sub-aperture and for the 4 foci sub-aperture was fixed at 70 mm.

3.2.2 Delay Curve

Assuming the transducer element T_0 generates a pulse at t = 0, we would have to determine the firing times for the remaining elements for the sound waves to be in-phase at the focal point. The first step in determining the time delay is to calculate the distance from the transducer elements to the focal point by using the Euclidean distance formula.

$$d_i = \sqrt{(x_i - x_f)^2 + (z_i - z_f)^2} \qquad (3\text{-}3)$$

where x_f is the lateral coordinate and z_f is the axial coordinate of the focus or focal point and x_i is the lateral coordinate and z_i is the axial coordinate of the i^{th} transducer element.

The next step is to determine the time it takes for the ultrasound wave to reach the focal point, assuming the speed of sound in soft tissue is c = 1540 ms^{-1}, by using the following equation.

$$t_i = \frac{d_i}{c} \qquad (3\text{-}4)$$

After determining the triggering time, the time delays are given by the following equation.

$$\tau_i = t_{max} - t_i \qquad (3\text{-}5)$$

3.2.3 Pressure Field Simulation

Once the delay curves have been established the next step is to generate the pressure fields. The pressure fields are simulated using the acoustic simulation package, Field II [73]. Table 3.1 list the parameters for Field II simulation. The attenuation coefficient, α, was set to 0.5 dB/cm/MHz, which is the attenuation coefficient reported for soft tissues [72]. The delay curves calculated in the preceding step is fed as an input to simulate the pressure field.

Table 3.1: Parameters for Field II simulation

Parameter	Value
Number of elements	128
Center frequency	3.0 MHz
Sampling frequency	200 MHz
Azimuthal element pitch	0.4246 mm
Elevation element height	13 mm
Radius	41.219 mm
Kerf	0.05 mm
Attenuation	0.5 dB/cm/MHz
Sub-aperture size	42-44-42 (3 foci beam) 20-44-44-20 (4 foci beam)
Grid size	200 × 200 (X × Z)

3.3 Results and Discussion

Figure 3.3(a, b) shows the results of the delay profile for 3 foci and 4 foci sub-aperture.

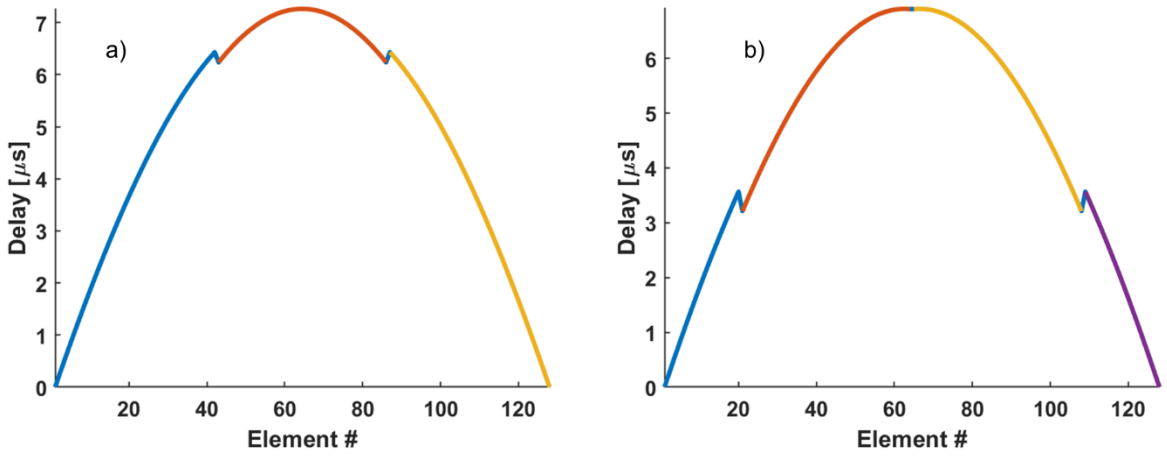

Figure 3.3: (a, b) Delay curves for 3 foci and 4 foci sub-aperture.

Once the delay profiles have been computed, the next step is to utilize these delay curves in simulating the pressure field. Figure 3.4(a, b, c) shows the simulation results of pressure field for 3 foci, 4 foci, and the combined beam.

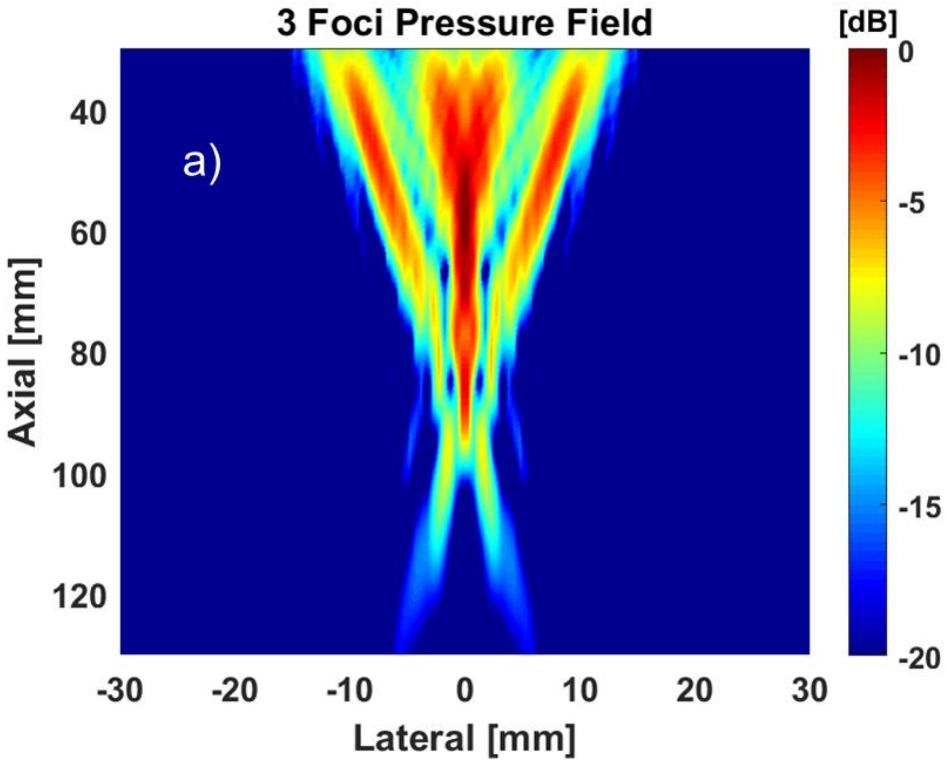
3 Foci Pressure Field
[dB]
0
-5
-10
-15
-20
a)
40
60
80
100
120
Axial [mm]
-30
-20
-10
0
10
20
30
Lateral [mm]

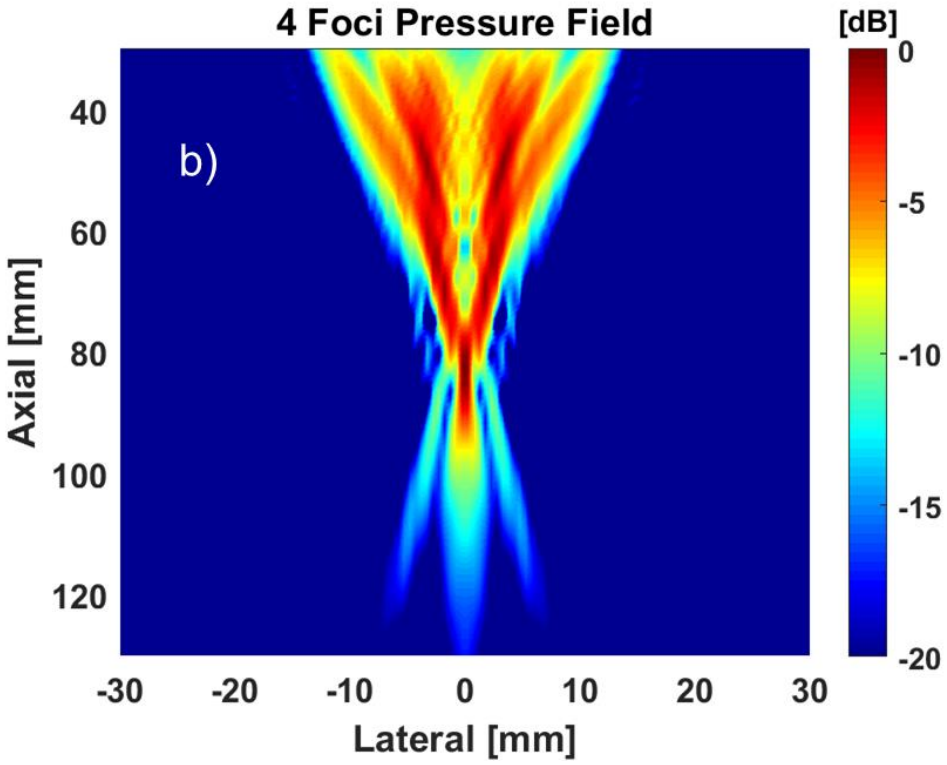
4 Foci Pressure Field
[dB]
0
-5
-10
-15
-20
b)
40
60
80
100
120
Axial [mm]
-30
-20
-10
0
10
20
30
Lateral [mm]

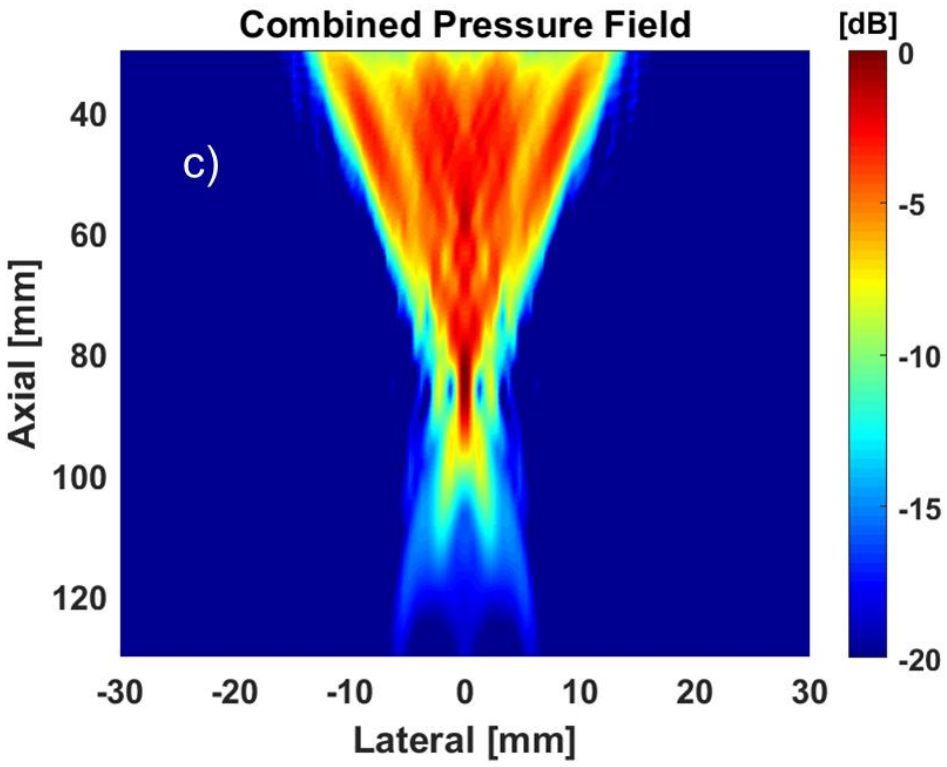

Figure 3.4: (a, b, c) Pressure field simulation for 3 foci, 4 foci, and the combined beam using Field II.

There are two metrics to determine the quality of multi-foci beamforming which are the depth of field and the lateral beam width. Depth of field is plotted along the axial axis at the center of the transducer geometry while lateral beam width is plotted along the lateral direction where the maximum pressure is recorded along the axial axis or at an axial depth of preferred choice. Figure 3.5(a, b, c) shows the depth of field plot for 3 foci, 4 foci, and the combined beam. The -6-dB depth of field estimate for 3 foci was 60 mm, stretched from 34 mm to 94 mm in the axial direction. For 4 foci beam, -6-dB depth of field estimate was 20 mm, stretched from 74 mm to 94 mm. The -6-dB depth of field estimate for the combined beam was 62 mm, stretched from 34 mm to 96 mm.

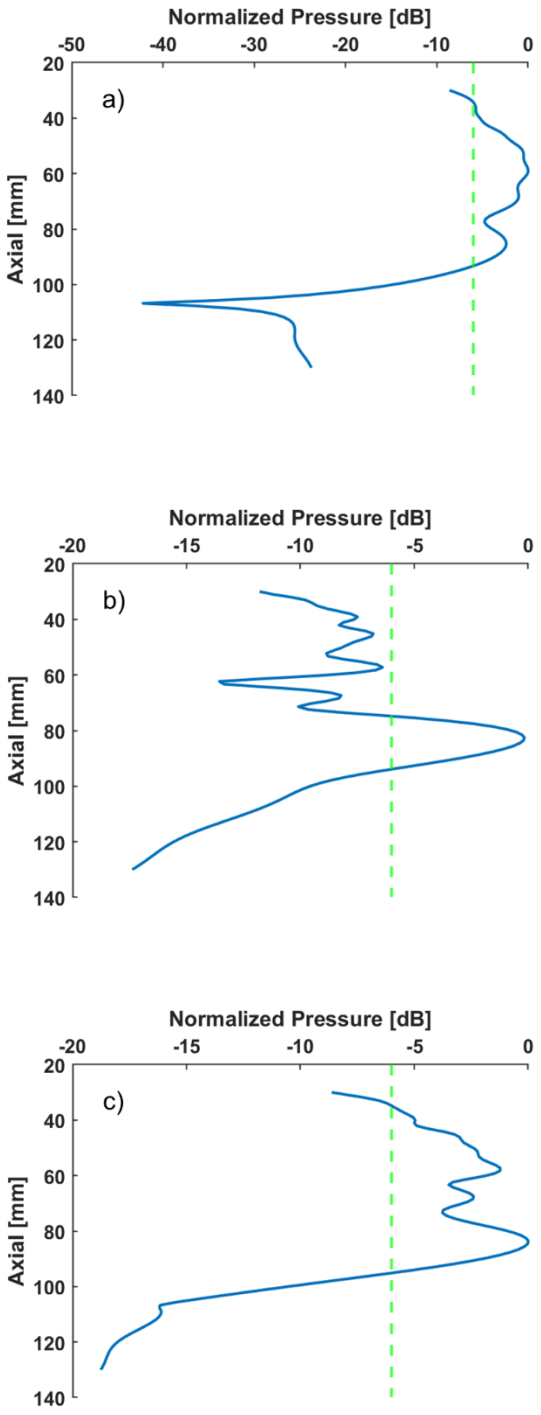

Figure 3.5: (a) The -6-dB depth of field estimate for 3 foci was 60 mm, stretches from 34 mm to 94 mm in the axial direction. For 4 foci beam, -6-dB depth of field estimate was 20 mm, stretches from 74 mm to 94 mm. The -6-dB depth of field estimate for the combined beam was 62 mm, stretches from 34 mm to 96 mm.

Figure 3.6 (a, b, c) shows the lateral beam width plot for 3 foci, 4 foci, and for the combined beam at an axial depth of 60 mm. From Figure 3.6(a) it can be observed, the -6-dB lateral beam width estimate for 3 foci is difficult to establish due to the fact that the pressure oscillates across the -6-dB threshold. Similarly, this scenario exists for the 4 foci beam as the pressure also oscillates across the -6-dB threshold as shown in Figure 3.6(b). However, on combining the 3 foci and 4 foci beam, results in a widened lateral beam width and pressure fluctuations across the -6-dB threshold are diminished. The -6-dB lateral beam width estimate for the combined beam was 11 mm and ranges from -5.5 mm to +5.5 mm.

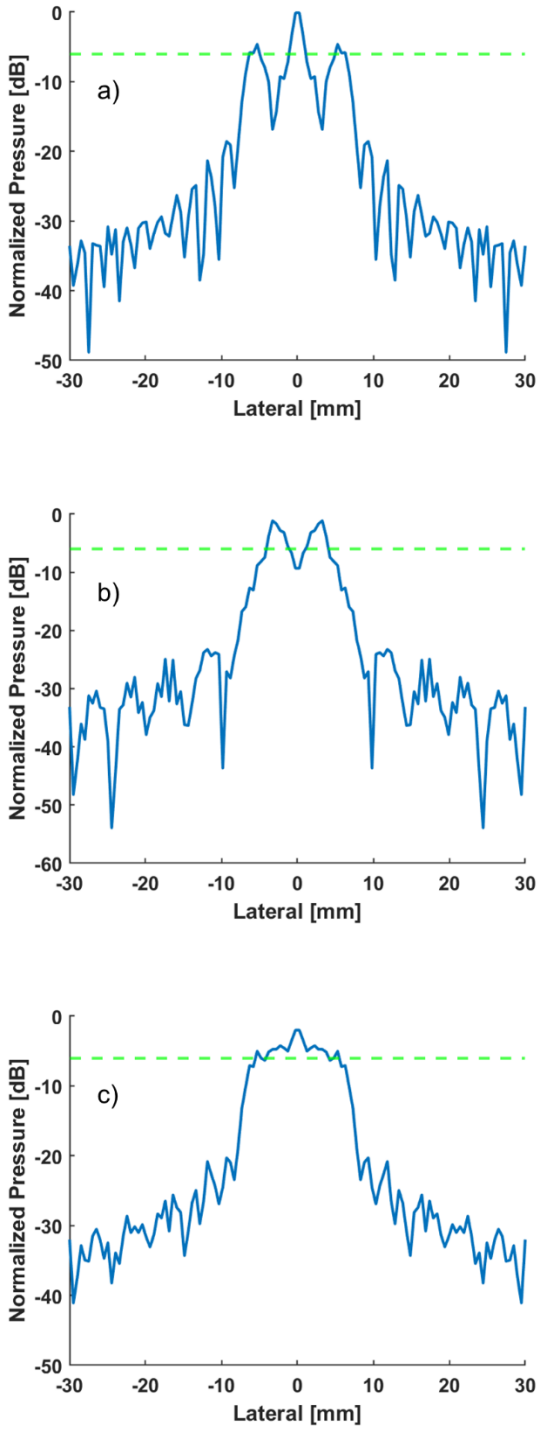

Figure 3.6: (a, b) For 3 foci and 4 foci, the pressure oscillates across the -6-dB threshold. Thus, difficult to determine the lateral beam width. However, on combining the 3 foci and 4 foci beam, the -6-dB lateral beam width estimate for the combined beam was 11 mm and ranges from -5.5 mm to +5.5 mm.

Nguyen implemented a different sub-aperture configuration for 3 foci and 4 foci for a linear array transducer in [59, 60]. The 3 foci sub-aperture configuration was [34 30 34] and [34 30 30 34] for 4 foci sub aperture. For the 3 foci sub aperture the first 15 elements and the last 15 elements were not utilized [59, 60]. Figure 3.7 summarizes the results of the sub-aperture configuration in [59, 60] implemented for a curved linear array geometry. For the 3 foci sub-aperture, the lateral focus was still kept at [-4.40 0.00 4.40] and for the 4 foci sub-aperture the lateral focus was also the same [-6.60 -2.20 2.20 6.60]. The axial focus for the 3 foci sub-aperture and for the 4 foci sub-aperture was also fixed at 70 mm. There are fluctuations in pressure along the depth of field and the lateral beam width for the combined beam across the -6-dB threshold.

It is noteworthy to mention that there is no mathematical equation or function that can determine the aperture division for multi-foci beamforming. The division of transducer aperture into sub apertures and selection of axial and lateral focus is an iterative approach. This requires multiple iterations in order to optimize the area for heating. The best overall combined beam was selected using quantitative metrics that would maximize the depth of field and the lateral beam width.

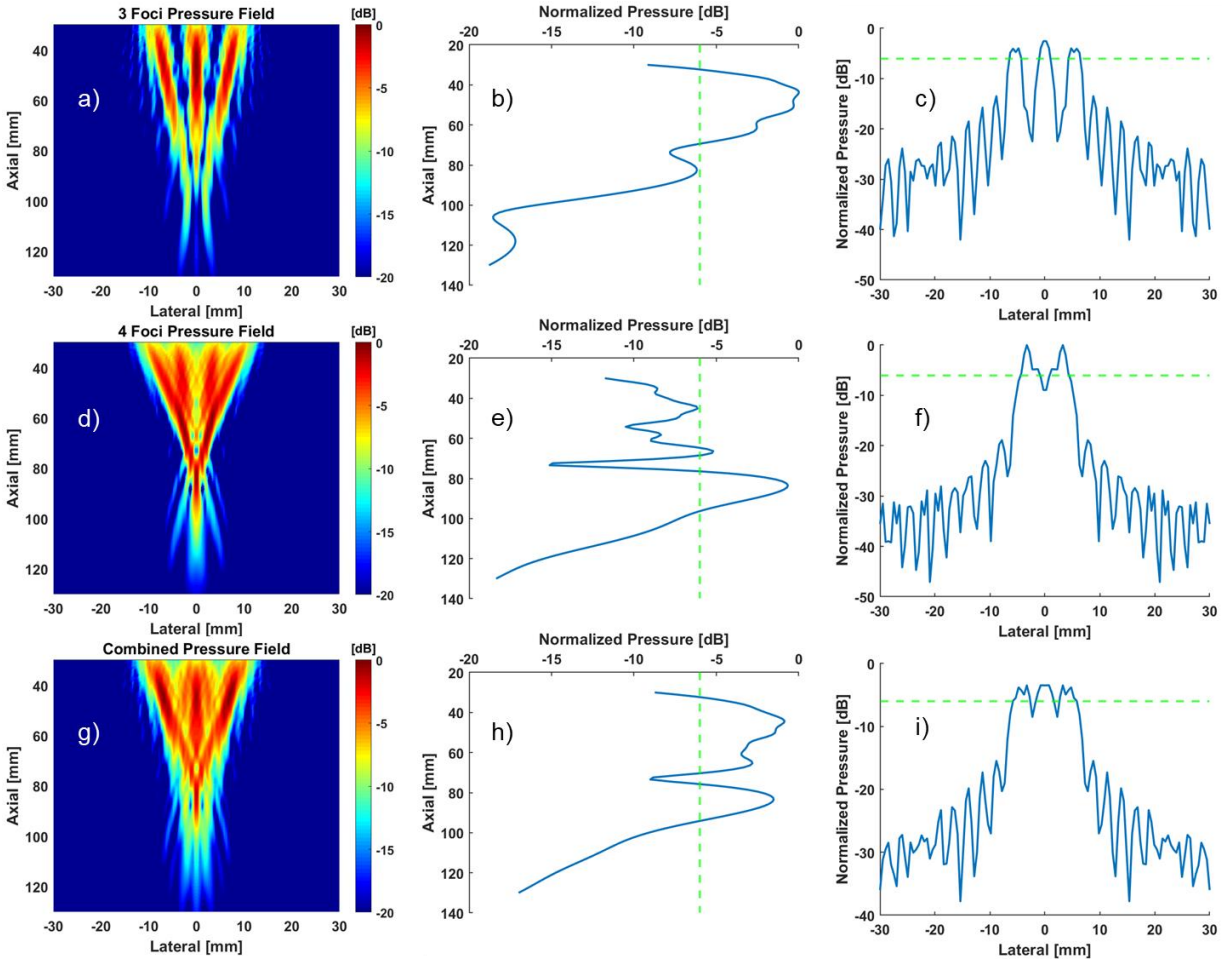

Figure 3.7: (a, d, g) Pressure field simulation for 3 foci, 4 foci, and the combined beam using Field II. The 3 foci sub-aperture was [34 30 34] and [34 30 30 34] for 4 foci sub aperture. (b, e, h) Depth of field plots for 3 foci, 4 foci, and the combined beam. (c, f, i) Lateral beam width for 3 foci, 4 foci, and the combined beam. There are fluctuations in pressure along the depth of field and the lateral beam width for the combined beam across the -6-dB threshold.

3.4 Conclusion

In this chapter, we introduced multi-foci beamforming and outline the preliminary steps for simulating the pressure field. These novel multi-foci beams create a homogeneous region for heating. This is due to the fact of allowing the transducer aperture to be divided into a three sub-aperture and a four sub-aperture. We also introduced the quality metrics that are pivotal in determining the area of the heating region. In the next chapter we examine a modification to the current design where each of the sub-aperture has a different lateral and an axial focus, that results in an extended area for heating compared to the stated design.

4.0 Multi-Foci Thermal Strain Imaging Using A Curved Linear Array Transducer for Identification of Lipids In Deep Tissue

4.1 Introduction

Nonalcoholic fatty liver disease (NAFLD) is the most common chronic liver disease among children and adults in the United States and its prevalence is growing in the world. In less than a decade, NAFLD will likely become the number one cause of liver transplants in the United States. Currently it affects an estimate of 80 to 100 million people in the country [74].

NAFLD encompasses a disease spectrum of liver conditions ranging from simple steatosis (SS) to nonalcoholic steatohepatitis (NASH). SS is a benign form of NAFLD, characterized by the accumulation of lipid in the liver. On the other hand, NASH is defined by hepatic steatosis with cell injury, hepatic ballooning and various degrees of fibrosis. NASH may further develop into cirrhosis, liver failure and hepatocellular carcinoma (HCC) [29].

Currently, liver biopsy is the gold standard for diagnosing nonalcoholic fatty liver disease [14]. However, liver biopsy is invasive in nature and suffers from medical complications such as perforation and bleeding. Additionally, needle biopsy is a poor screening tool that is not appropriate for longitudinal monitoring or evaluating diagnosis in response to treatment [30]. Because of the limitations of liver biopsy, there has been an increase in research for noninvasive methods for diagnosing NAFLD. Noninvasive methods include imaging modalities such as computed tomography (CT), magnetic resonance imaging (MRI) and ultrasound (US) [32]. CT is considered an unacceptable imaging modality for diagnosing NAFLD due to the fact that it

exposes patients to high dose of ionizing radiation and remains a poor screening tool among children. CT displays a broad spectrum of sensitivity (54-93%) and high specificity (95-100%) for diagnosing NAFLD [33]. Currently, MRI is known to be the most accurate imaging modality for diagnosing NAFLD and quantification of lipid accumulation in liver. MRI measures proton-density fat fraction (PDFF) which is a measure of fractional lipid content [75]. For detecting NAFLD, the average sensitivity of MRI ranges from 82.0% to 97.4% and the average specificity ranges from 76.1% to 95.3% [34]. However, MRI has several limitations including contra-indications, higher costs associated with scanning and is not easily available in remote clinics.

Conventional ultrasound remains the preferred choice among radiologists for diagnosing NAFLD but assessment for ultrasound remains qualitative and is dependent upon the expertise and experience of the physician [39]. A wide range of sensitivities (60–94%) and specificities (66–95%) for diagnosing NAFLD have been reported for ultrasound [40]. There exists a strong need for a noninvasive, precise and an inexpensive screening technology to accurately detect and quantify the degree of steatosis in liver because of lipid deposition.

Several intravascular imaging methods have recently been used for plaque imaging. The most frequently used for minimal invasive imaging modality for vessel wall anatomy is intravascular ultrasound (IVUS) imaging. In IVUS images, lipid-rich cores of atherosclerotic plaques appear hypoechoic. Because of the low contrast between lipid-rich plaques and other healthy tissues, additional techniques are utilized for clear distinction [76]. For example, intravascular elastography can help differentiate fatty from fibrous plaques based on the tissue strain and displacement [77].

Virtual histology intravascular ultrasound (VH-IVUS) provides information on tissues based on the IVUS signal, but therapeutic effectiveness has not been thoroughly validated for

plaque analysis [78, 79]. Intravascular optical coherent tomography (IV-OCT) provides high-resolution superficial images which are adequate to determine the thickness of the fibrous plaque [80, 81]. However, IV-OCT suffers from poor imaging depth and the composition of the plaque is difficult to discern [82]. Currently, intravascular photoacoustic (IVPA) imaging is being extensively studied to provide physiological information based on tissue optical properties and to reveal tissue structural information when combined with IVUS or IV-OCT [83, 84]. On the other hand, it is difficult to acquire a 1210-nm or 1720-nm pulsed laser source for lipid imaging. There are several groups developing new laser sources for lipid imaging, but they are pricey, bulky, and not readily available [85-87]. Photothermal strain imaging (pTSI) is based upon the dependence of speed of sound on temperature for different types of tissues [88]. Conventional TSI methods use microwaves or US as heat sources, while pTSI uses a relatively inexpensive, commercially available continuous-wave (CW) laser as a heat source. A major drawback with pTSI is the long heating time (1 minute) required to raise the temperature of the tissue. This may influence heat conduction into the surrounding tissue and may pose a problem during clinical trials as patients may not be able to hold their breath for such long durations to compensate for breathing motion [88].

Thermal strain imaging (TSI) is primarily used for non-invasive thermometry [43] and distinguishing lipids from water bearing tissues [44-46, 48]. TSI is an ultrasound-based imaging modality centered upon the principle that the speed of sound in a medium is dependent upon temperature. Lipids depict a decreasing sound speed with an increase in temperature whereas water bearing tissues exhibit an increasing sound speed with an increase in temperature [21, 22]. The derivative of the temporal echo shifts due to change in temperature and is within the safety limit of less than 2°C that yields the thermal strain. Triglycerides content is quantified from TSI with

areas of positive thermal strains as opposed to water bearing tissue which is registered as a negative strain.

TSI has proven its worth in identifying lipid from water bearing tissues in rabbit atherosclerotic plaques model and quantification of liver fat in ob/ob or obese mice [46, 48]. TSI has successfully been implemented on a single, commercially available clinical linear array transducer (Philips ATL L7-4) using novel beamforming technique called multi-foci beamforming to detect lipids in excised human atherosclerotic plaques [59, 60]. Ultrasound probes, depending on the region of interest being examined, comes in different shapes and sizes. Linear array transducers are primarily designed for imaging shallower organs or small structures whereas curved linear array transducers are designed for abdominal imaging based on the geometry and center frequency of the transducer. However, TSI has not yet been implemented on a curved linear array transducer to image abdominal organs.

In this paper, we implement multi-foci beamforming on a single commercially available curved linear array transducer to be used for imaging and heating of abdominal viewing. This was achieved by simulating pressure fields and correlating the results with hydrophone measurements followed by exhibiting the results on tissue-mimicking gelatin phantoms with a rubber inclusion that mimics lipid contents in terms of sound speed change in response to temperature modulation and liposuction fat present inside. A successful implementation of this technology would be beneficial for prognosis and monitoring of abdominal organs which are prone to accumulation of fat such as NAFLD.

4.2 Material and Methods

4.2.1 Background

The governing equation for TSI is as follows:

$$\frac{du}{dz} = (\beta - \lambda)\Delta T \qquad (4\text{-}1)$$

where du/dz is called thermal strain. This is the derivative of the apparent displacement, u, in the direction of wave propagation (axial direction, z) due to the increase in temperature, ΔT. λ [°C−1] is the linear coefficient for sound speed vs. temperature and β [°C−1] is the linear coefficient of thermal expansion. ΔT [°C] is the temperature change in the tissue. For temperatures less than 50°C, the linear coefficient of thermal expansion β has an order of magnitude much smaller than λ and can therefore be ignored [47]. Thus, the principal equation for TSI becomes:

$$\frac{du}{dz} = -\lambda\Delta T \qquad (4\text{-}2)$$

At normal body temperature (37°C), for water bearing tissues λ is positive with typical values varying between 0.7 x 10^{-3} to 1.3 x 10^{-3} and for lipid bearing tissue λ is negative with typical values varying between −1.3 x 10^{-3} to −2.0 x 10^{-3} [23]. β is about one tenth of λ for water bearing tissue with values varying between 7.0 x 10^{-5} to 1.3 x 10^{-4} and for lipid bearing tissue β has values varying between 1.3 x 10^{-4} to 2.0 x 10^{-4} [89].

4.2.2 Design of ultrasound heating beam

Single focus beamforming utilizes all the transducer elements to focus at a solo axial and lateral position. Single focus beamforming results in a much lesser area for heating. On the contrary, for TSI, a wide heating ultrasound beam is preferred to form a large area for heating. This means an ultrasound beam with a larger depth of field and a broad lateral beam width is desired [52]. For linear arrays the -6-dB lateral beam width (BW) and depth of field (DOF) can be approximated from the following equations, assuming linear propagation [72]

$$\mathrm{BW} = \lambda\left(\frac{Z_f}{D}\right) = \lambda\,.\,(F/\#) \qquad (4\text{-}3)$$

$$\mathrm{DOF} = 8\lambda\left(\frac{Z_f}{D}\right)^2 = 8\lambda.\,(F/\#)^2 \qquad (4\text{-}4)$$

where λ [mm] is the ultrasound wavelength, Z_f [mm] is the focal depth and D [mm] is the width of the active aperture. From the equations above, it can be determined that when dividing the transducer elements into sub apertures, at a specific frequency and at a fixed depth, the f-number increases. Ultimately this leads to an increase in the lateral beam width and depth of field.

Multi-foci beamforming consists of dividing the transducer aperture, first into three sub-apertures, then into four sub-apertures. A separate delay profile is applied to each sub-aperture. Figure 4.1(a, b) shows the sub-aperture configuration for 3 foci and 4 foci. The 3 foci sub-aperture consists of dividing the transducer aperture as 42-44-42 and the 4 foci sub-aperture consists of dividing the transducer aperture as 20-44-44-20. Each of the sub-aperture has a different lateral focus. Figure 4.1(c, d) shows the lateral and axial focus for each of the sub-aperture. For the 3 foci sub-aperture, the lateral focus was at [-4.40 0.00 4.40] and for the 4 foci sub-aperture the lateral focus was at [-6.60 -2.20 2.20 6.60]. The lateral focus for 3 foci beam was located between the

lateral focus for 4 foci beam. As a result, the cumulative heating beam width is equal to a seven foci beam. The 3 foci and 4 foci beams are temporally interleaved creating a uniform area for heating resulting in an extended area for heating as shown in Figure 4.2. The axial focus for the 3 foci sub-aperture and for the 4 foci sub-aperture was fixed at 70 mm, equivalent to the elevation focus of the Philips ATL C4-2 transducer.

Multi-foci beamforming has previously been implemented on a linear array transducer, Philips ATL L7-4, for identification of atherosclerosis plaque in human carotid endarterectomy specimen [59, 60].

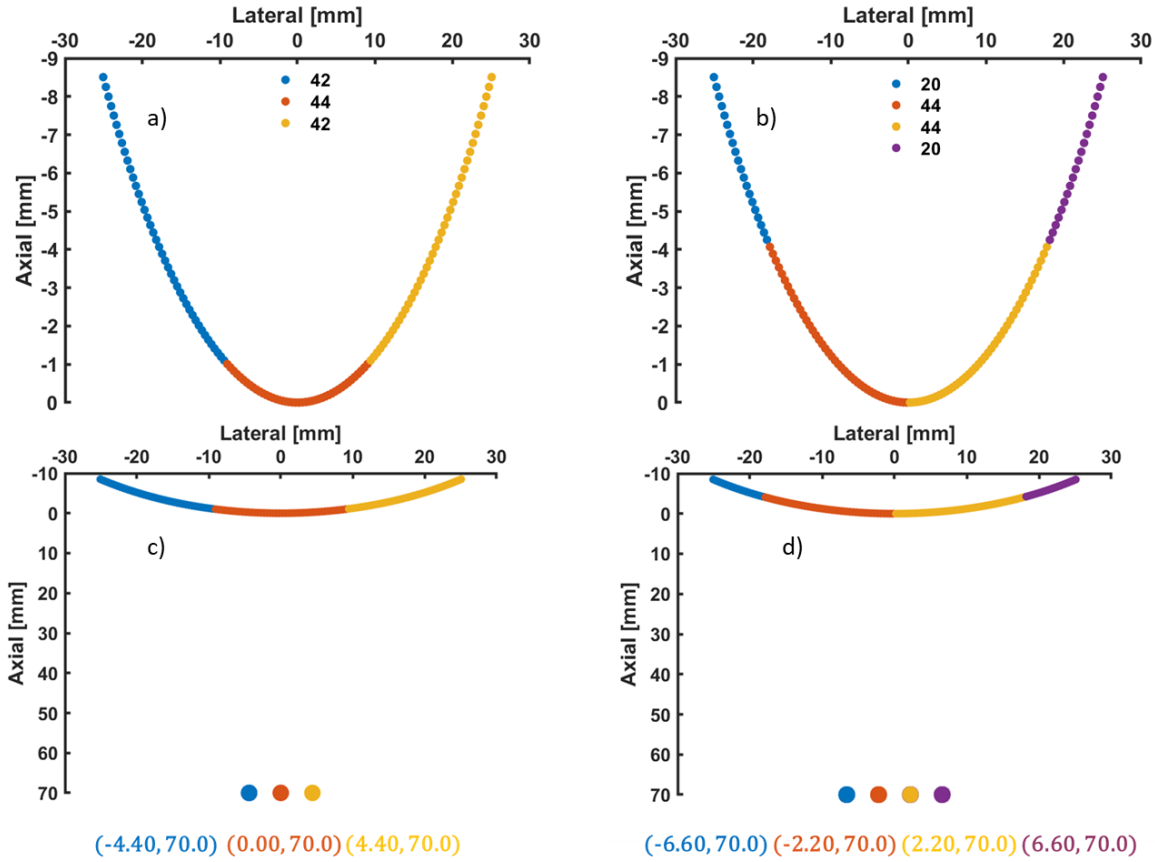

Figure 4.1: Transducer array geometry for a curved linear array transducer, Philips ATL C4-2 in the x-z plane. This transducer consists of 128 elements. (a) The 3 foci sub-aperture consist of dividing the transducer elements as 42-44-42 and (b) the 4 foci sub-aperture consist of dividing the transducer elements as 20-44-44-20. (c) The lateral focus for 3 foci sub-aperture was at [-4.40 0.00 4.40] and for the 4 foci sub-aperture the lateral focus was

at [-6.60 -2.20 2.20 6.60] (d). The axial focus for the 3 foci sub-aperture and for the 4 foci sub-aperture was fixed at 70 mm.

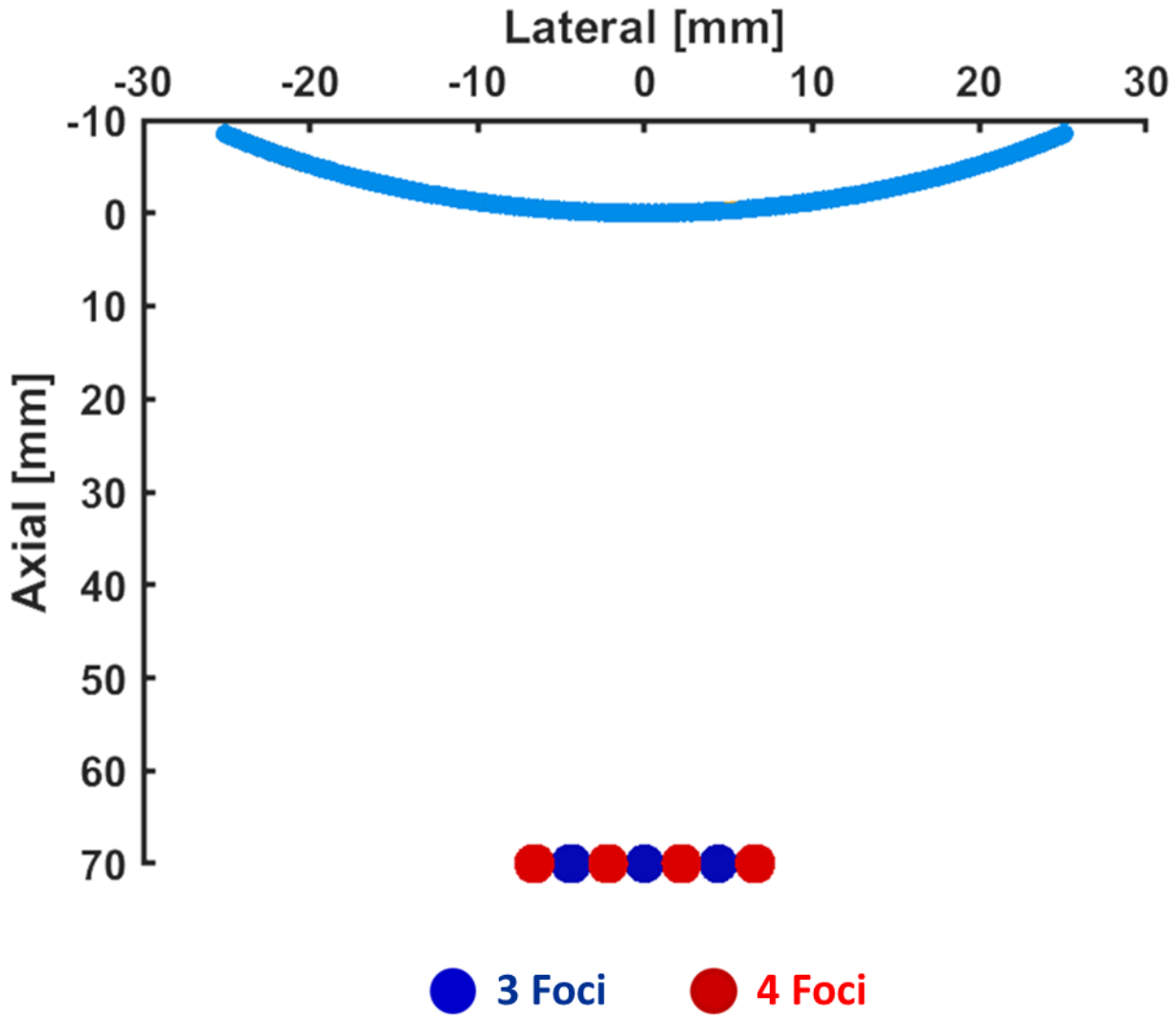

Figure 4.2: The 3 foci and 4 foci beams are temporally interleaved resulting in an extended area for heating.

4.2.3 Sub-aperture configuration

For single focus beamforming, the axial focus was set at 70 mm which is equal to the elevation focus of the transducer and the lateral focus was set at 0 mm. For multi-foci

beamforming, the 3 foci sub-aperture consists of dividing the elements as 42-44-42 and the 4 foci sub-aperture consists of dividing the elements as 20-44-44-20. To maximize the heating area in the far field, the axial focus for the 3 foci sub-aperture was changed to [69.0 70.0 69.0] as show in Figure 4.3(c). The axial focus for the 4 foci sub-aperture was changed to [74.0 72.5 72.5 74.0] and the lateral focus was changed to [-2.30 -1.90 1.90 2.30] as show in Figure 4.3(d). Each of the sub-apertures has a unique lateral and axial foci to broaden the heating beam to cover a much larger region. Figure 4.3(a, b) shows the aperture division for 3 and 4 foci beams. Once the sub-aperture configuration for 3 and 4 foci beams were finalized, delay curves were computed and then pressure fields were simulated by using the acoustic simulation package, Field II [73]. Table 4.1 lists the parameters for Field II simulation.

Table 4.1: Parameters for Field II simulation

Parameter	**Value**
Number of elements	128
Center frequency	3.0 MHz
Sampling frequency	12 MHz (200 MHz for Field II)
Azimuthal element pitch	0.4246 mm
Elevation element height	13 mm
Radius	41.219 mm
Kerf	0.05 mm
Attenuation	0.5 dB/cm/MHz
Sub-aperture size	42-44-42 (3 foci beam) 20-44-44-20 (4 foci beam)
Grid size	200 × 200 (X × Z)

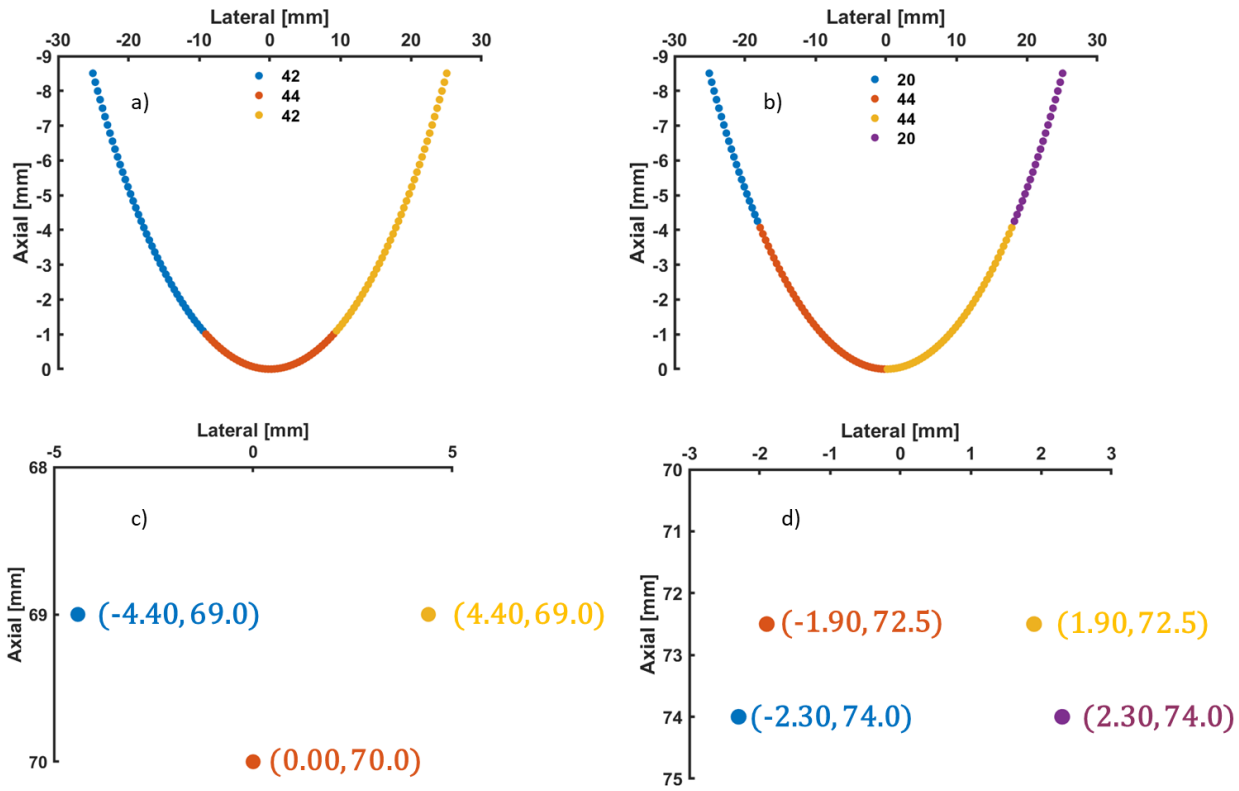

Figure 4.3: (a) The 3 foci sub-aperture consist of dividing the transducer elements as 42-44-42 and (b) the 4 foci sub-aperture consist of dividing the transducer elements as 20-44-44-20. (c) The lateral focus for 3 foci sub-aperture was at [-4.40 0.00 4.40] and the axial focus was [69.0 70.0 69.0]. (d) The lateral focus for 4 foci sub-aperture was at [-2.30 -1.90 1.90 2.30] and the axial focus was [74.0 72.5 72.5 74.0].

4.2.4 Delay curve calculation

Assuming the transducer element T_0 generates a pulse at t = 0, we would have to determine the firing times for the remaining elements for the sound waves to be in-phase at the focal point. The first step in determining the time delay is to calculate the distance from the transducer elements to the focal point by using the Euclidean distance formula.

$$d_i = \sqrt{(x_i - x_f)^2 + (z_i - z_f)^2} \qquad (4\text{-}5)$$

where (x_f, z_f) is the lateral and axial coordinate of the focal point and (x_i, z_i) is the lateral and axial coordinate of the i^{th} transducer element.

The next step is to determine the time it takes for the ultrasound wave to reach the focal point, assuming the speed of sound in soft tissue is c = 1540 ms^{-1}, by using the following equation.

$$t_i = \frac{d_i}{c} \qquad (4\text{-}6)$$

After determining the triggering time, the time delays are given by the following equation.

$$\tau_i = t_{max} - t_i \qquad (4\text{-}7)$$

4.2.5 Hydrophone measurements

The design for multi-foci heating beams were then executed on a research ultrasound scanner (Verasonics Data Acquisition System [VDAS] Vantage Model, Verasonics, Kirkland, WA, USA) connected to a curved linear array transducer, Philips ATL C4-2. The pressure field from the Philips ATL C4-2 transducer was measured in a water tank using a hydrophone (HGL0200, Onda, Sunnyvale, CA, USA) connected to a computer controlled translational stage. The hydrophone maneuvered in a 2-D rectangular plane, with an axial dimension starting from 30 mm to 100 mm with a step size of 1 mm and a lateral range from -30 mm to 30mm with stepper increments of 0.5 mm for generating the pressure field.

4.2.6 Temperature rise simulation

Temperature rise during TSI was simulated using Comsol software (Comsol Multiphysics Version 5.1, Comsol, Burlington, MA, USA). Assuming linear propagation, the acoustic pressure field was first derived using Field II. The acoustic intensity is computed using the acoustic pressure field and is calculated from the following equation:

$$I = \frac{P^2}{2\rho c} \qquad (4\text{-}8)$$

where I [W/cm^2] is the acoustic intensity magnitude, P [MPa] is the acoustic pressure amplitude, ρ [kg/m^3] is the density and c [m/s] is the speed of sound.

The amount of heat deposited, Q, into the tissue is calculated using the following equation:

$$Q = 2\alpha I \qquad (4\text{-}9)$$

where α [Np/cm] is the absorption coefficient for tissue and I [W/cm^2] is the acoustic beam intensity**.**

A tissue phantom model and a model that portrays material properties of fat was developed using Comsol. These models were imported into MATLAB to simulate the thermal map. To model the heat transfer within biological tissue, Penne's bioheat transfer equation (BHTE) is used.

$$\rho C_p \frac{\partial T}{\partial t} = \nabla.(k\nabla T) - \rho_b C_b w_b (T - T_b) + Q + Q_{met} \qquad (4\text{-}10)$$

where T is the temperature, ρ is the density, C_p is the specific heat, k is the thermal conductivity, ρ_b is the density of blood, C_b is the specific heat of blood, w_b is the blood perfusion rate, T_b is the temperature of the blood, Q is the heat deposition, the absorbed ultrasound energy

calculated from the above stated equation and Q_{met} is the metabolic heat source. Table 4.2 lists the input parameters for the BHTE simulation.

Table 4.2: Parameters for penne's bioheat transfer equation

Parameter	Tissue Phantom	Fat
Center frequency (MHz)	3.0	3.0
Initial Temperature (°C)	24	24
Heating Duration (°C)	2.0	2.0
Cooling Duration (°C)	2.0	2.0
Density of tissue (kg/m3)	1044	900
Speed of Sound (m/s)	1540	1450
Attenuation (Np/m/MHz)	8.55	9.0
Specific Heat (J/(kg.K))	3710	3411
Thermal Conductivity (W/(m.K))	0.59	0.5

For a detailed understanding on the construction of tissue phantom model and how heat is induced by focused ultrasound the reader is referred to [90].

Similarly, the pressure field from hydrophone was also used to simulate the temperature rise during TSI.

4.2.7 Temperature measurements

The peak pressure was recorded at an axial depth of 60 mm. The peak temperature rise during TSI was measured using a thermocouple connected to a data acquisition module (QuadTemp, Thermoworks, Lindon, UT, USA). Temperature measurements were recorded 3 times at the peak pressure (60 mm).

4.2.8 Phantom construction

A homogeneous gelatin phantom was fabricated with a rubber inclusion present inside. The reason for incorporating rubber in the phantom is that it produces a large positive thermal strain and mirrors properties of lipid (Huang et al. 2007). The homogeneous gelatin phantom was manufactured by slowly adding 50 g (5% g/mL) of gelatin from porcine skin (Sigma Aldrich Co., MO, USA) to 1000 mL of cold water. The solution was allowed to mix homogeneously till it became transparent or reached a temperature of approximately 65°C. Once the solution was clear, an additional 10 g (1% g/mL) of cellulose (Sigma Aldrich Co., MO, USA) was added. When the entire cellulose was completely dissolved, the mixture was poured into a container and kept inside a freezer at -20°C for approximately an hour to solidify. Any air bubbles present on the surface were carefully removed [91]. The homogeneous gelatin phantom was then kept outside for an adequate amount of time to bring it down to room temperature for TSI measurements. During TSI operation the transducer was firmly placed on the surface of the gelatin phantom using a clamp. The contact between ultrasound probe and gelatin surface was made using degassed water.

To further validate our technology, an additional homogeneous gelatin phantom was constructed with liposuction fat inside. Liposuction fat was obtained from a patient undergoing bilateral breast reduction and a written consent was received. Liposuction fat is a mixture of oil, fat, residual fluids and some blood particles at room temperature. It was centrifuged for 5 minutes to separate the 3 different layers. The topmost, oil layer was removed and the remaining fat was poured into a container and kept inside a -20°C freezer to allow the fat fragments to aggregate to create a single large piece of liposuction fat. The liposuction fat was later fixated in a homogeneous gelatin phantom for further testing. Similarly, the gelatin phantom was kept outside for an ample

time to bring it down to room temperature and the ultrasound transducer was clamped and coupled to the surface of the phantom using degassed water.

4.2.9 TSI pulse sequence

A typical beam sequence for TSI consists of acquiring frames before and after heating. Repeating high intensity multi-foci beam for a longer duration of 2.0 seconds led to an increase in temperature via absorption by the propagating medium. Phase based tracking algorithm, Loupas, was used to measure displacement between pre and post frames in the axial direction. The kernel size for tracking the displacement was 3.0 wavelengths. Thermal strain was computed by taking the derivative using a second order savitzky-golay filter of 15 mm in the axial direction. Thermal strain maps were color coded within the heating region so that red indicated positive strain corresponding to lipid presence and blue indicated negative strain corresponding to water bearing tissue. Figure 4.4 shows the pulse sequence for multi-foci TSI.

Focused imaging was used for acquiring B-mode images before and after heating. A F/2 configuration was used for transmission and reception of scan lines. The axial focus was set at 60 mm. The center frequency used for imaging pulses was 3.0 MHz with a pulse length of 2 cycles. The heating duration was kept at 2.0 seconds with a duty cycle of 5 %. The center frequency used for heating pulses was 3.0 MHz and the number of cycles for 3 foci and 4 foci were kept at 64.

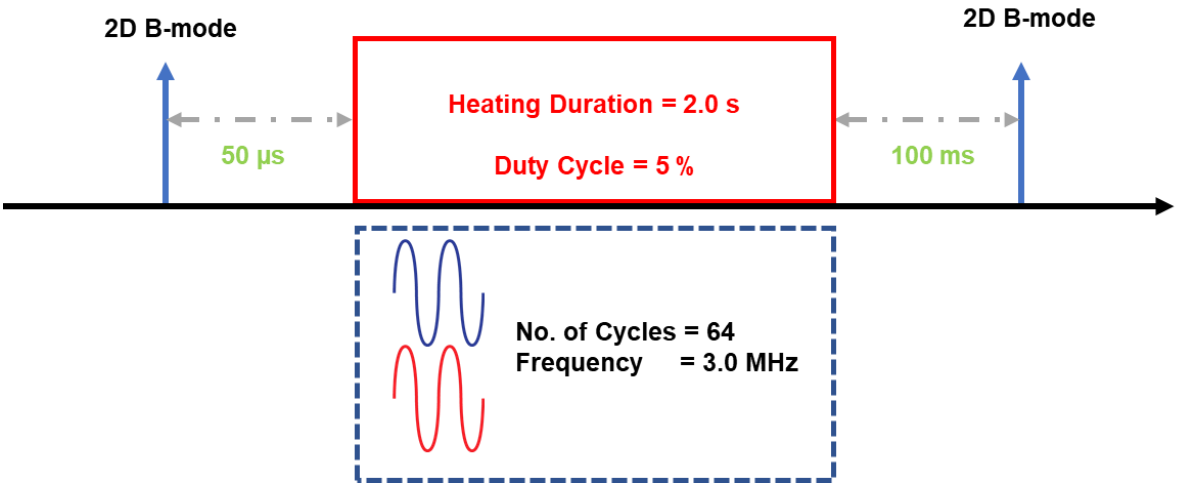

Figure 4.4: For TSI pulse sequence, repeating this high intensity multi-foci beam for a longer duration (2.0 seconds) can lead to an increase in temperature via absorption by the propagating medium.

4.2.10 Peak negative pressure (PNP)

The non-thermal effects of multi-foci beamforming were also taken into consideration. Mechanical Index (MI) was computed as it is a measure of the acoustic power of the ultrasound beam [66]. Peak negative pressure (PNP) is measured during the hydrophone experiment at the respective excitation voltage. Mechanical Index is later computed by using the equation $\mathrm{MI} = \mathrm{NPP}/\sqrt{\mathrm{centerfrequency}}$.

4.3 Results and Discussion

4.3.1 Optimization of sub-aperture configuration

It is noteworthy to mention that there is no mathematical equation or function that can determine the aperture division for multi-foci beamforming. The division of transducer aperture into sub apertures and selection of axial and lateral foci is an optimization problem. This requires multiple iterations in order to optimize the area for heating. The current design underwent multiple iterations before finalizing on the sub-aperture division and position of the axial and lateral foci. The best overall combined beam is chosen using quantitative metrics that would optimize the heating area and furthermore increase the temperature of the tissue over an extended area. The number of elements in each sub-aperture is determined by considering that fewer elements in each sub-aperture may not deposit enough energy to contribute to an increase in tissue temperature or that having a large number of elements in each sub-aperture may result in an increase in temperature (> 2 °C) that will cause adverse biological effects.

A different sub-aperture configuration for 3 foci and 4 foci for a linear array transducer was implemented in [59, 60] . The 3 foci sub-aperture configuration was [34 30 34] and [34 30 30 34] for 4 foci sub aperture. For the 3 foci sub aperture the first 15 elements and the last 15 elements were not utilized. This sub-aperture configuration was implemented for a curved linear array geometry. For the 3 foci sub-aperture, the lateral focus was kept at [-4.40 0.00 4.40] and for the 4 foci sub-aperture the lateral focus was at [-6.60 -2.20 2.20 6.60]. The axial focus for the 3 foci sub-aperture and for the 4 foci sub-aperture was fixed at 70 mm. There were fluctuations in pressure

along the depth of field and the lateral beam width for the combined beam across the -6-dB threshold.

4.3.2 Pressure field

Figure 4.5 shows the results of this design in comparison with single focus beamforming. Figure 4.5 (a, e) depicts the delay profile for multi-foci and single focus beamforming. Figure 4.5 (b, f) depicts the pressure field generated using Field II. All pressure fields generated were normalized with respect to the peak pressure.

The depth of field for multi-foci beamforming is ~64 mm (Figure 4.5(d)) which is much larger in comparison to the single focus beamforming which is 28 mm (Figure 4.5(h)). Similarly, the lateral beam width at 70 mm for multi-foci beamforming is ~13 mm (Figure 4.5(c)) which is also higher in comparison to single focus beamforming. The lateral beam width for single focus beamforming is 1.5 mm (Figure 4.5(g)).

Figure 4.6 exhibits the result of the pressure field beam pattern from simulation and from hydrophone measurements. Figure 4.7(a – c) exhibits the depth of field plot for 3 Foci, 4 Foci and combined pressure beams. The depth of field plot from simulation draws a parallel with results from hydrophone measurements. Figure 4.7(d – e) exhibits the lateral beam width plots. The lateral beam width plot for each of the beams is along the axial value where maximum pressure occurs along the depth of field. For 3 Foci beam, the maximum pressure occurs at a depth of 60 mm, 4 Foci occurs at 88 mm and the combined beam occurs at 60 mm. The lateral beam width from hydrophone measurements for each of the beams showcase a strong association with results from simulation.

At -6-dB full width half maximum (FWHM) beam width, the heating area for multi-foci beamforming for curved linear array transducer was from -7 to +7 mm in the lateral direction and 32 to 96 mm in the axial direction. Previous study by [60] demonstrating multi-foci beamforming implemented on a linear array transducer for identifying lipid rich cores in excised human atherosclerotic plaques resulted in a heating area from -4 to +4 mm in the lateral direction and 20 to 30 mm in the axial direction.

Hydrophones designed for diagnostic ultrasound can be damaged under high acoustic pressures in the near field. Therefore, the hydrophone is kept at a distance of 30 mm from the surface of the transducer, which is common to avoid irreversible damages to the hydrophone. Other alternatives such as clad needle hydrophones and optical hydrophones can be used to determine the acoustic pressure in the near field [92].

The results from multi-foci beamforming for curved linear array transducer demonstrate that scanning of organs at a deeper depth is more achievable than a linear array transducer because the liver is approximately located 40 to 50 mm below the surface of the skin [93].

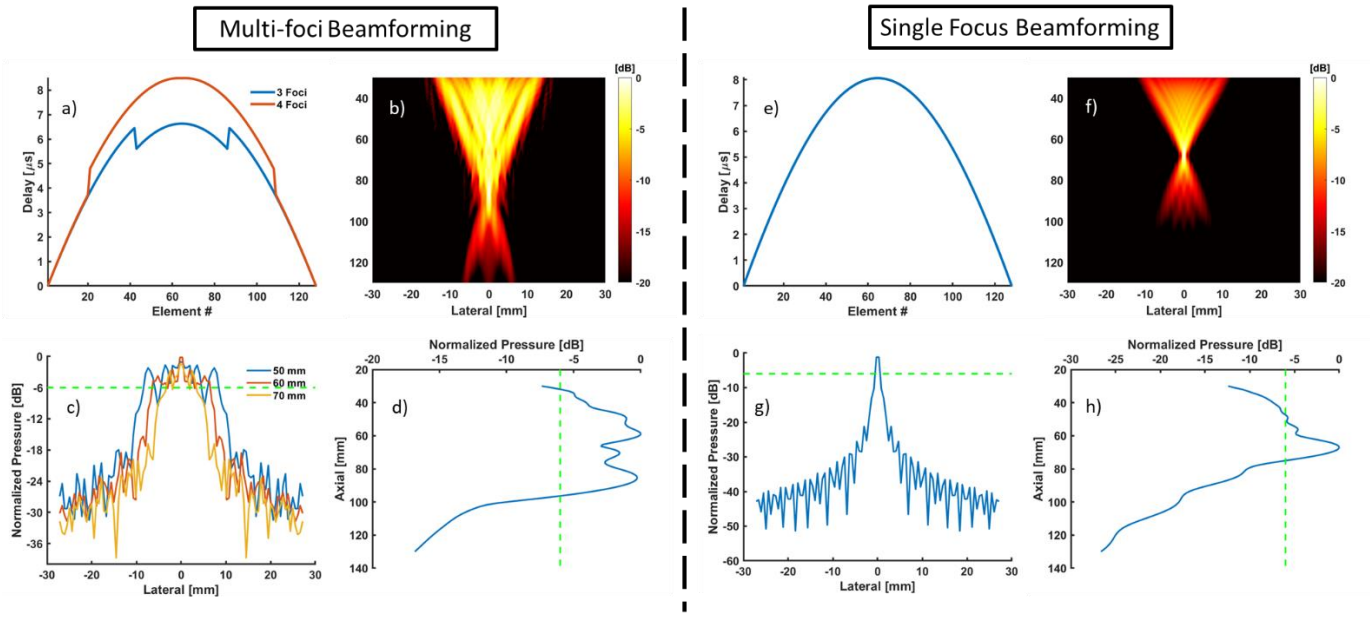

Figure 4.5: Comparison of multi-foci beamforming with single focus beamforming. (a) Delay profile for multi-foci beamforming is generated using delay and sum algorithm. (b) Pressure field is simulated with Field II, normalized to the peak acoustic pressure. The lateral beam width at various depths is shown in (c). The beam width is wider compared to single focus beamforming (g) as this is preferred for TSI. (d) The depth of field plot depicts a large depth of field compared to single focus beamforming (h). The depth of field is approximately ~ 64 mm. Single focus beamforming involves exploiting all of the transducer elements to focus at a solo axial and lateral position. The axial and lateral focus were set at 70 mm and 0 mm. (e) Delay curve for single focus beamforming and (f) Pressure field simulated with Field II normalized to the peak acoustic pressure.

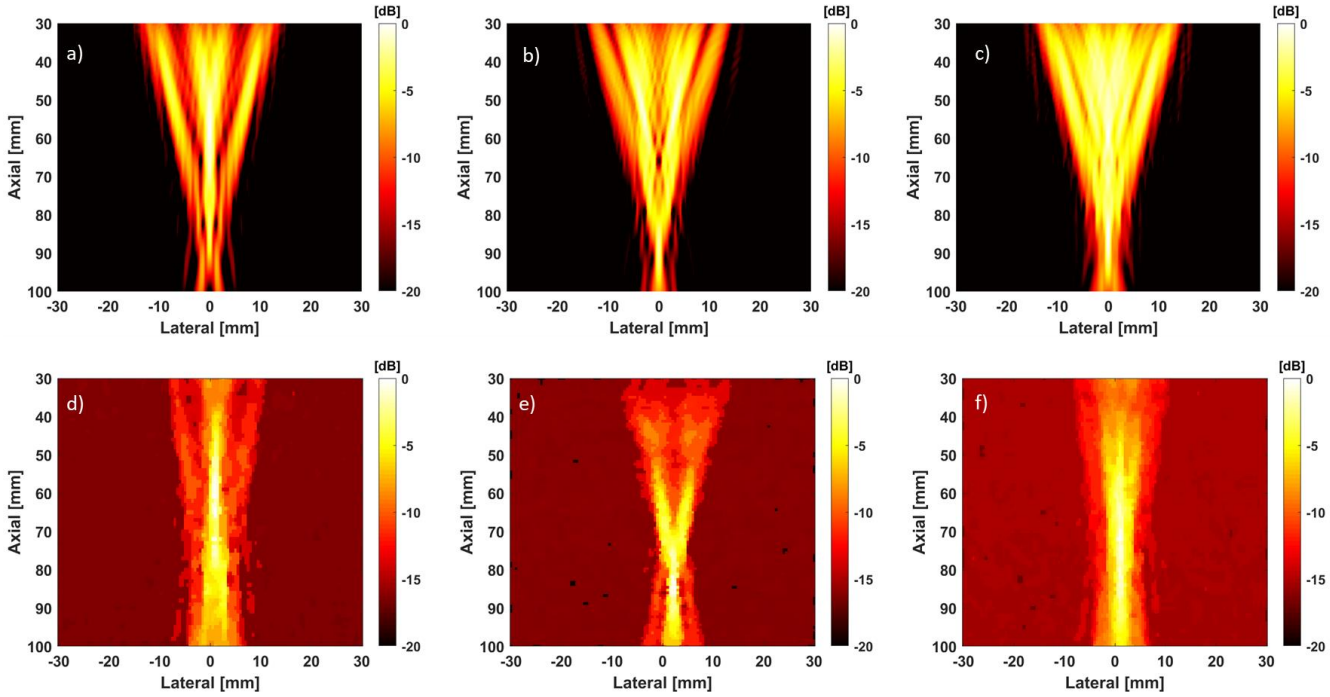

Figure 4.6: (a) – (c) Simulation results from Field II (3 Foci, 4 Foci and Combined Pressure field). (d) – (e) Results from hydrophone experiment (3 Foci, 4 Foci and Combined Pressure field).

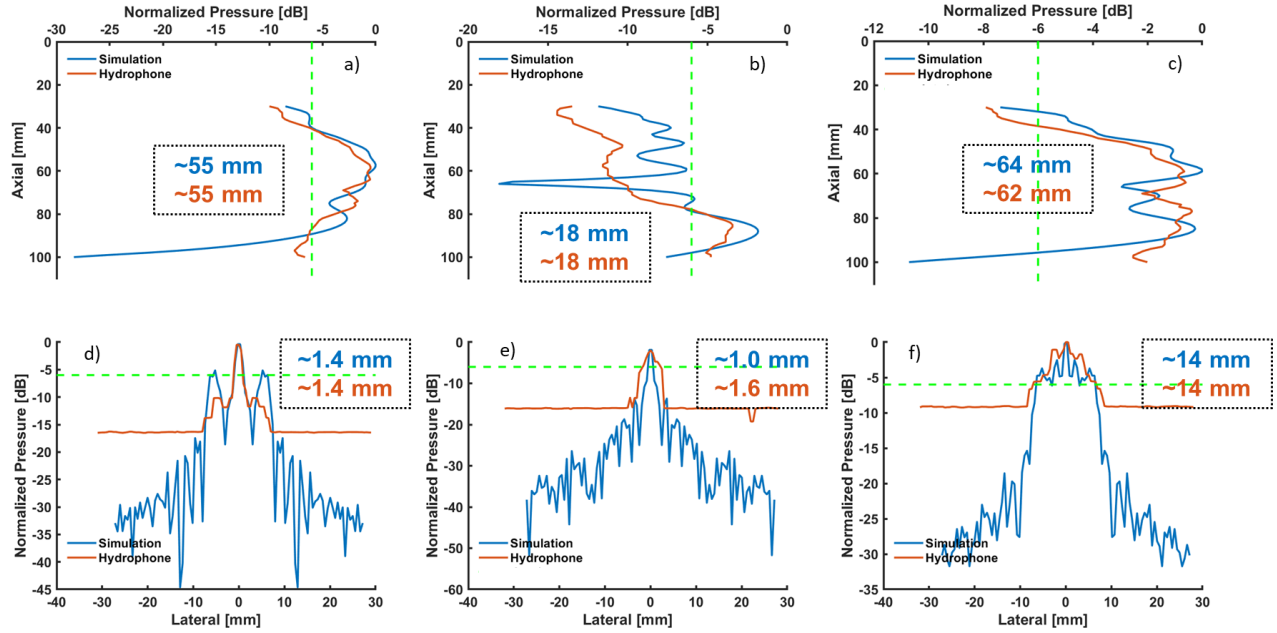

Figure 4.7: (a) – (c) Depth of field plot both for simulation and hydrophone experiment. (d) – (e) Lateral beam width plot both for simulation and hydrophone experiment.

Tissue thermal response

Figure 4.8 displays the thermal map from both simulated pressure field and hydrophone.

Figure 4.8(a) represents the simulated temperature map and (b) represents the temperature map

generated using pressure field from hydrophone for 2.0 seconds of heating. From simulation, the rise in temperature at 60 mm is ~ 1.6°C (Figure 4.8(a)) and the rise in temperature at 60 mm is ~ 1.8°C (Figure 4.8(b)).

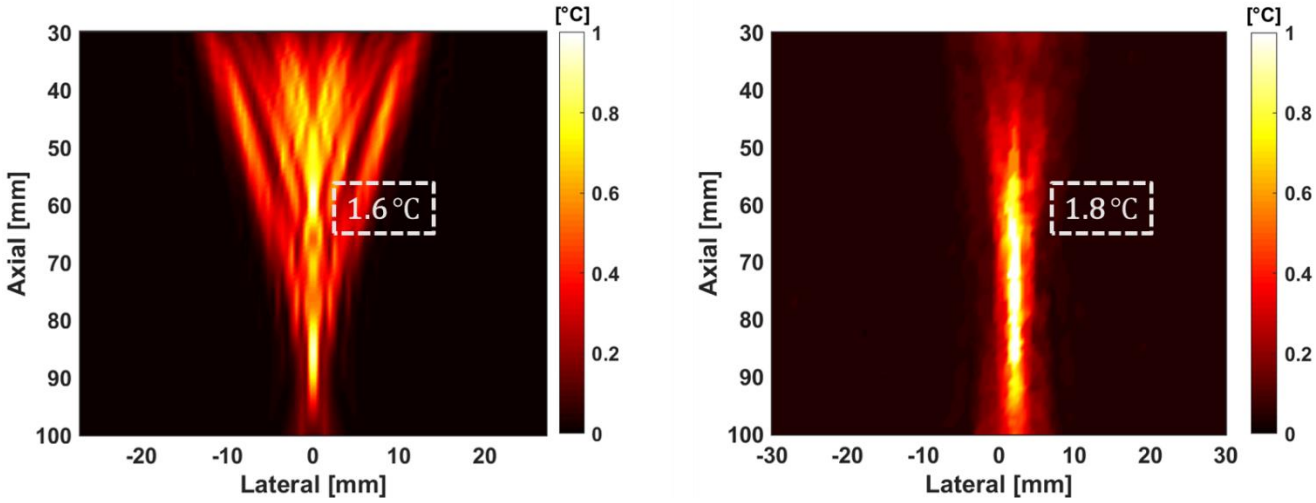

Figure 4.8: Simulation and experimental thermal results. (a) Simulated temperature map for 2.0 seconds of heating using penne's bioheat transfer equation. (b) Temperature map generated using pressure field from hydrophone as input for 2.0 seconds of heating using pen

Figure 4.9(a) displays a B-mode image of a homogeneous gelatin phantom with the tip of the thermocouple needle at 60 mm. Figure 9(b) displays the actual rise in temperature of the homogeneous gelatin phantom during TSI for 2.0 seconds of heating. The temperature rise recorded during TSI is ~1.0°C. Moreover, Figure 4.9(b) displays the simulated increase in temperature for the tissue and fat model.

The difference in temperature measurement between experimental value and the value from simulation may be due to 1) variation in tissue thermal properties of the fabricated gelatin and the tissue phantom properties from simulation and 2) conduction of heat alongside the thermocouple needle [60]. Furthermore, Penne's bioheat transfer equation assumes that 1) metabolic heat is distributed linearly within the human body, 2) tissue thermal properties do not

change, 3) blood flow rate is constant, and 4) blood temperature is constant and equal to human body temperature [94, 95]. Though, this bioheat model is the most frequently used, but Penne's assumptions do not always hold true. The rate of blood flow varies between arteries and capillaries. In addition, a lot of convective metabolic heat transfer happens through blood perfusion, and metabolic heat exchange often takes place between small and loosely spaced vessels. Ultimately, these conditions influence the model of bioheat transfer, which, in turn, does not remain valid and precise in all instances. According to the American Institute of Ultrasound in Medicine (AIUM), "there have been no significant, adverse biological effects observed due to temperature increases less than or equal to 2°C above normal, for exposure durations up to 50 hours".

Unlike previously used TSI systems, multi-foci beamforming eliminates the prerequisite of separate transducer for heating and rejects the notion for dedicated electronics. Moreover, the prospect of implementing this technology on commercially available clinical ultrasound systems is promising.

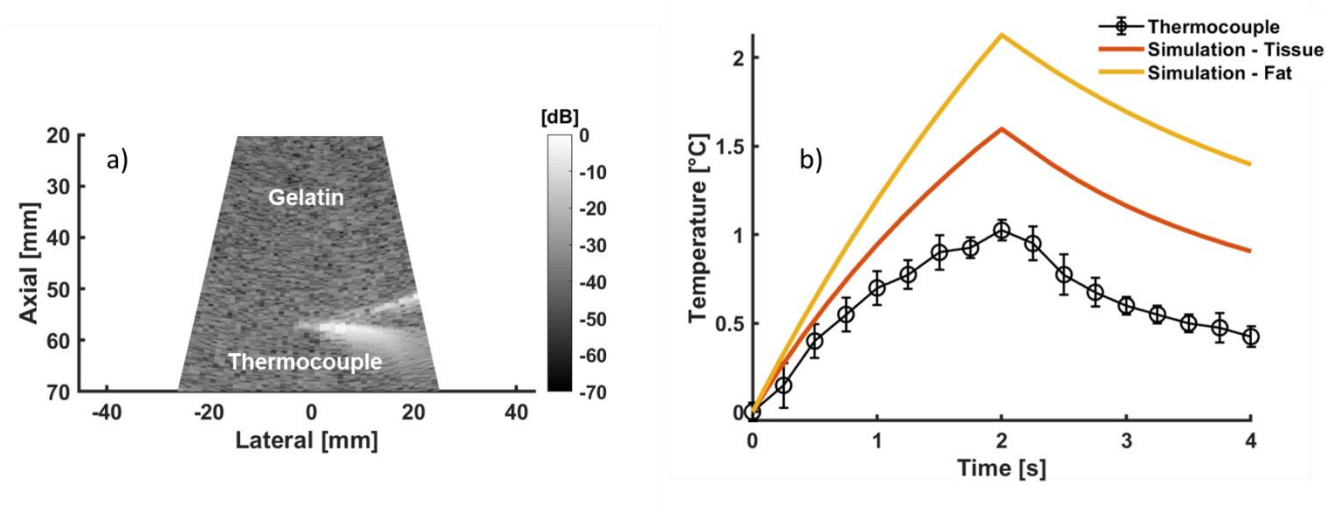

Figure 4.9: Temperature rise during TSI was recorded. (a) The tip of the thermocouple can be seen from the B-mode image. Temperature measurements were repeated 3 times at a depth of 60 mm. The peak temperature rise during TSI was 1.0 ºC as shown in (b), measured using a thermocouple. (b) Simulated temperature increase for tissue and fat model overlaid on the measured curve.

4.3.3 Phantom experiment results

Rubber—Figure 4.10(a) illustrates B-mode with rubber inclusion in the middle. The diameter (14 mm) of the rubber inclusion is equal to the lateral beam width of the heating beam at 60 mm. With a temperature increase of 1.0°C, the expected range of strains are -0.07% to -0.13% for water-bearing tissue and 0.13% to 0.2% for lipid bearing tissue, calculated using the TSI principle equation. The average strain produced in rubber is 0.6%, which is greater than the theoretical value as shown in Figure 4.10(b).

Rubber is known to have a higher thermal conductivity and absorption coefficient. These characteristics cause a greater rise in temperature and produces a much larger positive strain in rubber.

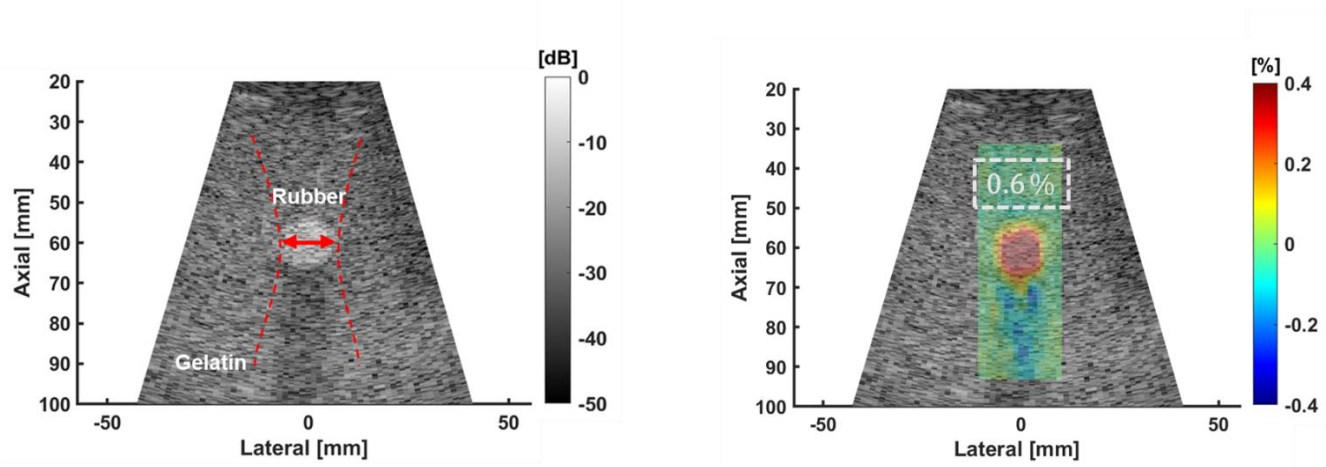

Figure 4.10: B-mode (a) and TSI image (b) of a cylindrical rubber (d = 14 mm) inclusion embedded in gelatin.

Liposuction fat— Figure 4.11(a) illustrates a B-mode with liposuction fat present inside of gelatin phantom. TSI pulse sequence was implemented on the phantom. TSI was able to distinguish the liposuction fat from the background water-based gelatin as evident in Figure 4.11(b) with an average strain of 0.16% which is in accordance with the theoretical value calculated.

To showcase that our technology can be used to diagnose real life scenarios in particular nonalcoholic fatty liver disease, we tested the efficacy of our technology on a gelatin phantom model with liposuction fat implanted inside.

The average strain reported inside the region of interest was calculated by taking an average of the number of pixels greater than a specific threshold. This threshold was determined by first measuring the root mean square (RMS) value of the non-heating region to the left and right of the heating region. The RMS value for non-heating region to the left was 0.029% and the RMS value for non-heating region to the right was 0.027%. After calculating the RMS value of the non-heating region, an average RMS value was measured. The average RMS value was 0.03%.

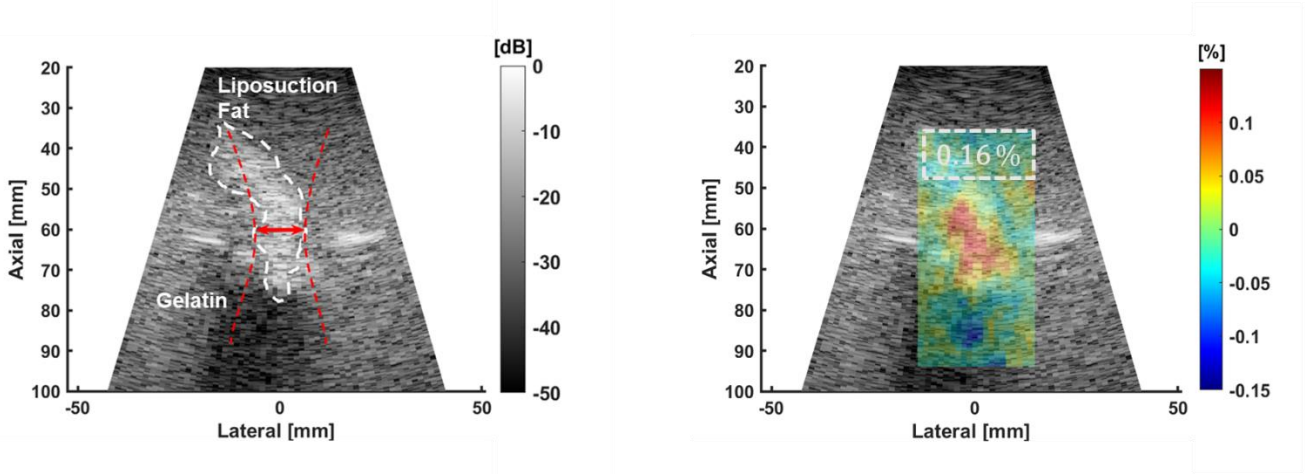

Figure 4.11: B-mode (a) and TSI image (b) of a liposuction fat embedded in gelatin.

4.3.4 Delay in TSI pulse sequence

For the TSI pulse sequence, a short time delay of 50 µs between acquiring pre-frames and heating pulse sequence was attributed due to a hardware constraint on the VDAS ultrasound scanner. This wait was to allow the hardware to transition from regular B-mode imaging profile to a high intensity focused ultrasound profile. The long delay period between heating pulse sequence and acquisition of post-frames was adopted to compensate for any motion introduced because of the acoustic radiation force [45].

4.3.5 Non-thermal effects

Figure 4.12 depicts the voltage versus PNP curve for the multi-foci heating beam. The PNP at a driving voltage of 20.0 V is 3.24 MPa. MI for the heating beam sequence is 1.8. According to the Food and Drug Administration (FDA), MI cannot exceed above the approved limit of 1.9 [67]. Moreover, MI may not be the most accurate indicator of mechanical bioeffect of ultrasound such

as cavitation. Multiple studies in water have shown that long ultrasound pulses will cause inertial cavitation (IC) activity [96, 97].

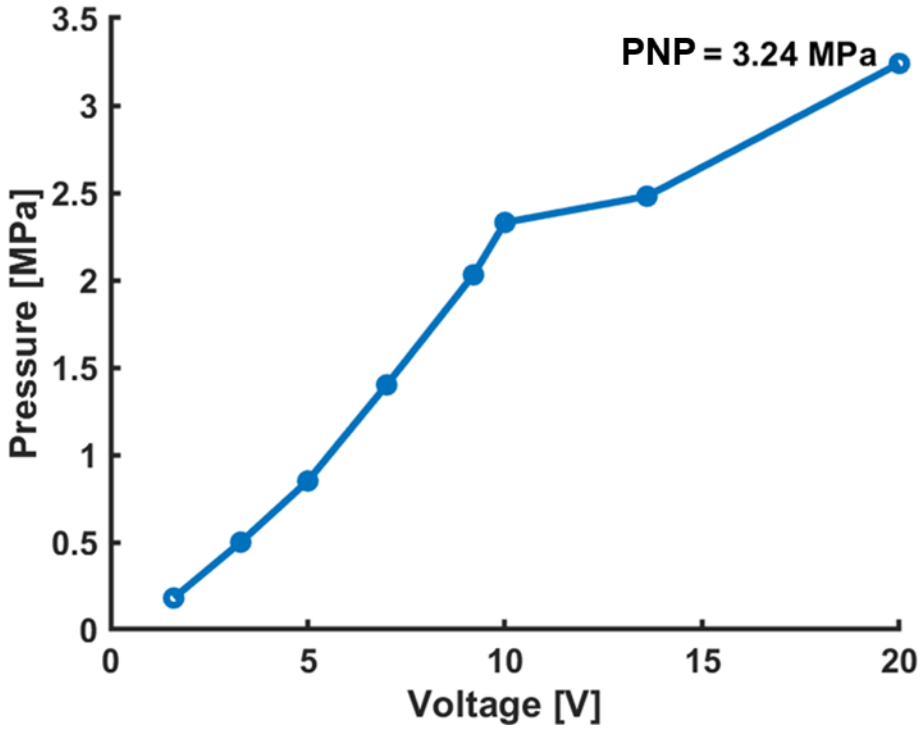

Figure 4.12: TSI pulse sequence is run at an excitation voltage of 20.0 V. Peak negative pressure (PNP) was measured in a water tank using a hydrophone. Mechanical Index (= PNP / √(*center frequency*)) was calculated to be 1.8. For clinical translation, it is necessary to have the MI below 1.9 to meet the FDA-approved limit.

4.3.6 Limitations

There are a few limitations that are needed to be taken into consideration with TSI systems for future in vivo experiments. These include potential thermal damages to transducer, physiological motion arising from breathing, cardiac pulsations and blood perfusion in the liver.

The TSI heating beams were implemented on the VDAS. The VDAS was connected to an external power source to draw more voltage from the system. This generated high intensity focused ultrasound beams increasing the temperature of the tissue via absorption by the propagating

medium. The current excitation voltage was set at 20.0 V. Driving the transducer at a high voltage for a long period of time or repeated TSI pulse sequences without any delay in between can cause severe irreversible effects to the piezo ceramic materials of the transducer elements. With advancements in transducer technology, development of new ultrasound probes for heating or acoustic radiation force impulse (ARFI) transducers will have to compensate for thermal damages to the piezo ceramic materials. A possible solution would be to design a transducer with a built-in cooling mechanism.

The naturally occurring physiological motion arising from breathing and cardiac pulsations during in-vivo testing may result in poor estimation of displacement. For a human subject study, the concern with motion arising from breathing may be resolved by requesting the patients to hold their breath for a few seconds (< 5 s). To compensate for cardiac pulsations, B-mode frames before and after heating can be synchronized with an ECG trigger.

During thermal simulation blood perfusion in the liver was not considered. For in-vivo operations, blood perfusion in liver may possibly affect the temperature of the tissue. Additional simulations should be carried out to understand the effect of blood perfusion.

The next phase of the project would involve carrying out ex-vivo experiments with excised human liver tissue embedded in gelatin. The excised human liver tissue would be attained from patients diagnosed with fatty liver disease. However, for in-vivo testing on patients diagnosed with fatty liver disease, further investigation needs to be carried out to devise a heating beam to have a larger lateral beam width that is wide enough to cover a sizable portion of the liver as the adipose distribution across the liver is heterogeneous.

4.3.7 Future applications

The use of multi-foci beamforming can be twofold, not only can it be used for heating the tissue but also to generate an acoustic radiation force push which is beneficial in determining the bio-mechanical properties of tissue using elastography methods such as acoustic radiation force impulse (ARFI) imaging. Currently, no such multimodal imaging tool exists. A successful implementation of this dual-modality imaging system will be a step towards a novel clinical system which would permit the creation of a single co-registered image featuring information regarding lipid content and stiffness of tissue.

4.4 Conclusion

In this paper, multi-foci beamforming implemented on a curved linear array transducer for abdominal imaging was reported. The multi-foci beam yielded an extended area of uniform heating from -7 to +7 mm in the lateral direction and 32 to 96 mm in the axial direction, evidenced in hydrophone measurements. The maximum temperature rise at the focal point measured 1.0°C within 2.0 seconds which is within the safety limits before any adverse biological effects develop. TSI pulse sequence utilizing multi-foci beamforming identified with high contrast rubber inclusion and liposuction fat embedded in tissue-mimicking gelatin phantoms. This work warrants further transitional investigation using excised human liver tissue diagnosed with fatty liver disease.

5.0 Multi-Foci Beamforming for Simultaneous Acoustic Radiation Force Impulse And Thermal Strain Imaging

5.1 Introduction

Currently, manual palpation is the preferred choice for a routine clinical exam to physically determine the health of tissue. For instance, during routine breast exams, manual palpation is valuable in identifying stiff lesions in the breast as an early sign of breast cancer. However, assessment from manual palpation is subjective and more inclined towards large and superficial structures [24, 98]. Recently, the demand for methods designed to access the biomechanical properties of tissues with improved sensitivity and specificity in comparison to manual palpation has increased. Ultrasound-based elasticity imaging methods has shown its potential in determining the stiffness of soft tissues deep within the human body. The elasticity of soft tissues has been correlated to the pathological conditions within tissue such that a hard tissue indicates the presence of a stiffer mass, inflammation and infection whereas a soft or compliant tissue is an indication of a healthy tissue [24, 98, 99].

Conventional ultrasound, B-mode imaging, utilizes acoustic impedance properties to differentiate among regions of tissues. In contrast, ultrasound-based elasticity imaging techniques utilize biomechanical properties to differentiate among regions of tissues. This is achieved by excitation of soft tissues and monitoring the response as a result of the excitation. This response can yield qualitative or quantitative information about the stiffness of the tissue [24, 98, 99]. The methods of excitation are numerous and can be introduced by applying an external force, for example an ultrasound transducer compressed against the skin surface in strain imaging [100-102].

Likewise, an external mechanical vibrator can be used to oscillate the tissue in sonoelasticity, transient elastography, magnetic resonance elastography (MRE) [103, 104]. Moreover, naturally occurring physiological based sources such as breathing, cardiac rhythms and arterial pulsations can be used to reveal elasticity information in cardiac strain-rate imaging [77, 105-108]. In our work, we will focus on elasticity imaging methods based upon acoustic radiation force (ARF).

ARF based elasticity methods applies acoustic radiation force as the source of mechanical excitation. Acoustic radiation force results from the transfer of momentum from the ultrasonic wave to the tissue due to the absorption and scattering mechanisms [109]. There are two elasticity imaging methods based upon ARF excitation, shear wave elasticity imaging (SWEI) and acoustic radiation force impulse imaging (ARFI) [109, 110].

ARF methods generate shear waves within tissue perpendicular to the direction of the ultrasound wave. SWEI methods monitor the propagating speed of the shear waves away from the region of excitation (ROE) to calculate the shear modulus. Shear modulus is given by the following equation, which is a measure of tissue elasticity.

$$\mu = \rho {c_s}^2 \qquad (5\text{-}1)$$

where μ is the shear modulus [Pa], ρ is density of soft tissue which is assumed to be 1000 kg/m^3 and c_s is the shear wave propagation [m/s]. Higher shear wave speed corresponds to stiffer tissues and slower shear wave speed corresponds to compliant tissues [110, 111].

ARFI monitors the response of the tissue in the direction of wave propagation i.e. within the radiation force ROE. The magnitude of the acoustic radiation force is calculated by the following equation:

$$F = \frac{2\alpha I}{c} \qquad (5\text{-}2)$$

where F [kg/(s^{2}cm$^{2)}$] is the magnitude of the radiation force, α [Np/m] is the acoustic absorption coefficient, I [W/cm^2] is the acoustic intensity of the beam and c [m/s] is the speed of sound. The magnitude of this force is typically on the order of dynes. This force is in the form of a body force [24, 109].

ARFI methods utilize short durations of high intensity focused ultrasound pulse to generate a push in a localized region of excitation. The response of the tissue inside the region of excitation is determined by estimating the displacement using correlation-based methods. ARFI creates tissue displacement in the range of 1 to 15 μm. The magnitude of the tissue displacement is inversely proportional to the tissue elastic shear modulus. Smaller displacements are related to stiffer tissues and larger displacements are related to compliant tissues [24, 109]. ARFI imaging is beneficial in revealing biomechanical information of tissues which is not possible with conventional B-mode imaging. ARFI imaging has been used in clinics for multiple applications. For example, ARFI imaging has been used to access the stiffness of both cardiac and vascular tissues during the cardiac cycle [112, 113] and it has been valuable in distinguishing the soft vulnerable atherosclerosis plaques from the stiffer and more stable ones [114, 115]. It has also been used in cancer imaging to identify the stiffer tumor lesions in the breast [116]. Furthermore, ARFI imaging is essential in determining the structural information such as the size of lesions present in prostrate and kidneys that are difficulty to visualize with conventional ultrasound B-mode [117].

In ARFI, a single transducer is used to generate the push and monitor the deformation response. At a given lateral position, a typical ARFI pulse sequence consists of 1) a reference pulse (A-line) which serves as a baseline position for the tissue before applying acoustic radiation force

2) followed by pushing pulses along the same reference A-line responsible for generating the acoustic radiation force to introduce motion in a localized region and 3) then a series of tracking pulses which are immediately applied after acoustic radiation force to record the deformation response and recovery of the soft tissue. This combination of reference pulse, pushing pulse and tracking pulse is replicated across the aperture in the lateral direction to drive biomechanical information [118].

The shape of the displacement field, generated by the high intensity focused acoustic pulses, is dependent upon the transducer focal configurations which is characterized by the dimensionless f-number, $(F/\#)$.

$$F/\# = \frac{z}{D} \qquad (5\text{-}3)$$

where z is the acoustic focal depth and D is the width of the active aperture. The active aperture width, D, is defined by the following equation:

$$D = N \,.\, d \qquad (5\text{-}4)$$

where N is the number of elements and d is the element pitch. Element pitch is the distance between the centers of two successive transducer elements.

For a given f-number of 1.3 at a focal depth of 25 mm, the first step involves computing the number of pushing lines. This step is similar to calculating the number of scan lines in beamforming in linear array transducer for focused imaging. Using the equation for f-number, the aperture width is calculated at 65.38 wavelengths. This is followed by calculating the number of transducer elements needed to generate the pushing line. The number of active elements required were 65 (= 65.38 / 1.00). The element pitch was 1.00 wavelengths.

A lower f-number indicates a greater number of active elements for pushing, therefore depositing higher amounts of energy and generating greater displacements at the expense of a smaller ROE. A trade off exists between the f-number and the number of active elements. Table 1 summarizes the results of the number of pushing lines and the number of active elements for different f-number configurations.

Table 5.1: The number of pushing lines and the number of active elements for different f-number configurations

F/#	No. of Lines	No. of Active Elements
1.0	44	85
1.3	64	65
1.5	72	57
1.7	78	51
2.0	86	43

The devised multi-foci beam can also be used to generate an acoustic radiation force push. This multi-foci push is localized to a specific region i.e. the region of excitation and it generates displacement in a smaller window as opposed to a conventional ARFI (parallel transmit and receive) where a large field of view (FOV) is displaced by the radiation force. The multi-foci beam can be simultaneously used for ARFI push and TSI heating. In ARFI imaging, the time it takes for the tissue to return back to its baseline position after the acoustic radiation force is over a period of 1 to 10 ms. Moreover, heating the tissue takes hundreds of milliseconds and declines in seconds. These differences in temporal responses for ARFI and TSI can be monitored simultaneously.

5.2 Materials and Methods

5.2.1 Excised Human Liver Tissue

Excised human liver tissue specimens were obtained from the Pitt Biospecimen Core (PBC) facility under an approved University of Pittsburgh IRB code (19030357). Two samples were surgically excised from two patients diagnosed with alcoholic liver diseases (ALD). The samples were kept frozen at -80°C. PBC also provided the pathology reports, approved by a physician, for each patient. The pathology report for the first specimen identified the patient as a 55 to 60-year-old male, diagnosed with alcoholic liver disease, cirrhosis and severe encephalopathy. A CT-scan of the abdomen was performed in 2010 to verify the cirrhosis in liver and the patient was recommended a liver transplant. The pathology report for the second specimen identified the patient as a 65 to 70-year-old male, diagnosed with alcoholic liver disease. A CT-scan of the abdomen in 2009 showed cirrhotic liver morphology with stigmata of portal hypertension and this patient was also recommended a liver transplant. A prolonged history of drinking heavily can lead to a severe and potentially fatal condition, eventually requiring a liver transplant. Figure 5.1 shows the excised human liver tissue specimens. The excised human liver tissues were defrosted and embedded in gelatin phantoms for *ex-vivo* measurements. A tissue mimicking gelatin phantom was fabricated.

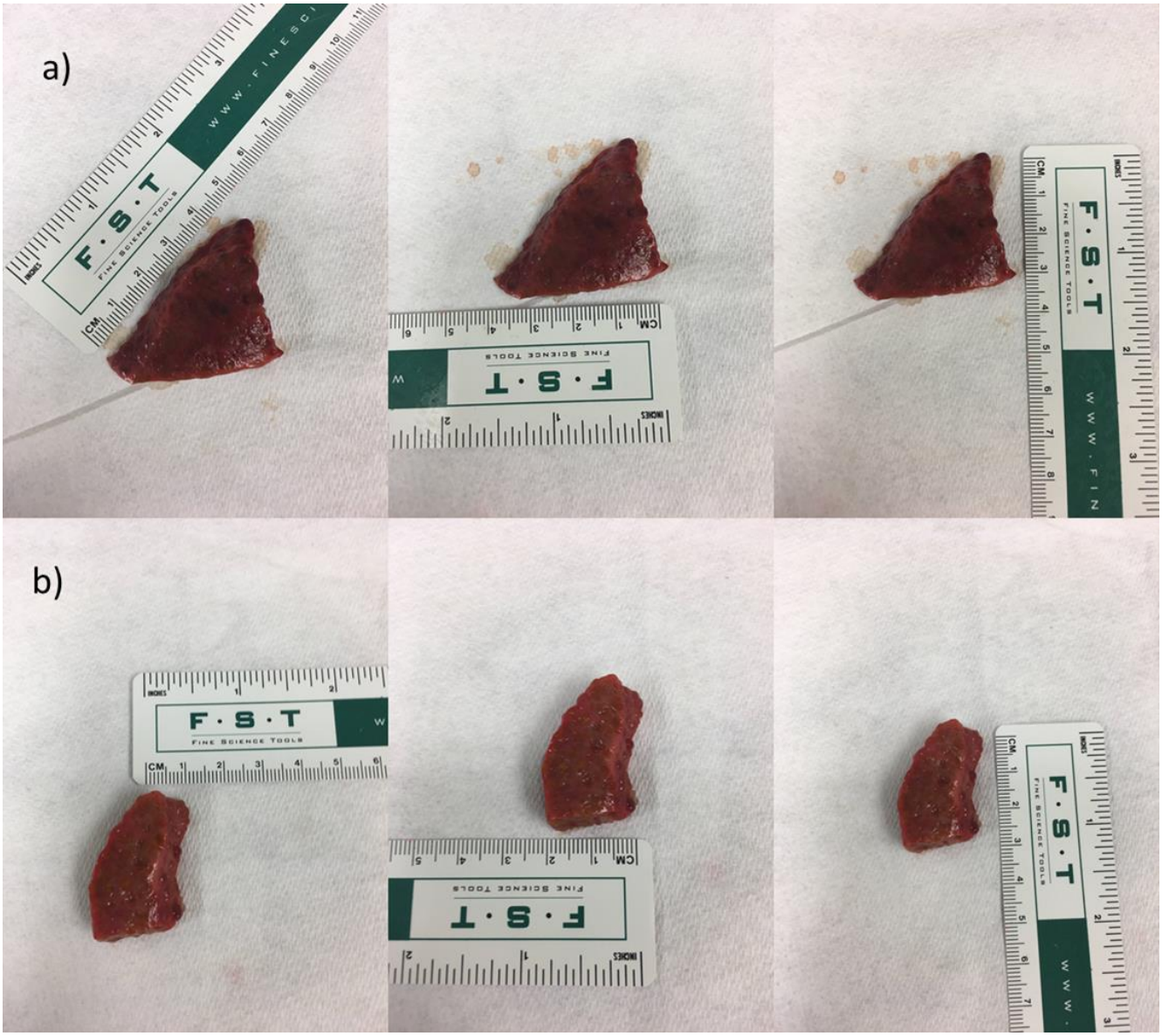

Figure 5.1: Excised human liver tissue specimens diagnosed with alcoholic liver disease

5.2.2 Phantom Construction

The homogeneous gelatin phantom was manufactured by gradually adding 50 g (5% g/mL) of porcine skin gelatin (Sigma Aldrich Co., MO, USA) to 1000 mL of cold water. The solution was allowed to mix homogeneously until it became transparent or reached an approximate temperature of 65°C. A further 10 g (1% g/mL) of cellulose (Sigma Aldrich Co., MO, USA) was added once the solution was clear. When the whole cellulose was completely dissolved, the mixture was poured into an empty container and kept inside the freezer at -20°C for about an hour to solidify. Any air bubbles on the surface have been carefully removed. The homogeneous gelatin phantom was then kept outside for a sufficient amount of time to reduce it to room temperature for ARFI and TSI measurements.

5.2.3 ARFI-TSI Imaging Pulse Sequence

The ARFI pulse sequence consists of acquiring pre-frames followed by a multi-foci push and then acquiring post-frames. Phase-shift method, Loupas, was used for tracking displacement in the axial direction. This algorithm utilizes the demodulated in-phase and quadrature data for tracking displacement as opposed to a cross-correlation method that operates in the time-domain on RF data. This segment of the ultrasound pulse sequence discloses information about the mechanical properties of the tissue. Tissue mimicking homogeneous gelatin phantom was manufactured to display the displacement map resulting from the radiation force.

For TSI pulse sequence, repeating this high intensity multi-foci beam for a longer duration (2.0 seconds) can lead to an increase in temperature via absorption by the propagating medium. Ultimately, post frames are collected at the end of this heating duration. These post-frames are

used to track displacement in the axial direction. Thermal strain is computed by taking the derivative in the axial direction. Thermal strain maps are color coded within the heating region such that red indicates a positive strain implying lipid presence and blue indicates a negative strain implying to water bearing tissue.

To measure the degree of steatosis in each of the excised human liver tissues by TSI, lipid composition [%] was defined as a metric. First, a region of interest (ROI) was determined i.e. the liver region insonified by the heating beam was identified from the US B-mode image. Then the number of pixels representing the positive thermal strain inside the liver ROI was determined. Lipid composition was calculated by dividing the pixels indicating the positive thermal strain over the liver ROI insonified by the heating beam. A threshold was predetermined for pixels which was counted towards the positive thermal strain. This threshold was computed by taking an average of the root mean square (RMS) values outside the heating region for each of the strain maps. The average RMS value calculated was 0.017%.

The stiffness of the liver insonified by the ARFI pushing beam was calculated by the mean ARFI displacement magnitude inside the ROI.

5.2.4 Tissue Thermal Response

In addition to generating the acoustic radiation force, acoustic energy is absorbed resulting in heat generated within the tissue. Temperature rise during ARFI imaging was measured using a Type T needle sheathed thermocouple (MT-23/5, Thermoworks, UT, USA) connected to a data acquisition module (QuadTemp, Thermoworks, Lindon, UT, USA). Temperature measurements

were recorded 3 times at an axial depth of 60 mm and 0 mm in the lateral direction. In the preceding chapter, temperature rise was measured for TSI pulse sequence.

5.2.5 Experimental Set-up

Ultrasound gel was used as a coupling medium between the transducer surface and the surface of the gelatin phantom. Commercially available ultrasound gel contains a lot of air bubbles. Ultrasound gel was centrifuged to remove the presence of any air bubbles. The transducer was clamped using an ultrasound probe holder. The ultrasound probe holder was mounted on a motorized linear translation stage (BiSlide MN10, Velmex, Bloomfield, NY, USA). The translation stage incorporates a stepper motor driven to sweep across the specimen during ultrasound scanning. 400 steps per revolution of the stepper motor corresponds to 1.0 mm of distance traversed.

For specimen 1, ultrasound scanning was performed on the longitudinal or long axis i.e. scanning was carried out in a plane parallel to the liver. A total of 5 slices were acquired. Each TSI slice was 1 mm apart. For specimen 2, ultrasound scanning was performed on the transverse or short axis i.e. scanning was carried out in a plane perpendicular to the liver. A total of 8 slices were acquired and each TSI slice was 3 mm apart.

5.2.6 Histology

After performing TSI, excised human liver tissue specimens underwent histopathological process to determine the amount of adipose tissue. Fresh frozen sections of the tissue, 10 – 50 μm in thickness, were cut and stained with oil red o (ORO). The oil red o stain is used to identify the

presence of fat in specimens of fatty liver disease. Under oil red o staining, the red dye indicates lipid presence and the blue dye indicates water bearing tissue. To quantify the degree of steatosis in each liver specimen, the area corresponding to the amount of lipid present in the specimen was calculated. This was done by dividing the area of red stain over the total area of the specimen. This image analysis was conducted using the ImageJ software (National Institutes of Health, Bethesda, MD). Livers with percentage steatosis ≥20% were considered fatty [48].

5.2.7 Statistical Analyses

A linear regression, Pearson's correlation coefficient (R^2), was used to determine the correlation between the lipid composition established by histology and TSI. Statistical analysis was carried out using the statistics toolbox of MATLAB R2020a.

5.3 Results and Discussion

5.3.1 Multi-foci ARFI Push

Figure 5.2 shows the results of testing the multi-foci ultrasound beam on a homogeneous gelatin phantom. Figure 5.2(a) shows a B-mode image of the gelatin phantom. Figure 5.2(b) displays an ARFI displacement map. The displacement is generated in an axial region corresponding to the depth of field plot from the Field II simulation, as indicated on the ARFI displacement map. Figure 5.2(c) shows a depth of field plot similar to the simulation result. Plane wave imaging (PWI) was used for tracking. PWI utilizes an unfocused transmit beam where all the transducer elements are fired simultaneously at the same time. PWI yields a higher frame rate compromising image resolution and contrast.

In an ARFI displacement map, darker regions represent a decrease displacement indicating the presence of a stiffer mass compared to the bright copper shade which represents higher displacement indicating the presence of a soft, malleable mass.

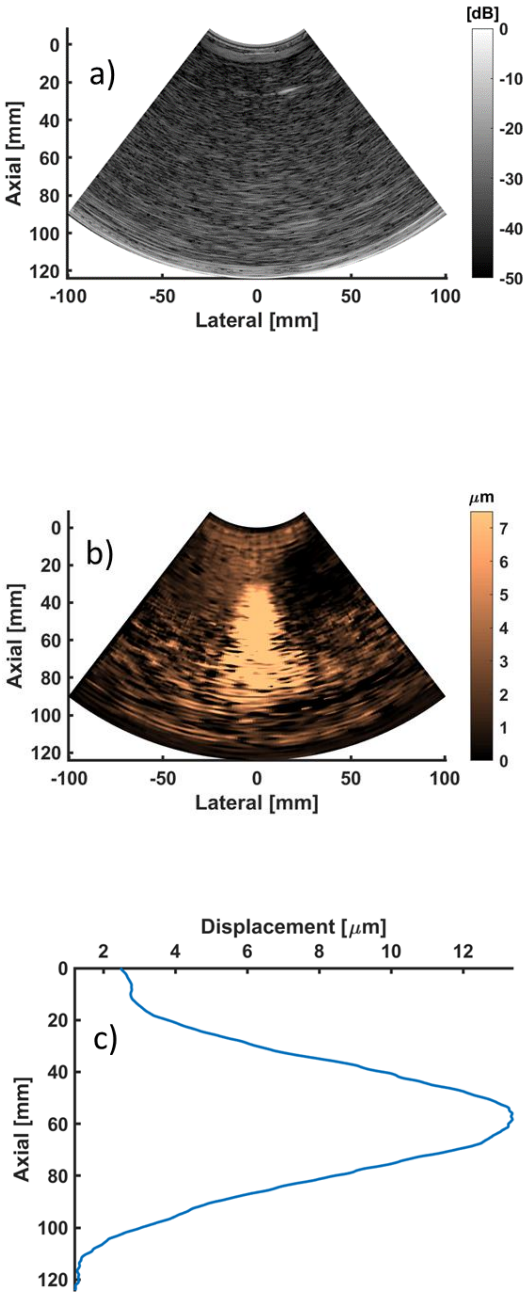

Figure 5.2: Multi-foci ARFI push was tested on a homogeneous gelatin phantom. (a) B-mode image of the gelatin phantom. Plane wave imaging was used instead of focused imaging to generate the b-mode image. (b) ARFI displacement map shown at the time of peak displacement. Displacement is registered in an axial window corresponding to the depth of field from Field II simulation. (c) the depth of field plot. The peak displacement occurs at 60 mm which correlates with results from simulation.

5.3.2 Temperature Measurement

Figure 5.3 displays the rise in temperature of the homogeneous gelatin phantom during the multi-foci ARFI pulse sequence. The temperature rise recorded during the multi-foci ARFI pushing pulse is barely perceptible. The maximum temperature rise at the focal point for ARFI imaging varies from 0.02°C to 0.2°C [98].

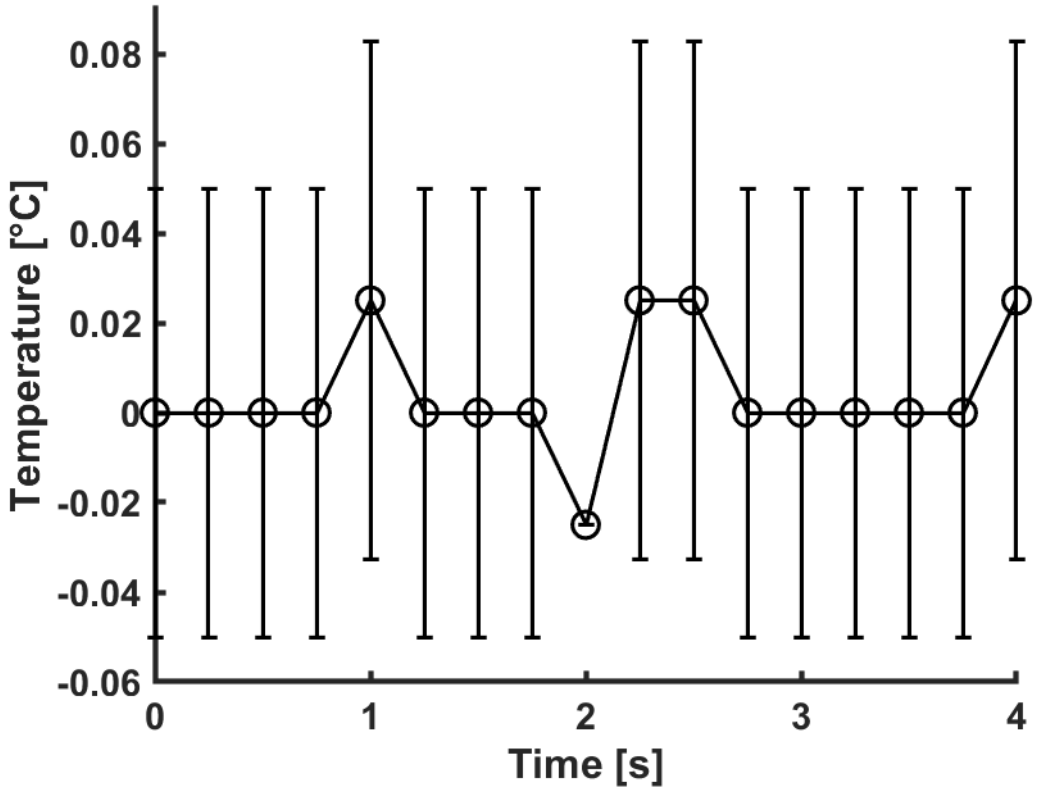

Figure 5.3: Temperature rise recorded during multi-foci ARFI pushing pulse

5.3.3 Excised Human Liver Tissue Results

To demonstrate that our technology can be used to diagnose real-life ailments, in particular nonalcoholic fatty liver disease, we tested the effectiveness of the combined ARFI-TSI pulse sequence on multiple gelatin phantom models with excised human liver tissue embedded inside. Figure 5.4(a) shows the B-mode image of the excised human liver tissue implanted in gelatin. The approximate region of heating is indicated by the dotted curved red line in Figure 5.4(a). The liver contour is marked by the dashed white line and the strain map is overlaid on the B-mode image in Figure 5.4(b). Figure 5.4(c) shows the corresponding oil red o histology. The black box on the strain map and histology indicates the heating area. Figure 5.4(d) reveals the corresponding displacement map overlaid on the B-mode. Histologically determined lipid composition and results from TSI have shown a strong correlation. The lipid composition determined by TSI for this slice of liver was 90.2% and 86.3% from histology. The mean displacement inside the ROI was 6.35 μm.

For specimens with larger dimensions, a routine procedure during histology is to cut the specimen into 2 pieces. The specimens are cut in a manner so that they can correctly overlay on top of the microscopic slide. Figure 5.4(c) shows the specimen cut into 2 sections.

Figure 5.5 shows the results of Pearson's correlation coefficient between lipid composition determined by histology and TSI for the 5 sections. A correlation of $R^2 = 0.67$ between the two measurements was observed.

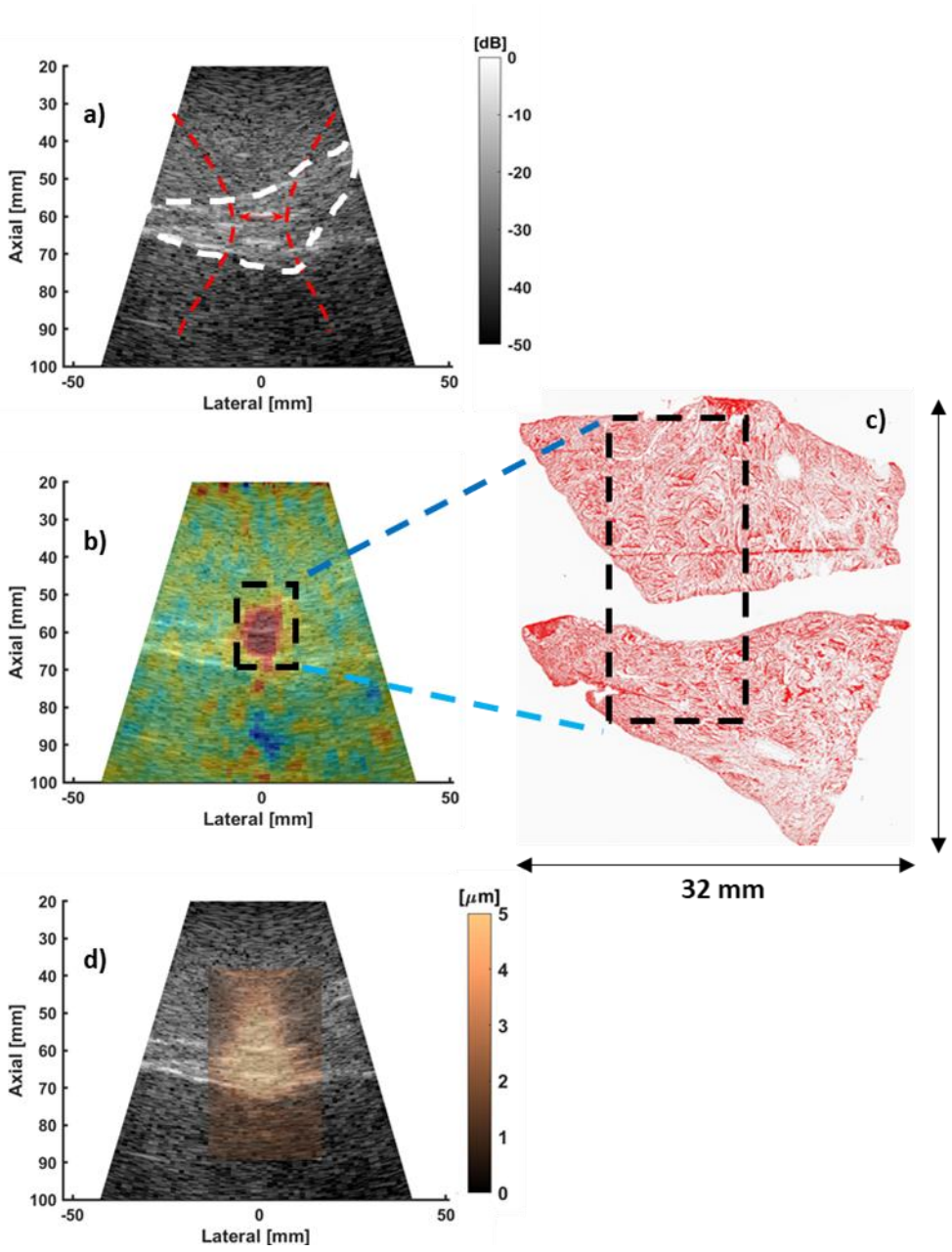

Figure 5.4: (a) B-mode image of the excised human liver tissue implanted in gelatin. (b) Strain map is overlaid on the b-mode image. (c) The corresponding oil red o histology. The black box on strain map and histology matches to the heating area. (d) corresponding displacement map overlaid on the B-mode.

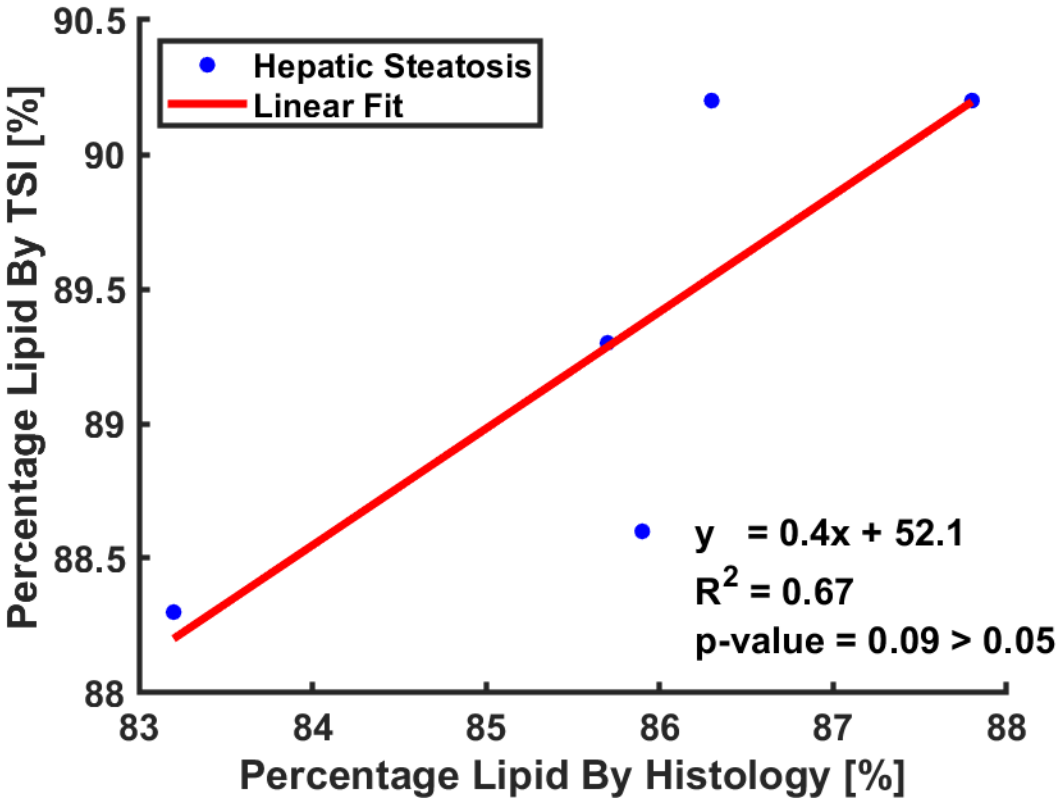

Figure 5.5: Pearson's correlation coefficient (R^2 = 0.67) between lipid composition determined by histology and TSI for the 5 sections.

The average displacement value reported within the ROE is more of a qualitative metric than a quantitative data. ARFI imaging does not disclose quantitative metric such as the speed of shear wave that can be used to measure the shear modulus. The mean displacement value reported by ARFI imaging may be less effective in revealing the biomechanical properties of soft tissue because of the limited field of view for multi-foci push. To resolve this challenge, ARFI measurements were also recorded in the adjacent regions i.e. on the homogeneous gelatin phantom. Figure 5.7 shows the mean ARFI displacement for liver and gelatin. The mean ARFI displacement inside the liver was 49% lower compared to the neighboring gelatin, indicating stiffer mechanical properties.

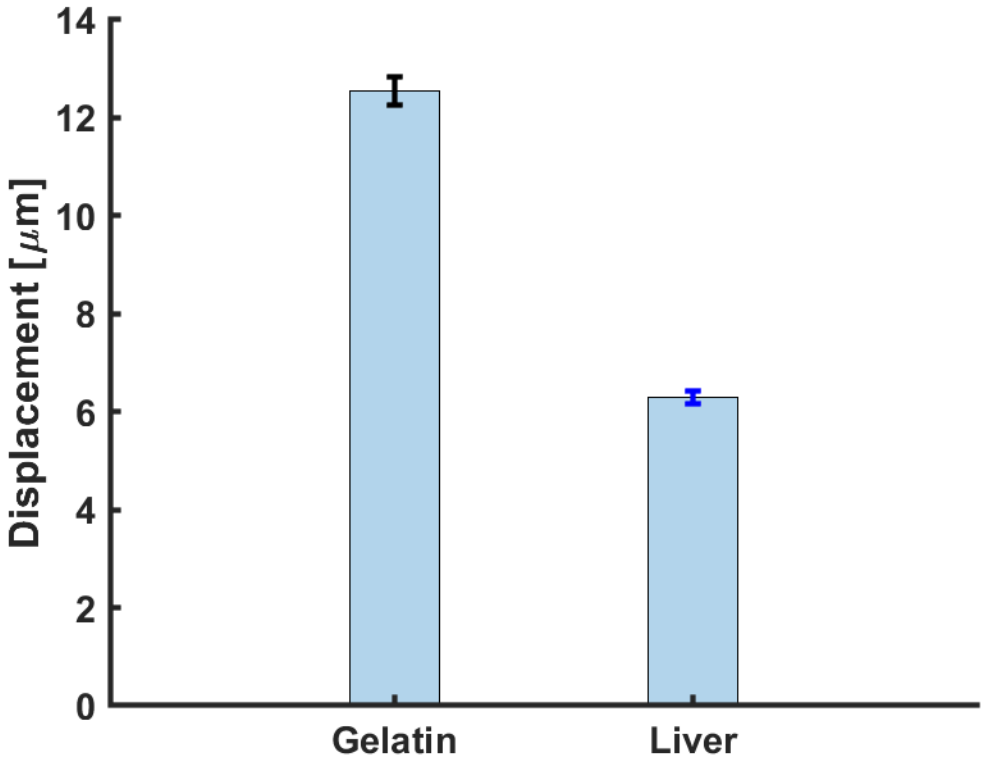

Figure 5.7: Mean ARFI displacement inside the liver and neighboring gelatin for the 5 sections.

One limitation of this study was the sample size of the liver tissues. An inadequate number of excised human liver tissue samples were used. Also, the contrast of results between the excised human liver tissue samples and a control group was unable to be demonstrated. Because of this, a complete statistical analysis was not carried out and quantitative measurements of the sensitivity and specificity of TSI were not performed preventing to generate a receiver operating characteristic (ROC) curve. Moreover, this study does not incorporate specimens that would reflect an entire spectrum of steatosis. These excised human liver tissue specimens were acquired from patients diagnosed with ALD with a history of alcohol abuse, exhibiting an excessive buildup of fat inside the liver cells. For future studies, it would be beneficial to have specimens that can be divided into

4 categories according to the severity of NAFLD: no NAFLD (≤5%), mild NAFLD (5% - 33%), moderate NAFLD (34% - 66%), and severe NAFLD (>66%) [119].

The average liver diameter for a healthy adult is roughly 14.0 cm [120]. The lateral beam width for TSI at 60 mm is 14 mm. The lesions arising from deposition of hepatic lipids are unevenly distributed throughout the liver parenchyma. The current design covers a very small fraction of the liver volume. This may give a rise to sampling error and staging inaccuracies. Further research for a design of multi-foci beamforming that can cover a substantial width of the liver is needed.

For clinical applications where visualization of structural information is of significance, for example in lesion identification and ablation procedure, a multi-foci beam with a large field of view can be advantageous. With the current design, ARFI imaging reveals qualitative information only within the ROE, thus neighboring regions next to ROE must be excited to showcase the contrast in displacement measurements. This will help to separate the rigid mass from the conforming masses. A possible area of investigation would be in cancer imaging, where ARFI can be used to differentiate malignant and benign lesions based on their displacement differences.

5.4 Conclusion

This dual modality imaging system provides a relatively uniform heating for TSI applications over an extended area. In addition, this system also generates an acoustic radiation force push which uncovers biomechanical properties of soft tissue. Lipid enriched excised human liver tissues were detected successfully in good agreement with histological findings. Furthermore, the mean displacement value calculated also suggested the presence of a stiffer mass. The ability to use this dual modality ARFI-TSI imaging system as a non-invasive screening test could spare the patients from medical complications and cost of a liver biopsy.

6.0 Conclusions and Future Work

6.1 Conclusions

The purpose of this work is to demonstrate a dual modality imaging system i.e. combining thermal strain imaging (TSI) and acoustic radiation force impulse (ARFI) imaging as a tool for measuring the amount of adipose tissue build up inside liver and assessing the bio-mechanical properties of liver. The results presented in this dissertation have demonstrated that TSI can be used to distinguish lipid bearing tissue from water bearing tissue. Moreover, further investigation indicated that multi-foci beamforming can be used to generate an acoustic radiation force in the direction of wave propagation.

Chapter 2 entails the utilization of a custom designed thermal strain imaging system for identification of lipids in obese mice. This custom engineered thermal strain imaging system had a separate transducer for heating and imaging. This setup required dedicated electronics and skilled expertise in setting up the equipment for scanning. Moreover, the center frequency for imaging (21 MHz) was impractical for scanning abdominal organs. These fundamental limitations of separate transducers lead to the discovery of multi-foci beamforming. Multi-foci beamforming involves dividing the transducer elements into three sub-aperture and four sub-aperture. Each sub-aperture has a unique axial and lateral focus. The beams from 3 and 4 foci are interleaved thus producing a broad homogeneous region that can be used both for heating and pushing.

6.2 Future Work

6.2.1 Size of Heating Area

The multi-foci beamforming approach presented in this work for a curved linear array transducer yields an extended area of uniform heating from -7 to +7 mm in the lateral direction and 32 to 96 mm in the axial direction. However, for in-vivo testing on patients diagnosed with fatty liver disease, additional research needs to be carried out to devise a heating beam with a larger lateral beam width that is wide enough to cover a sizable portion of the liver as the lipid distribution across the liver is heterogeneous. A possible alternative is to explore an ultrasound elasticity imaging method, comb push ultrasound shear elastography (CUSE), where a large field of view (FOV) is insonofied. In CUSE, the elements of a linear array transducer are divided into sub-groups and each sub-group is responsible for generating a focused ultrasound beam arranged in a comb pattern (comb-push) for shear wave propagation [121, 122]. The sub-group division specified in CUSE can be studied for the sub-aperture configuration for multi-foci beamforming.

6.2.2 Motion Artifact Correction

Motion correction will need to be addressed when TSI is introduced in clinics. The displacement signal recorded through TSI is typically on the order of microns. However, hand motion introduced by sonographer during scanning, respiratory motion of the patient, and cardiac motion all have greater orders of magnitude and will utterly corrupt the displacement signal. This will produce a signal with a poor signal-to-noise ratio (SNR). However, these issues can be addressed by the following. The patients can be requested to hold their breath for a few seconds

(<5 s) to prevent motion arising from breathing. To compensate for cardiac pulsations, B-mode frames acquired before and after heating can be synchronized with an ECG trigger. Alternatively, advance signal processing techniques using time series analysis can be used to reduce motion artifact in US-TSI [61]. Moreover, other speckle tracking algorithms can be explored such as Bayesian speckle tracking for estimating ultrasound displacement [62, 63]. In the recent years, there has been a surge of machine-learning algorithms in ultrasonics. Machine-learning algorithms that features speckle tracking can be used for displacement estimation [64, 65].

Currently, we have successfully programmed an ARFI-TSI pulse sequence for a curved linear array transducer and tested benchtop using tissue mimicking phantoms and performed *ex vivo* experiments on human liver samples, one step towards a clinical translation of this technology. The results from excised human liver tissue has been validated against histology. The impact of the project will be influential in the NAFLD management, being complemented with laboratory assays to provide 1) critical diagnostic and prognostic information, 2) cost effective monitoring of the disease and treatment response.

Bibliography

[1] A. Ghaemi, F. A. Taleban, A. Hekmatdoost, A. Rafiei, V. Hosseini, Z. Amiri, R. Homayounfar, and H. Fakheri, "How Much Weight Loss is Effective on Nonalcoholic Fatty Liver Disease?," *Hepatitis Monthly,* vol. 13, no. 12, pp. e15227-e15227, 2013.

[2] A. Lonardo, F. Nascimbeni, M. Maurantonio, A. Marrazzo, L. Rinaldi, and L. E. Adinolfi, "Nonalcoholic fatty liver disease: Evolving paradigms," *World J Gastroenterol,* vol. 23, no. 36, pp. 6571-6592, Sep 28, 2017.

[3] N. Bastati, D. Feier, A. Wibmer, S. Traussnigg, C. Balassy, D. Tamandl, H. Einspieler, F. Wrba, M. Trauner, C. Herold, and A. Ba-Ssalamah, "Noninvasive Differentiation of Simple Steatosis and Steatohepatitis by Using Gadoxetic Acid–enhanced MR Imaging in Patients with Nonalcoholic Fatty Liver Disease: A Proof-of-Concept Study," *Radiology,* vol. 271, no. 3, pp. 739-747, 2014/06/01, 2014.

[4] S. Leoni, F. Tovoli, L. Napoli, I. Serio, S. Ferri, and L. Bolondi, "Current guidelines for the management of non-alcoholic fatty liver disease: A systematic review with comparative analysis," *World J Gastroenterol,* vol. 24, no. 30, pp. 3361-3373, Aug 14, 2018.

[5] P. Paschos, and K. Paletas, "Non alcoholic fatty liver disease and metabolic syndrome," *Hippokratia,* vol. 13, no. 1, pp. 9-19, Jan, 2009.

[6] A. Ismaiel, and D. L. Dumitraşcu, "Cardiovascular Risk in Fatty Liver Disease: The Liver-Heart Axis-Literature Review," *Front Med (Lausanne),* vol. 6, pp. 202, 2019.

[7] L. Calzadilla Bertot, and L. A. Adams, "The Natural Course of Non-Alcoholic Fatty Liver Disease," *Int J Mol Sci,* vol. 17, no. 5, May 20, 2016.

[8] N. Alkhouri, and A. J. McCullough, "Noninvasive Diagnosis of NASH and Liver Fibrosis Within the Spectrum of NAFLD," *Gastroenterol Hepatol (N Y),* vol. 8, no. 10, pp. 661-8, Oct, 2012.

[9] M. E. Rinella, R. Loomba, S. H. Caldwell, K. Kowdley, M. Charlton, B. Tetri, and S. A. Harrison, "Controversies in the Diagnosis and Management of NAFLD and NASH," *Gastroenterol Hepatol (N Y),* vol. 10, no. 4, pp. 219-27, Apr, 2014.

[10] G. C. Farrell, D. van Rooyen, L. Gan, and S. Chitturi, "NASH is an Inflammatory Disorder: Pathogenic, Prognostic and Therapeutic Implications," *Gut Liver,* vol. 6, no. 2, pp. 149-71, Apr, 2012.

[11] S. Schuster, D. Cabrera, M. Arrese, and A. E. Feldstein, "Triggering and resolution of inflammation in NASH," *Nat Rev Gastroenterol Hepatol,* vol. 15, no. 6, pp. 349-364, Jun, 2018.

[12] H. Enomoto, Y. Bando, H. Nakamura, S. Nishiguchi, and M. Koga, "Liver fibrosis markers of nonalcoholic steatohepatitis," *World J Gastroenterol,* vol. 21, no. 24, pp. 7427-35, Jun 28, 2015.

[13] B. Li, C. Zhang, and Y. T. Zhan, "Nonalcoholic Fatty Liver Disease Cirrhosis: A Review of Its Epidemiology, Risk Factors, Clinical Presentation, Diagnosis, Management, and Prognosis," *Can J Gastroenterol Hepatol,* vol. 2018, pp. 2784537, 2018.

[14] I. L. Nalbantoglu, and E. M. Brunt, "Role of liver biopsy in nonalcoholic fatty liver disease," *World J Gastroenterol,* vol. 20, no. 27, pp. 9026-37, Jul 21, 2014.

[15] P. Bedossa, and K. Patel, "Biopsy and Noninvasive Methods to Assess Progression of Nonalcoholic Fatty Liver Disease," *Gastroenterology,* vol. 150, no. 8, pp. 1811-1822.e4, Jun, 2016.

[16] D. H. Lee, "Imaging evaluation of non-alcoholic fatty liver disease: focused on quantification," *Clin Mol Hepatol,* vol. 23, no. 4, pp. 290-301, Dec, 2017.

[17] Q. Li, M. Dhyani, J. R. Grajo, C. Sirlin, and A. E. Samir, "Current status of imaging in nonalcoholic fatty liver disease," *World J Hepatol,* vol. 10, no. 8, pp. 530-542, Aug 27, 2018.

[18] M. M. Wells, Z. Li, B. Addeman, C. A. McKenzie, A. Mujoomdar, M. Beaton, and J. Bird, "Computed Tomography Measurement of Hepatic Steatosis: Prevalence of Hepatic Steatosis in a Canadian Population," *Can J Gastroenterol Hepatol,* vol. 2016, pp. 4930987, 2016.

[19] C. Caussy, S. B. Reeder, C. B. Sirlin, and R. Loomba, “Noninvasive, Quantitative Assessment of Liver Fat by MRI-PDFF as an Endpoint in NASH Trials,” *Hepatology,* vol. 68, no. 2, pp. 763-772, Aug, 2018.

[20] A. R. Mahale, S. D. Prabhu, M. Nachiappan, M. Fernandes, and S. Ullal, “Clinical relevance of reporting fatty liver on ultrasound in asymptomatic patients during routine health checkups,” *J Int Med Res*, vol. 46, no. 11, pp. 4447-4454, Nov, 2018.

[21] J. C. Bamber, and C. R. Hill, “Ultrasonic attenuation and propagation speed in mammalian tissues as a function of temperature,” *Ultrasound Med Biol,* vol. 5, no. 2, pp. 149-57, 1979.

[22] J. C. Bamber, "Acoustical Characteristics of Biological Media," *Encyclopedia of Acoustics*, M. J. Crocker, ed., pp. 1703-1726, New York: John Wiley, 1997.

[23] F. A. Duck, *Physical properties of tissue : a comprehensive reference book*, London: Academic Press, 1990.

[24] K. Nightingale, “Acoustic Radiation Force Impulse (ARFI) Imaging: a Review,” *Curr Med Imaging Rev,* vol. 7, no. 4, pp. 328-339, Nov 1, 2011.

[25] P. Angulo, and K. D. Lindor, “Non-alcoholic fatty liver disease,” *Journal of Gastroenterology and Hepatology,* vol. 17, no. s1, pp. S186-S190, 2002/02/01, 2002.

[26] S. M. Abd El-Kader, and E. M. El-Den Ashmawy, “Non-alcoholic fatty liver disease: The diagnosis and management,” *World J Hepatol,* vol. 7, no. 6, pp. 846-58, Apr 28, 2015.

[27] R. Pais, A. S. t. Barritt, Y. Calmus, O. Scatton, T. Runge, P. Lebray, T. Poynard, V. Ratziu, and F. Conti, “NAFLD and liver transplantation: Current burden and expected challenges,” *J Hepatol,* vol. 65, no. 6, pp. 1245-1257, Dec, 2016.

[28] C. S. Hsu, and J. H. Kao, “Non-alcoholic fatty liver disease: an emerging liver disease in Taiwan,” *J Formos Med Assoc,* vol. 111, no. 10, pp. 527-35, Oct, 2012.

[29] N. Chalasani, Z. Younossi, J. E. Lavine, A. M. Diehl, E. M. Brunt, K. Cusi, M. Charlton, and A. J. Sanyal, “The diagnosis and management of non-alcoholic fatty liver disease: Practice Guideline by the American Association for the Study of Liver Diseases, American College of Gastroenterology,

and the American Gastroenterological Association," *Hepatology,* vol. 55, no. 6, pp. 2005-2023, 2012.

[30] Y. Sumida, A. Nakajima, and Y. Itoh, "Limitations of liver biopsy and non-invasive diagnostic tests for the diagnosis of nonalcoholic fatty liver disease/nonalcoholic steatohepatitis," *World journal of gastroenterology,* vol. 20, no. 2, pp. 475-485, 2014.

[31] J. L. Temple, P. Cordero, J. Li, V. Nguyen, and J. A. Oben, "A Guide to Non-Alcoholic Fatty Liver Disease in Childhood and Adolescence," *International journal of molecular sciences,* vol. 17, no. 6, pp. 947, 2016.

[32] Q. Li, M. Dhyani, J. R. Grajo, C. Sirlin, and A. E. Samir, "Current status of imaging in nonalcoholic fatty liver disease," *World journal of hepatology,* vol. 10, no. 8, pp. 530-542, 2018.

[33] J. K. Dyson, Q. M. Anstee, and S. McPherson, "Non-alcoholic fatty liver disease: a practical approach to diagnosis and staging," *Frontline gastroenterology,* vol. 5, no. 3, pp. 211-218, 2014.

[34] A. E. Bohte, J. R. van Werven, S. Bipat, and J. Stoker, "The diagnostic accuracy of US, CT, MRI and 1H-MRS for the evaluation of hepatic steatosis compared with liver biopsy: a meta-analysis," *Eur Radiol,* vol. 21, no. 1, pp. 87-97, Jan, 2011.

[35] S. B. Reeder, and C. B. Sirlin, "Quantification of liver fat with magnetic resonance imaging," *Magnetic resonance imaging clinics of North America,* vol. 18, no. 3, pp. 337-57, 2010.

[36] T.-H. Kim, C.-W. Jeong, H. Y. Jun, C. Lee, S. Noh, J. E. Kim, S. Kim, and K.-H. Yoon, "Accuracy of proton magnetic resonance for diagnosing non-alcoholic steatohepatitis: a meta-analysis," *Scientific Reports,* vol. 9, no. 1, pp. 15002, 2019/10/18, 2019.

[37] S. Sammet, "Magnetic resonance safety," *Abdom Radiol (NY),* vol. 41, no. 3, pp. 444-51, Mar, 2016.

[38] A. Benjamin, R. Zubajlo, K. Thomenius, M. Dhyani, K. Kaliannan, A. E. Samir, and B. W. Anthony, "Non-invasive diagnosis of non-alcoholic fatty liver disease (NAFLD) using ultrasound image echogenicity," *Conf Proc IEEE Eng Med Biol Soc,* vol. 2017, pp. 2920-2923, Jul, 2017.

[39] D. Joy, V. R. Thava, and B. B. Scott, "Diagnosis of fatty liver disease: is biopsy necessary?," *Eur J Gastroenterol Hepatol,* vol. 15, no. 5, pp. 539-43, May, 2003.

[40] R. Hernaez, M. Lazo, S. Bonekamp, I. Kamel, F. L. Brancati, E. Guallar, and J. M. Clark, "Diagnostic accuracy and reliability of ultrasonography for the detection of fatty liver: a meta-analysis," *Hepatology,* vol. 54, no. 3, pp. 1082-1090, Sep 2, 2011.

[41] S. Strauss, E. Gavish, P. Gottlieb, and L. Katsnelson, "Interobserver and intraobserver variability in the sonographic assessment of fatty liver," *AJR Am J Roentgenol,* vol. 189, no. 6, pp. W320-3, Dec, 2007.

[42] M. Obika, and H. Noguchi, "Diagnosis and evaluation of nonalcoholic fatty liver disease," *Exp Diabetes Res,* vol. 2012, pp. 145754, 2012.

[43] C. Simon, P. VanBaren, and E. S. Ebbini, "Two-dimensional temperature estimation using diagnostic ultrasound," *IEEE Transactions on Ultrasonics, Ferroelectrics, and Frequency Control,* vol. 45, no. 4, pp. 1088-1099, 1998.

[44] Y. Shi, R. S. Witte, and M. O'Donnell, "Identification of vulnerable atherosclerotic plaque using IVUS-based thermal strain imaging," *IEEE Transactions on Ultrasonics, Ferroelectrics, and Frequency Control,* vol. 52, no. 5, pp. 844-50, May, 2005.

[45] K. Kim, S. Huang, T. L. Hall, R. S. Witte, T. L. Chenevert, and M. O. Donnell, "Arterial Vulnerable Plaque Characterization Using Ultrasound-Induced Thermal Strain Imaging (TSI)," *IEEE Transactions on Biomedical Engineering,* vol. 55, no. 1, pp. 171-180, 2008.

[46] A. M. Mahmoud, D. Dutta, L. Lavery, D. N. Stephens, F. S. Villanueva, and K. Kim, "Noninvasive detection of lipids in atherosclerotic plaque using ultrasound thermal strain imaging: in vivo animal study," *J Am Coll Cardiol,* vol. 62, no. 19, pp. 1804-9, Nov 5, 2013.

[47] R. Maass-Moreno, and C. A. Damianou, "Noninvasive temperature estimation in tissue via ultrasound echo-shifts. Part I. Analytical model," *J Acoust Soc Am,* vol. 100, no. 4 Pt 1, pp. 2514-21, Oct, 1996.

[48] A. M. Mahmoud, X. Ding, D. Dutta, V. P. Singh, and K. Kim, "Detecting hepatic steatosis using ultrasound-induced thermal strain imaging: an ex vivo animal study," *Phys Med Biol,* vol. 59, no. 4, pp. 881-95, Feb 21, 2014.

[49] E. L. Thomas, G. Hamilton, N. Patel, R. O'Dwyer, C. J. Doré, R. D. Goldin, J. D. Bell, and S. D. Taylor-Robinson, "Hepatic triglyceride content and its relation to body adiposity: a magnetic resonance imaging and proton magnetic resonance spectroscopy study," *Gut,* vol. 54, no. 1, pp. 122-7, Jan, 2005.

[50] H. H. Hansen, M. Feigh, S. S. Veidal, K. T. Rigbolt, N. Vrang, and K. Fosgerau, "Mouse models of nonalcoholic steatohepatitis in preclinical drug development," *Drug Discov Today,* vol. 22, no. 11, pp. 1707-1718, Nov, 2017.

[51] A. W. Norris, L. Chen, S. J. Fisher, I. Szanto, M. Ristow, A. C. Jozsi, M. F. Hirshman, E. D. Rosen, L. J. Goodyear, F. J. Gonzalez, B. M. Spiegelman, and C. R. Kahn, "Muscle-specific PPARgamma-deficient mice develop increased adiposity and insulin resistance but respond to thiazolidinediones," *J Clin Invest,* vol. 112, no. 4, pp. 608-18, Aug, 2003.

[52] D. N. Stephens, A. M. Mahmoud, X. Ding, S. Lucero, D. Dutta, F. T. H. Yu, X. Chen, and K. Kim, "Flexible integration of high-imaging-resolution and high-power arrays for ultrasound-induced thermal strain imaging (US-TSI)," *IEEE transactions on Ultrasonics, Ferroelectrics, and Frequency Control,* vol. 60, no. 12, pp. 2645-2656, 2013.

[53] G. F. Pinton, J. J. Dahl, and G. E. Trahey, "Rapid tracking of small displacements with ultrasound," *IEEE transactions on Ultrasonics, Ferroelectrics, and Frequency Control,* vol. 53, no. 6, pp. 1103-17, Jun, 2006.

[54] M. Benedict, and X. Zhang, "Non-alcoholic fatty liver disease: An expanded review," *World J Hepatol,* vol. 9, no. 16, pp. 715-732, Jun 8, 2017.

[55] E. M. Brunt, D. E. Kleiner, L. A. Wilson, P. Belt, B. A. Neuschwander-Tetri, and N. C. R. Network, "Nonalcoholic fatty liver disease (NAFLD) activity score and the histopathologic diagnosis in

NAFLD: distinct clinicopathologic meanings," *Hepatology (Baltimore, Md.),* vol. 53, no. 3, pp. 810-820, 2011.

[56] Y. Kamada, S. Kiso, Y. Yoshida, N. Chatani, T. Kizu, M. Hamano, M. Tsubakio, T. Takemura, H. Ezaki, N. Hayashi, and T. Takehara, "Estrogen deficiency worsens steatohepatitis in mice fed high-fat and high-cholesterol diet," *Am J Physiol Gastrointest Liver Physiol,* vol. 301, no. 6, pp. G1031-43, Dec, 2011.

[57] J. Ludwig, T. R. Viggiano, D. B. McGill, and B. J. Oh, "Nonalcoholic steatohepatitis: Mayo Clinic experiences with a hitherto unnamed disease," *Mayo Clin Proc,* vol. 55, no. 7, pp. 434-8, Jul, 1980.

[58] V. H. I. Fengler, T. Macheiner, S. M. Kessler, B. Czepukojc, K. Gemperlein, R. Müller, A. K. Kiemer, C. Magnes, J. Haybaeck, C. Lackner, and K. Sargsyan, "Susceptibility of Different Mouse Wild Type Strains to Develop Diet-Induced NAFLD/AFLD-Associated Liver Disease," *PLOS ONE,* vol. 11, no. 5, pp. e0155163, 2016.

[59] M. M. Nguyen, X. Ding, F. Yu, and K. Kim, "Adaptive beamforming for thermal strain imaging using a single ultrasound linear array." pp. 1686-1689.

[60] M. M. Nguyen, X. Ding, S. A. Leers, and K. Kim, "Multi-Focus Beamforming for Thermal Strain Imaging Using a Single Ultrasound Linear Array Transducer," *Ultrasound Med Biol,* vol. 43, no. 6, pp. 1263-1274, Jun, 2017.

[61] D. Dutta, A. M. Mahmoud, S. A. Leers, and K. Kim, "Motion Artifact Reduction in Ultrasound Based Thermal Strain Imaging of Atherosclerotic Plaques Using Time Series Analysis," *IEEE transactions on Ultrasonics, Ferroelectrics, and Frequency Control,* vol. 60, no. 8, pp. 1660-1668, Aug 2, 2013.

[62] B. Byram, G. E. Trahey, and M. Palmeri, "Bayesian speckle tracking. Part I: an implementable perturbation to the likelihood function for ultrasound displacement estimation," *IEEE Trans Ultrason Ferroelectr Freq Control,* vol. 60, no. 1, pp. 132-43, Jan, 2013.

[63] B. Byram, G. E. Trahey, and M. Palmeri, “Bayesian speckle tracking. Part II: biased ultrasound displacement estimation,” *IEEE Trans Ultrason Ferroelectr Freq Control,* vol. 60, no. 1, pp. 144-57, Jan, 2013.

[64] P. P. Sengupta, Y. M. Huang, M. Bansal, A. Ashrafi, M. Fisher, K. Shameer, W. Gall, and J. T. Dudley, “Cognitive Machine-Learning Algorithm for Cardiac Imaging: A Pilot Study for Differentiating Constrictive Pericarditis From Restrictive Cardiomyopathy,” *Circ Cardiovasc Imaging,* vol. 9, no. 6, Jun, 2016.

[65] S. Narula, K. Shameer, A. M. Salem Omar, J. T. Dudley, and P. P. Sengupta, “Machine-Learning Algorithms to Automate Morphological and Functional Assessments in 2D Echocardiography,” *Journal of the American College of Cardiology,* vol. 68, no. 21, pp. 2287-2295, 2016/11/29/, 2016.

[66] F. Forsberg, W. T. Shi, C. R. Merritt, Q. Dai, M. Solcova, and B. B. Goldberg, “On the usefulness of the mechanical index displayed on clinical ultrasound scanners for predicting contrast microbubble destruction,” *J Ultrasound Med,* vol. 24, no. 4, pp. 443-50, Apr, 2005.

[67] G. Ter Haar, “Ultrasonic imaging: safety considerations,” *Interface focus,* vol. 1, no. 4, pp. 686-697, 2011.

[68] T. L. Szabo, "Chapter 1 - Introduction," *Diagnostic Ultrasound Imaging: Inside Out (Second Edition)*, T. L. Szabo, ed., pp. 1-37, Boston: Academic Press, 2014.

[69] W. Lee, and Y. Roh, “Ultrasonic transducers for medical diagnostic imaging,” *Biomed Eng Lett,* vol. 7, no. 2, pp. 91-97, May, 2017.

[70] T. P. Nguyen, N. T. P. Truong, N. Q. Bui, V. T. Nguyen, G. Hoang, J. Choi, T. T. V. Phan, V. H. Pham, B. G. Kim, and J. Oh, “Design, Fabrication, and Evaluation of Multifocal Point Transducer for High-Frequency Ultrasound Applications,” *Sensors (Basel),* vol. 19, no. 3, Feb 1, 2019.

[71] G. Matrone, A. S. Savoia, G. Caliano, and G. Magenes, “The Delay Multiply and Sum Beamforming Algorithm in Ultrasound B-Mode Medical Imaging,” *IEEE Transactions on Medical Imaging,* vol. 34, no. 4, pp. 940-949, 2015.

[72] R. S. C. Cobbold, *Foundations of Biomedical Ultrasound*, New York: Oxford University Press, 2007.

[73] J. A. Jensen, and N. B. Svendsen, "Calculation of pressure fields from arbitrarily shaped, apodized, and excited ultrasound transducers," *IEEE Transactions on Ultrasonics, Ferroelectrics, and Frequency Control,* vol. 39, no. 2, pp. 262-267, 1992.

[74] B. J. Perumpail, M. A. Khan, E. R. Yoo, G. Cholankeril, D. Kim, and A. Ahmed, "Clinical epidemiology and disease burden of nonalcoholic fatty liver disease," *World J Gastroenterol,* vol. 23, no. 47, pp. 8263-8276, Dec 21, 2017.

[75] S. B. Reeder, and C. B. Sirlin, "Quantification of liver fat with magnetic resonance imaging," *Magnetic resonance imaging clinics of North America,* vol. 18, no. 3, pp. 337-ix, 2010.

[76] S. Waxman, F. Ishibashi, and J. E. Muller, "Detection and treatment of vulnerable plaques and vulnerable patients: novel approaches to prevention of coronary events," *Circulation,* vol. 114, no. 22, pp. 2390-411, Nov 28, 2006.

[77] C. L. de Korte, and A. F. van der Steen, "Intravascular ultrasound elastography: an overview," *Ultrasonics,* vol. 40, no. 1-8, pp. 859-65, May, 2002.

[78] P. A. Calvert, D. R. Obaid, M. O'Sullivan, L. M. Shapiro, D. McNab, C. G. Densem, P. M. Schofield, D. Braganza, S. C. Clarke, K. K. Ray, N. E. West, and M. R. Bennett, "Association between IVUS findings and adverse outcomes in patients with coronary artery disease: the VIVA (VH-IVUS in Vulnerable Atherosclerosis) Study," *JACC Cardiovasc Imaging,* vol. 4, no. 8, pp. 894-901, Aug, 2011.

[79] S. E. Nissen, "IVUS Virtual Histology: Unvalidated Gimmick or Useful Technique?," *J Am Coll Cardiol,* vol. 67, no. 15, pp. 1784-1785, Apr 19, 2016.

[80] I. K. Jang, B. E. Bouma, D. H. Kang, S. J. Park, S. W. Park, K. B. Seung, K. B. Choi, M. Shishkov, K. Schlendorf, E. Pomerantsev, S. L. Houser, H. T. Aretz, and G. J. Tearney, "Visualization of coronary atherosclerotic plaques in patients using optical coherence tomography: comparison with intravascular ultrasound," *J Am Coll Cardiol,* vol. 39, no. 4, pp. 604-9, Feb 20, 2002.

[81] A. S. Kini, S. Motoyama, Y. Vengrenyuk, J. E. Feig, J. Pena, U. Baber, A. M. Bhat, P. Moreno, J. C. Kovacic, J. Narula, and S. K. Sharma, "Multimodality Intravascular Imaging to Predict Periprocedural Myocardial Infarction During Percutaneous Coronary Intervention," *JACC Cardiovasc Interv,* vol. 8, no. 7, pp. 937-45, Jun, 2015.

[82] W. Choi, E.-Y. Park, S. Jeon, and C. Kim, "Clinical photoacoustic imaging platforms," *Biomedical Engineering Letters,* vol. 8, no. 2, pp. 139-155, 2018/05/01, 2018.

[83] A. B. Karpiouk, B. Wang, J. Amirian, R. W. Smalling, and S. Y. Emelianov, "Feasibility of in vivo intravascular photoacoustic imaging using integrated ultrasound and photoacoustic imaging catheter," *J Biomed Opt,* vol. 17, no. 9, pp. 96008-1, Sep, 2012.

[84] J. Hui, Y. Cao, Y. Zhang, A. Kole, P. Wang, G. Yu, G. Eakins, M. Sturek, W. Chen, and J. X. Cheng, "Real-time intravascular photoacoustic-ultrasound imaging of lipid-laden plaque in human coronary artery at 16 frames per second," *Sci Rep,* vol. 7, no. 1, pp. 1417, May 3, 2017.

[85] Y. Cao, J. Hui, A. Kole, P. Wang, Q. Yu, W. Chen, M. Sturek, and J. X. Cheng, "High-sensitivity intravascular photoacoustic imaging of lipid-laden plaque with a collinear catheter design," *Sci Rep,* vol. 6, pp. 25236, Apr 28, 2016.

[86] J. Hui, Q. Yu, T. Ma, P. Wang, Y. Cao, R. S. Bruning, Y. Qu, Z. Chen, Q. Zhou, M. Sturek, J. X. Cheng, and W. Chen, "High-speed intravascular photoacoustic imaging at 1.7 μm with a KTP-based OPO," *Biomed Opt Express,* vol. 6, no. 11, pp. 4557-66, Nov 1, 2015.

[87] P. Wang, T. Ma, M. N. Slipchenko, S. Liang, J. Hui, K. K. Shung, S. Roy, M. Sturek, Q. Zhou, Z. Chen, and J. X. Cheng, "High-speed intravascular photoacoustic imaging of lipid-laden atherosclerotic plaque enabled by a 2-kHz barium nitrite raman laser," *Sci Rep,* vol. 4, pp. 6889, Nov 4, 2014.

[88] C. Choi, J. Ahn, and C. Kim, "Intravascular Photothermal Strain Imaging for Lipid Detection," *Sensors (Basel),* vol. 18, no. 11, Oct 24, 2018.

[89] C. Y. Lai, D. E. Kruse, C. F. Caskey, D. N. Stephens, P. L. Sutcliffe, and K. W. Ferrara, "Noninvasive thermometry assisted by a dual-function ultrasound transducer for mild

hyperthermia," *IEEE Trans Ultrason Ferroelectr Freq Control,* vol. 57, no. 12, pp. 2671-84, Dec, 2010.

[90] R. Martinez-Valdez, A. Vera, and L. Leija, "HIFU Induced Heating Modelling by Using the Finite Element Method," *Physics Procedia,* vol. 63, 12/31, 2015.

[91] S. W. Huang, K. Kim, R. S. Witte, R. Olafsson, and M. O'Donnell, "Inducing and imaging thermal strain using a single ultrasound linear array," *IEEE Trans Ultrason Ferroelectr Freq Control,* vol. 54, no. 9, pp. 1718-20, Sep, 2007.

[92] K. A. Wear, Y. Liu, and G. R. Harris, "Pressure Pulse Distortion by Needle and Fiber-Optic Hydrophones due to Nonuniform Sensitivity," *IEEE Trans Ultrason Ferroelectr Freq Control,* vol. 65, no. 2, pp. 137-148, Feb, 2018.

[93] D. C. Wolf, "Evaluation of the Size, Shape, and Consistency of the Liver," *Clinical Methods: The History, Physical, and Laboratory Examinations,* H. K. Walker, W. D. Hall and J. W. Hurst, eds., Boston: Butterworths, 1990.

[94] A. Coccarelli, E. Boileau, D. Parthimos, and P. Nithiarasu, "An advanced computational bioheat transfer model for a human body with an embedded systemic circulation," *Biomech Model Mechanobiol,* vol. 15, no. 5, pp. 1173-90, Oct, 2016.

[95] D. B. Rodrigues, P. J. Pereira, P. Limão-Vieira, P. R. Stauffer, and P. F. Maccarini, "Study of the one dimensional and transient bioheat transfer equation: multi-layer solution development and applications," *Int J Heat Mass Transf,* vol. 62, pp. 153-162, Jul 1, 2013.

[96] S. Datta, C. C. Coussios, L. E. McAdory, J. Tan, T. Porter, G. De Courten-Myers, and C. K. Holland, "Correlation of cavitation with ultrasound enhancement of thrombolysis," *Ultrasound Med Biol,* vol. 32, no. 8, pp. 1257-67, Aug, 2006.

[97] A. D. Maxwell, C. A. Cain, T. L. Hall, J. B. Fowlkes, and Z. Xu, "Probability of cavitation for single ultrasound pulses applied to tissues and tissue-mimicking materials," *Ultrasound Med Biol,* vol. 39, no. 3, pp. 449-65, Mar, 2013.

[98] J. R. Doherty, G. E. Trahey, K. R. Nightingale, and M. L. Palmeri, “Acoustic radiation force elasticity imaging in diagnostic ultrasound,” *IEEE Trans Ultrason Ferroelectr Freq Control,* vol. 60, no. 4, pp. 685-701, Apr, 2013.

[99] X. Qian, T. Ma, M. Yu, X. Chen, K. K. Shung, and Q. Zhou, “Multi-functional Ultrasonic Micro-elastography Imaging System,” *Scientific Reports,* vol. 7, no. 1, pp. 1230, 2017/04/27, 2017.

[100] J. Ophir, I. Céspedes, H. Ponnekanti, Y. Yazdi, and X. Li, “Elastography: a quantitative method for imaging the elasticity of biological tissues,” *Ultrason Imaging,* vol. 13, no. 2, pp. 111-34, Apr, 1991.

[101] O. Jonathan, S. Seshadri, R. Raffaella, and T. Arun, “Elastography: A Decade of Progress (2000-2010),” *Current Medical Imaging,* vol. 7, no. 4, pp. 292-312, 2011.

[102] C. F. Dietrich, R. G. Barr, A. Farrokh, M. Dighe, M. Hocke, C. Jenssen, Y. Dong, A. Saftoiu, and R. F. Havre, “Strain Elastography - How To Do It?,” *Ultrasound Int Open,* vol. 3, no. 4, pp. E137-e149, Sep, 2017.

[103] R. M. Lerner, S. R. Huang, and K. J. Parker, “"Sonoelasticity" images derived from ultrasound signals in mechanically vibrated tissues,” *Ultrasound Med Biol,* vol. 16, no. 3, pp. 231-9, 1990.

[104] J. P. Kevin, “The Evolution of Vibration Sonoelastography,” *Current Medical Imaging,* vol. 7, no. 4, pp. 283-291, 2011.

[105] R. J. Dickinson, and C. R. Hill, “Measurement of soft tissue motion using correlation between A-scans,” *Ultrasound Med Biol,* vol. 8, no. 3, pp. 263-71, 1982.

[106] J. J. Mai, and M. F. Insana, “Strain imaging of internal deformation,” *Ultrasound Med Biol,* vol. 28, no. 11-12, pp. 1475-84, Nov-Dec, 2002.

[107] J. D'Hooge, B. Bijnens, J. Thoen, F. Van de Werf, G. R. Sutherland, and P. Suetens, “Echocardiographic strain and strain-rate imaging: a new tool to study regional myocardial function,” *IEEE Trans Med Imaging,* vol. 21, no. 9, pp. 1022-30, Sep, 2002.

[108] L. S. Wilson, and D. E. Robinson, “Ultrasonic measurement of small displacements and deformations of tissue,” *Ultrason Imaging,* vol. 4, no. 1, pp. 71-82, Jan, 1982.

[109] K. Nightingale, M. S. Soo, R. Nightingale, and G. Trahey, “Acoustic radiation force impulse imaging: in vivo demonstration of clinical feasibility,” *Ultrasound Med Biol,* vol. 28, no. 2, pp. 227-35, Feb, 2002.

[110] A. P. Sarvazyan, O. V. Rudenko, S. D. Swanson, J. B. Fowlkes, and S. Y. Emelianov, “Shear wave elasticity imaging: a new ultrasonic technology of medical diagnostics,” *Ultrasound Med Biol,* vol. 24, no. 9, pp. 1419-35, Nov, 1998.

[111] N. C. Rouze, M. H. Wang, M. L. Palmeri, and K. R. Nightingale, “Robust estimation of time-of-flight shear wave speed using a radon sum transformation,” *IEEE Trans Ultrason Ferroelectr Freq Control,* vol. 57, no. 12, pp. 2662-70, Dec, 2010.

[112] S. J. Hsu, R. R. Bouchard, D. M. Dumont, P. D. Wolf, and G. E. Trahey, “In vivo assessment of myocardial stiffness with acoustic radiation force impulse imaging,” *Ultrasound Med Biol,* vol. 33, no. 11, pp. 1706-19, Nov, 2007.

[113] J. J. Dahl, D. M. Dumont, J. D. Allen, E. M. Miller, and G. E. Trahey, “Acoustic radiation force impulse imaging for noninvasive characterization of carotid artery atherosclerotic plaques: a feasibility study,” *Ultrasound Med Biol,* vol. 35, no. 5, pp. 707-16, May, 2009.

[114] R. H. Behler, T. C. Nichols, H. Zhu, E. P. Merricks, and C. M. Gallippi, “ARFI imaging for noninvasive material characterization of atherosclerosis. Part II: toward in vivo characterization,” *Ultrasound Med Biol,* vol. 35, no. 2, pp. 278-95, Feb, 2009.

[115] T. J. Czernuszewicz, J. W. Homeister, M. C. Caughey, M. A. Farber, J. J. Fulton, P. F. Ford, W. A. Marston, R. Vallabhaneni, T. C. Nichols, and C. M. Gallippi, "In vivo characterization of atherosclerotic plaque of human carotid arteries with histopathological correlation using ARFI ultrasound." pp. 1794-1797.

[116] A. C. Sharma, M. S. Soo, G. E. Trahey, and K. R. Nightingale, "Acoustic radiation force impulse imaging of in vivo breast masses." pp. 728-731 Vol.1.

[117] L. Zhai, J. Dahl, J. Madden, V. Mouraviev, T. Polascik, M. Palmeri, and K. Nightingale, "Three-dimensional acoustic radiation force impulse (ARFI) imaging of human prostates in vivo." pp. 540-543.

[118] J. J. Dahl, G. F. Pinton, M. L. Palmeri, V. Agrawal, K. R. Nightingale, and G. E. Trahey, "A parallel tracking method for acoustic radiation force impulse imaging," *IEEE Trans Ultrason Ferroelectr Freq Control,* vol. 54, no. 2, pp. 301-12, Feb, 2007.

[119] C. S. Hung, P. H. Tseng, C. H. Tu, C. C. Chen, W. C. Liao, Y. C. Lee, H. M. Chiu, H. J. Lin, Y. L. Ho, W. S. Yang, M. S. Wu, and M. F. Chen, "Nonalcoholic Fatty Liver Disease Is Associated With QT Prolongation in the General Population," *J Am Heart Assoc,* vol. 4, no. 7, Jul 21, 2015.

[120] W. Kratzer, V. Fritz, R. A. Mason, M. M. Haenle, and V. Kaechele, "Factors affecting liver size: a sonographic survey of 2080 subjects," *J Ultrasound Med,* vol. 22, no. 11, pp. 1155-61, Nov, 2003.

[121] P. Song, M. W. Urban, A. Manduca, H. Zhao, J. F. Greenleaf, and S. Chen, "Comb-push ultrasound shear elastography (CUSE) with various ultrasound push beams," *IEEE Trans Med Imaging,* vol. 32, no. 8, pp. 1435-47, Aug, 2013.

[122] P. Song, H. Zhao, A. Manduca, M. W. Urban, J. F. Greenleaf, and S. Chen, "Comb-push ultrasound shear elastography (CUSE): a novel method for two-dimensional shear elasticity imaging of soft tissues," *IEEE Trans Med Imaging,* vol. 31, no. 9, pp. 1821-32, Sep, 2012.